

AD-759 176

HEAT-TRANSFER AND FLOW-FIELD TESTS OF
THE MCDONNELL DOUGLAS-MARTIN MARIETTA
SPACE SHUTTLE CONFIGURATIONS

R. K. Matthews, et al

Arnold Engineering Development Center
Arnold Air Force Station, Tennessee

April 1973

DISTRIBUTED BY:

NTIS

National Technical Information Service
U. S. DEPARTMENT OF COMMERCE
5285 Port Royal Road, Springfield Va. 22151

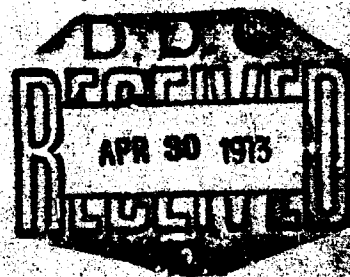


**HEAT-TRANSFER AND FLOW-FIELD TESTS
OF THE MCDONNELL DOUGLAS-MARTIN MARIETTA
SPACE SHUTTLE CONFIGURATIONS**

R. K. Matthews, R. H. Eaves, Jr., and W. R. Martindale

ARO, Inc.

April 1973



Approved for public release; distribution unlimited.

Reproduced by
**NATIONAL TECHNICAL
INFORMATION SERVICE**
U S Department of Commerce
Springfield VA 22151

**VON KARMAN GAS DYNAMICS FACILITY
ARNOLD ENGINEERING DEVELOPMENT CENTER
AIR FORCE SYSTEMS COMMAND
ARNOLD AIR FORCE STATION, TENNESSEE**

DOC	REF ID: A660000
STANDARD	
JUSTIFICATION	
BY	
DISTRIBUTION/AVAILABILITY CODE	
NO.	AVAIL. OR/NOT
A	

NOTICES

When U. S. Government drawings specifications, or other data are used for any purpose other than a definitely related Government procurement operation, the Government thereby incurs no responsibility nor any obligation whatsoever, and the fact that the Government may have formulated, furnished, or in any way supplied the said drawings, specifications, or other data, is not to be regarded by implication or otherwise, or in any manner licensing the holder or any other person or corporation, or conveying any rights or permission to manufacture, use, or sell any patented invention that may in any way be related thereto.

Qualified users may obtain copies of this report from the Defense Documentation Center.

References to named commercial products in this report are not to be considered in any sense as an endorsement of the product by the United States Air Force or the Government.

UNCLASSIFIED

Security Classification

DOCUMENT CONTROL DATA - R & D		
(Security classification of title, body of abstract and indexing annotation must be entered when the overall report is classified)		
1. ORIGINATING ACTIVITY (Corporate author) Arnold Engineering Development Center Arnold Air Force Station, Tennessee		2a. REPORT SECURITY CLASSIFICATION UNCLASSIFIED
		2b. GROUP N/A
3. REPORT TITLE HEAT-TRANSFER AND FLOW-FIELD TESTS OF THE MCDONNELL DOUGLAS--MARTIN MARIETTA SPACE SHUTTLE CONFIGURATIONS		
4. DESCRIPTIVE NOTES (Type of report and inclusive dates) Final Report - June 1971 to January 1972		
5. AUTHOR(S) (First name, middle initial, last name) R. K. Matthews, R. H. Eaves, Jr., and W. R. Martindale, ARO, Inc.		
6. REPORT DATE April 1973	7a. TOTAL NO. OF PAGES 106	7b. NO. OF REFS 47
8a. CONTRACT OR GRANT NO.	9a. ORIGINATOR'S REPORT NUMBER(S) AEDC-TR-73-53	
b. PROJECT NO. c. Program Element 921E-2 d.	9b. OTHER REPORT NO(S) (Any other numbers that may be assigned this report) ARO-VKF-TR-72-124	
10. DISTRIBUTION STATEMENT Approved for public release; distribution unlimited.		
11. SUPPLEMENTARY NOTES Available in DDC	12. SPONSORING MILITARY ACTIVITY Marshall Space Flight Center A&E-AERO-AAE Huntsville, Alabama 35812	
13. ABSTRACT Aerothermodynamic tests of Phase B space shuttle configurations proposed by McDonnell Douglas--Martin Marietta were conducted at Mach numbers 8 and 10.5. Test conditions provided both Mach number and Reynolds number simulation for typical ascent and reentry trajectories. This report provides a comprehensive analysis of the major test results and also presents data comparisons with theoretical calculations. Specific areas covered are ascent heating and shock interference, booster reentry heating and flow fields, and orbiter reentry analysis which includes leeside heating, windward shock angles and flow fields, windward surface heating, and boundary-layer transition.		

DD FORM 1 NOV 65 1473

UNCLASSIFIED
Security Classification

UNCLASSIFIED

Security Classification

14. KEY WORDS	LINK A		LINK B		LINK C	
	ROLE	WT	ROLE	WT	ROLE	WT
heat transfer flow field properties spacecraft reentry vehicles Reynolds number hypersonic flow hypervelocity flow						
APFC Amold APF Time						

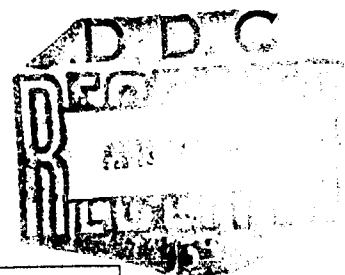
UNCLASSIFIED

Security Classification

1a

HEAT-TRANSFER AND FLOW-FIELD TESTS
OF THE MCDONNELL DOUGLAS-MARTIN MARIETTA
SPACE SHUTTLE CONFIGURATIONS

R. K. Matthews, R. H. Eaves, Jr., and W. R. Martindale
ARO, Inc.



Approved for public release; distribution unlimited.

ib

FOREWORD

The work reported herein was conducted at the Arnold Engineering Development Center (AEDC) under the sponsorship of the Marshall Space Flight Center (NASA-MSFC), Huntsville, Alabama, under Program Element 921E-2.

The results of tests presented were obtained by ARO, Inc. (a subsidiary of Sverdrup & Parcel and Associates, Inc.), contract operator of the AEDC, Air Force Systems Command (AFSC), Arnold Air Force Station, Tennessee. The tests were conducted in June and September 1971 and in January 1972 under ARO Project No. VT1162. The final data package was completed on May 10, 1972. The manuscript was submitted for publication on August 1, 1972.

The authors wish to express their appreciation to L. L. Trimmer who was the Facility coordinator for the space shuttle tests at AEDC and to S. R. Pate who wrote the boundary-layer transition results section. The assistance of H. R. Little, T. D. Buchanan, and A. H. Boudreau with the Tunnel F tests is also acknowledged. Dr. J. C. Adams, Jr., is responsible for the cross-flow theory presented herein, and G. E. Gilley deserves recognition for his efforts in developing the phase-change paint data reduction program. All of the above personnel are members of the Aerodynamics Division of the von Kármán Facility of ARO, Inc.

This technical report has been reviewed and is approved.

JIMMY W. MULLINS
Lt Colonel, USAF
Chief Air Force Test Director, VKF
Directorate of Test

A. L. COAPMAN
Colonel, USAF
Director of Test

CONTENTS

	<u>Page</u>
ABSTRACT	iii
NOMENCLATURE	vii
I. INTRODUCTION	1
II. APPARATUS	
2.1 Models	2
2.2 Wind Tunnels	3
III. PROCEDURES	
3.1 Test Conditions	4
3.2 Test Procedures and Data Reduction	6
IV. RESULTS AND DISCUSSION	
4.1 Ascent	13
4.2 Booster Reentry	14
4.3 Orbiter Reentry	16
V. CONCLUSIONS	22
REFERENCES	23

APPENDIXES

I. ILLUSTRATIONS

Figure

1. Typical Space Shuttle Trajectories and VKF Simulated Conditions	31
2. McDonnell Douglas Booster Model Sketch	32
3. Photograph of McDonnell Douglas Booster Model	33
4. McDonnell Douglas Delta Wing Orbiter Model Sketch	34
5. Photograph of McDonnell Douglas Orbiter Model (used in Tunnel B)	35
6. Photograph of the McDonnell Douglas Delta Wing Orbiter Installed in Tunnel F	36
7. Instrumentation Layout of Tunnel F Orbiter Model	37
8. Typical Timewise Variation of Tunnel F Conditions and Model Data	38
9. Probe-Rakes and Support (Tunnel B)	39
10. Photograph of Mated Configuration	40
11. Phase-Change Paint Photographs of Mated Configurations at $\alpha = 0$, $M_\infty = 8$, $Re_\infty = 3.7 \times 10^6 \text{ ft}^{-1}$	41
12. Phase-Change Paint Photographs of Mated Configurations at $\alpha = 0$, $M_\infty = 8$, $Re_\infty = 2.5 \times 10^6 \text{ ft}^{-1}$	42
13. Phase-Change Paint Photographs of Mated Configurations at $\alpha = +5 \text{ deg}$, $M_\infty = 8$, $Re_\infty = 2.5 \times 10^6 \text{ ft}^{-1}$	43
14. Phase-Change Paint Photographs of Mated Configurations at $\alpha = -5 \text{ deg}$, $M_\infty = 8$, $Re_\infty = 2.5 \times 10^6 \text{ ft}^{-1}$	44

<u>Figure</u>	<u>Page</u>
15. Mated Configuration Interference Heating at $\alpha = 0$, $M_\infty = 8$	45
16. Composite Shadowgraph of Mated Configuration at $\alpha = 0$, $Re_\infty = 2.5 \times 10^6 \text{ ft}^{-1}$, $M_\infty = 8$	46
17. Typical Booster Reentry Shadowgraph at $M_\infty = 8$	47
18. Booster Windward Centerline Pressure Distributions at $M_\infty = 8$, $Re_{\infty,L} = 7.3 \times 10^6$	48
19. Booster Windward Centerline Mach Number Profiles at $M_\infty = 8$ and $Re_{\infty,L} = 7.3 \times 10^6$	49
20. Typical Phase-Change Paint Photograph of Booster Bottom Surface at $M_\infty = 8$, $\alpha = 50 \text{ deg}$	50
21. Typical Side View Phase-Change Paint Photograph of Booster at $M_\infty = 8$, $\alpha = 50 \text{ deg}$	51
22. Booster Windward Centerline Heat Transfer Distributions, $M_\infty = 8$	52
23. Orbiter Lee Surface Phase-Change Paint Photographs, $M_\infty = 8$	53
24. Lee Surface Thermographic Phosphor Photographs, $M_\infty = 10.5$	54
25. Top Surface Heat Transfer Distributions, $\alpha = 50 \text{ deg}$, $M_\infty = 10.5$, $Re_{\infty,L} = 7.4 \times 10^6$	55
26. Orbiter Side Panel Phase-Change Paint Photographs, $M_\infty = 8$	56
27. Side Panel Thermographic Phosphor Photographs, $M_\infty = 10.5$	57
28. Side Panel Heat Transfer Distributions, $\alpha = 30 \text{ deg}$, $M_\infty = 10.3$, $Re_{\infty,L} = 4.9 \times 10^6$	58
29. Comparison of Windward and Lee-Side Centerline Heating Distributions	59
30. Flow Field Photographs of Orbiter	61
31. Comparison of Experimental and Theoretical Shock Angles	62
32. Orbiter Windward Centerline Pressure Distributions	63
33. Typical Orbiter Pitot Pressure and Total Temperature Profiles	64
34. Orbiter Windward Centerline Inviscid Mach Number Distributions	65
35. Comparison of Experimental and Theoretical Orbiter Windward Centerline Heating Distributions	66
36. Laminar and Turbulent Heat Transfer Results from Tunnel F, Phase II, $M_\infty = 10.8$, $\alpha = 40 \text{ deg}$	70
37. Laminar, Natural Transitional, and Turbulent Heat Transfer Results from Tunnel F, Phase II, $M_\infty = 10.8$, $\alpha = 40 \text{ deg}$	71
38. Effect of Unintentional Surface Roughness on Transition Results from Tunnel F at $M_\infty = 10.8$, $\alpha = 40 \text{ deg}$	72
39. Predicted Effect of Surface Roughness on Transition Results from Tunnel F at $M_\infty = 10.8$, $\alpha = 40 \text{ deg}$	73
40. Comparison of Transition Results with the Kipp-Masek Correlation	74
 II. TABLES	
I. Summary of Models	75
II. Nominal Test Conditions	76

II. TABLES (Continued)	
III. Tunnel Conditions Corresponding to Tunnel F Plotted Results	77
IV. Tunnel F Test Summary	78
III. EVALUATION OF STYCAST THERMAL PROPERTIES	79
IV. VKF BOUNDARY LAYER TRIP PROCEDURES USED DURING THE NASA-AEDC STS HEATING TEST IN TUNNEL B	89
V. PHASE-CHANGE PAINT DATA REDUCTION ASSUMPTIONS	91
VI. FLOW FIELD REGIMES ON THE WINDWARD SURFACE OF THE MCDONNELL DOUGLAS ORGITER	93
VII. LOCALLY SIMILAR BOUNDARY LAYER CALCULATIONS USING THE TABULATED SOLUTIONS OF DEWEY AND GROSS	95

NOMENCLATURE

c	Specific heat of Stycast, Btu/lbm-°R
H	Stagnation enthalpy, Btu/lbm
h	Heat transfer coefficient, $\dot{q}/(T_o - T_w)$, Btu/ft ² -sec-°R
k	Conductivity of Stycast Btu/ft-sec-°R or diameter of roughness element (sphere diam), in.
L	Axial length of model, in. (see Figs. 2 and 4)
M	Mach number
M*	Local Mach number at a distance y* from surface
p	Pressure, psia
p _c	Stagnation pressure downstream of a normal shock, psia
\dot{q}	Heat transfer rate, Btu/ft ² -sec
\dot{q}_o	Stagnation heat transfer rate of a 1-in.-diam . . . where, Btu/ft ² -sec
Re _∞	Unit Reynolds number, ft ⁻¹

$Re_{\infty,L}$	Free-stream Reynolds number based on length
Re_{∞,x_t}	Transition Reynolds number based on free-stream conditions and x_t
$Re_{c,\theta}$	Reynolds number based on edge conditions and momentum thickness at x_t location
r	Local model span; used as radius in axisymmetric calculations (see Fig. 35)
T	Temperature °F or °R as noted
t	Tunnel F test section time, msec
Δt	Time increment that model has been exposed to uniform flow, sec (Tunnel B)
u	Velocity, ft/sec
x	Axial distance from model nose, in.
x_k	Axial distance from model nose to center of roughness element, in.
x_t	Axial distance from model nose to beginning of transition, in.
x_{t0}	Axial distance from model nose to beginning of transition on smooth body, in.
y	Distance from model surface, in.
y^*	Distance from model surface where $T_R/T_0 \approx 1.0$ (see Fig. 33), in.
α	Angle of attack, deg
δ_s	Angle between local tangents to model surface and bow shock, deg
δ^*	Model boundary layer displacement thickness at x_k , in.
θ_s	Angle between free-stream velocity vector and tangent to local bow shock, deg
μ	Viscosity, lbm/ft-sec
ρ	Density, lbm/ft ³
σ	Angle between model axis and local tangent to model surface, deg

SUBSCRIPTS

aw	Adiabatic wall conditions
c	Edge conditions
i	Initial conditions
l	Local conditions
o	Stilling chamber conditions
pc	Phase change
R	Rake measurement
w	Wall conditions
∞	Free-stream conditions
ref	Heat transfer parameter based on Fay-Riddell theory and a 1-ft nose radius scaled down to the model scale (i.e., 0.011 ft or 0.009 ft)

SECTION I INTRODUCTION

During the Phase B design studies of the Space Transportation System (Space Shuttle), a fully reusable concept requiring a booster and an orbiter was investigated by NASA. In support of the Phase B program, extensive aerothermodynamic tests of several proposed configurations were conducted at the von Kármán Facility of the AEDC. The tests were sponsored by NASA-MSFC; however, the configurations were determined by the two Phase B contractor teams which were composed of:

1. McDonnell Douglas-Martin Marietta
2. North American Rockwell-General Dynamics Convair

This report presents results for the McDonnell Douglas-Martin Marietta configurations. A parallel report (Ref. 1) documents test results for the North American Rockwell-General Dynamics Convair configurations.

Additionally, tests of basic delta wing shapes were included in the test program; and these results will be documented in a separate report. All data generated during this test program were submitted to the NASA-sponsored "System for Automated Development of Static Aerothermodynamic Criteria" (SADSAC) and are documented in data reports (Refs. 2 through 17).

The test objectives for the McDonnell Douglas-Martin Marietta configurations are summarized as follows:

1. Provide aerodynamic heating data for the ascent (launch) configuration including booster-orbiter interference effects.
2. Provide aerodynamic heating data for both booster and orbiter entry conditions.
3. Obtain flow-field and boundary-layer transition data at reentry conditions.

To accomplish these objectives, two VKF test facilities were utilized. The continuous-flow hypersonic Tunnel B was used to provide ascent and reentry data, and the hypervelocity hotshot Tunnel F provided orbiter reentry data. Tunnel B was chosen because of its unique combination of high data quality, high productivity, and large model size capability. Tunnel F was used to provide flight-matched Mach number-Reynolds number conditions. The high Reynolds number capability of Tunnel F permitted investigation of fully turbulent heating rate distributions and boundary-layer transition location at flight conditions. The test conditions for both tunnels are compared with representative Space Shuttle trajectories in Fig. 1 (Appendix I).

In Tunnel B, heat-transfer rates were determined using the phase-change paint technique on 0.011-scale ascent and orbiter reentry models and on 0.009-scale booster

reentry models. The nominal test conditions were Mach number 8 and free-stream Reynolds numbers, based on model length, from 2 million to 9 million. To produce a maximum amount of fully turbulent flow on the reentry models, boundary-layer trips were used during some of the tests. Model surface pressures and flow-field pressure and temperature data were obtained for the reentry models.

The Tunnel F tests were made in two entries. From the first entry, heat-transfer-rate and model surface pressure measurements were obtained on a 0.011-scale orbiter during simulated reentry. Heat-transfer-rate distributions were determined by the thermographic phosphor paint technique, whereas the primary pressure and heat-transfer data were recorded with gages. The nominal test conditions were: Mach 10.5 and free-stream Reynolds numbers, based on model length, from 2 million to 24 million. Results from the first entry (Phase I) indicated that surface irregularities such as pressure orifices and heat gages may have unintentionally "tripped" the boundary layer at high angles of attack and high free-stream Reynolds numbers. Consequently, a second entry was made whereby "natural" transition results were obtained at 40-deg angle of attack and flight Reynolds numbers.

In addition to the experimental program, a parallel analytic research program was conducted by the VKI under Air Force sponsorship. One particularly valuable result of this effort was the development of a calculation technique for the laminar and turbulent windward surface heating of space shuttle configurations at large angles of attack. Results from this technique are compared with the experimental results from the present program in this report; a thorough description of the analytical procedures and additional data comparisons are presented in Ref. 18.

SECTION II APPARATUS

2.1 MODELS

2.1.1 Tunnel B Models

Two basic configurations of the space shuttle vehicles were tested: the -17A booster (MDAC-B) and the delta wing orbiter (MDAC-DWO). For the booster configuration, two model scales were selected: 1.1 percent and 0.9 percent. The 0.9-percent booster was used to provide high angle-of-attack reentry heating data, while the 1.1-percent booster was used for the tests of the booster mated with the orbiter. Model drawings were provided by the McDonnell Douglas Corporation, and the model fabrication was subcontracted to the Grumman Aerospace Corporation by AEDC. A list of the models fabricated is shown in Table I (Appendix I). The two 0.009-scale booster models (Configuration Nos. 41 and 42) were geometrically the same but Configuration 42 had ten windward centerline pressure orifices. A sketch showing the overall booster model dimensions is presented in Fig. 2, and a photograph of the 0.9-percent booster is shown in Fig. 3. References 4 and 5 provide additional configuration description details, as well as tabulated model surface coordinates.

The two orbiter models (Configuration Nos. 21 and 22) were also geometrically similar, but Configuration 22 had a 1.0-in.-long steel nose and 10 windward centerline pressure orifices. A sketch showing the overall model dimensions is presented in Fig. 4, and a photograph of Configuration 21 is shown in Fig. 5. Reference 7 provides additional configuration description details, as well as tabulated model surface coordinates. The mated configuration (booster-orbiter) used in the ascent tests is discussed later in Section IV.

The phase-change paint technique, which was used to provide heat-transfer-rate measurements in Tunnel B, requires a model material of relatively low thermal diffusivity to permit extraction of accurate heating data. Basically, the data are reduced by assuming that the model is a thermally semi-infinite slab. Several materials have been used in wind tunnel tests which satisfy the semi-infinite slab requirement (within reasonable limits of time and material thickness). Probably the most commonly used material at present is Stycast®, which is a filled, high-temperature epoxy. Stycast 2762® was selected as the model material for the present tests because of its proved performance.

One important requirement for phase-change paint data reduction is knowledge of the model material thermophysical properties. To provide this information for these models, two approaches were taken. First, a laboratory analysis of samples of the material was made; second, 6-in.-diam hemispheres were cast from the same batch of Stycast used to cast each model. Calibration runs were made during the tests with each hemisphere model. The results of these tests are discussed in Appendix III.

Chromel®-Alumel® thermocouples were cast into all the Stycast models approximately 1/8 in. from the surface to measure the initial model temperature.

2.1.2 Tunnel F Model

A photograph of the 1.1-percent scale model of the delta wing orbiter mounted on the support sting in Tunnel F is shown in Fig. 6. The model fabrication consisted of a stainless steel lower surface up to the model reference plane (see Figs. 6 and 7) with the fuselage upper body and vertical fin made of a Fiberglas® composition. A complete layout of the model showing all instrumentation locations is shown in Fig. 7. The model was constructed at AEDC from loft lines supplied by McDonnell Douglas (Drawing No. 255BJ00050, Rev. B). Only the windward centerline was instrumented for Phase II. Reference 8 provides additional configuration and instrumentation location details.

2.2 WIND TUNNELS

2.2.1 Tunnel B

Hypersonic Wind Tunnel (B) is a continuous, closed-circuit, variable density wind tunnel with an axisymmetric contoured nozzle and a 50-in.-diam test section. The tunnel can be operated at nominal Mach numbers of 6 and 8 at stagnation pressures from 20 to 300 and 50 to 900 psia, respectively, at stagnation temperatures up to 1350°R. The

model can be injected into the tunnel for a test run and then retracted for model cooling or model changes without interrupting the tunnel flow.

2.2.2 Tunnel F

The Hypervelocity Wind Tunnel (F) is an electric-arc-heated impulse wind tunnel of the hotshot type developed at AEDC. The test gas, nitrogen or air, is initially confined in an arc chamber by a diaphragm located near the throat of a convergent-divergent nozzle. The gas is heated and compressed by an electric arc discharge resulting in rupture of the diaphragm and subsequent expansion through a 4-deg half-angle conical nozzle ($M_{\infty} = 10$ to 22) or a $M_{\infty} = 8$ contoured nozzle. Testing is possible in the conical nozzle at either the 108-in.-diam test section for Mach numbers from 13 to 22 or at the 54-in.-diam station for Mach numbers from 10 to 17. Useful run times between 50 and 200 msec are obtained.

The present tests were conducted at the 54-in.-diam station ($M_{\infty} \approx 10.5$) using nitrogen as the test gas with a useful run time of approximately 100 msec utilizing the 4-ft³ arc chamber.

SECTION III PROCEDURES

3.1 TEST CONDITIONS

The nominal test conditions for each phase of the tests are shown in Table II. The specific test conditions and tabulated data are documented in a series of SADSAC reports (Refs. 2 through 8).

3.1.1 Tunnel B

The Tunnel B flow conditions are such that perfect gas, isentropic relationships can be used to compute test section properties from measured reservoir conditions.

3.1.2 Tunnel F

Since Tunnel F operates with a constant volume reservoir with an initial charge density, the reservoir conditions vary with time. As a result, all tunnel conditions and model data results vary with time during the useful data range. Nondimensional values such as p_0'/p_0 and model p/p_0' are relatively constant with time. Timewise variations in such parameters as Reynolds number permits acquisition of data at different Reynolds numbers for the same run. In many instances, laminar, transitional, and turbulent flow may be identified at the same gage location as a result of Reynolds number variation during one run. An illustration of the timewise behavior of various parameters for typical tunnel conditions encountered during this test is shown in Fig. 8.

To monitor the tunnel conditions, two 1.0-in.-diam hemisphere cylinders instrumented with slug calorimeters were installed in the test section at an appropriate distance from the model to eliminate shock interference. A pitot probe was located near each hemisphere cylinder to measure the normal shock stagnation pressure. The reservoir pressure and pitot pressures were measured with strain-gage-type transducers developed at the AEDC-VKF. Detailed information concerning the heat-transfer and pressure instrumentation can be found in Ref. 19.

The use of these measurements to compute flow conditions is as follows: instantaneous values of p_o and p'_o are measured directly and an instantaneous value of \dot{q}_o is inferred from the hemisphere cylinder shoulder heat rate measurements. Stagnation enthalpy (H_o) is calculated from these measurements using Fay-Riddell theory (Ref. 20). With values of p_o , p'_o , and H_o known, the remaining flow conditions (M_∞ , Re_∞ , etc.) are calculated as described in Refs. 21 and 22. For the short run times experienced in a hotshot tunnel, the model wall temperature ratio (T_w/T_o) varies between 0.15 and 0.30 which approximates the range experienced with reentry vehicles. The flow conditions corresponding to results presented herein are provided in Table III, and a Tunnel F test summary is presented in Table IV.

3.1.3 Test Condition Uncertainties

Uncertainty in the basic tunnel flow parameters p_o , T_o , p'_o , and \dot{q}_o was estimated from repeat calibrations of the instrumentation and from repeatability and uniformity of the test section flows during tunnel calibrations. The individual contributions of these uncertainties were propagated through the appropriate flow equations to obtain the remaining uncertainties.

Approximate uncertainties in tunnel flow conditions are:

<u>Parameter</u>	<u>Uncertainty, percent</u>	
	<u>Tunnel B</u>	<u>Tunnel F</u>
p_o	± 0.5	± 5
p'_o	± 0.3	± 4
T_o	± 1.0	± 4
\dot{q}_o or \dot{q}_{ref}	N/A	± 5
M_∞	± 0.3	± 1.5
p_∞	± 2.0	± 6
ρ_∞	± 1.1	± 8
u_∞	± 0.5	± 3
H_o	± 1.4	± 5
h_{ref}	± 1.0	± 2
Re_∞	± 2.0	± 10

3.2 TEST PROCEDURES AND DATA REDUCTION

3.2.1 Phase-Change Paint Test Technique (Tunnel B)

The phase-change paint technique of obtaining heat-transfer data uses an opaque coating which changes phase from a solid to a liquid (melts) at a specific temperature. Tempilaq®, a paint consisting of calibrated melting point materials suspended in an inert carrier, was used as the phase-change indicator. The specific melting temperatures of the Tempilaq paints used were 100, 113, 125, 150, 156, 175, 200, 225, 250, 300, 350, 400, and 500°F. Uncertainties in the phase-change temperatures are estimated by the manufacturer to be ± 1 percent.

The primary data were obtained by photographing the progression of the melt lines with 70-mm sequenced cameras. During the ascent phase of the test, one camera was mounted in the top window of the tunnel and two in the upstream side window. During the reentry phase, three sides of the model were photographed simultaneously with cameras mounted in the top and side windows and with the third camera in the model injection tank below the test section. The cameras used Kodak® TRI-X Pan black-and-white film, and the time from the start of model injection and of each shutter opening was recorded on magnetic tape. The cameras were operated at 2 frames per second.

Backup data were obtained with 16-mm motion-picture cameras. These cameras were operated at 24 frames per second, and Kodak Ekatachrome ER color film was used. The models were lighted with fluorescent light banks.

Prior to each run, the model was cleaned and cooled with alcohol and then spray-painted with Tempilaq. The model was installed on the model injection mechanism at the desired test attitude, and the model temperature was measured with a thermocouple probe or with the model-embedded thermocouples. During the course of the test, many of the embedded thermocouples became inoperative, and the probe temperature was generally used to determine the model initial temperature. The model was then injected into the airstream for approximately 20 sec, and during this time the model surface temperature rise produced isotherm melt lines.

Since the maximum Reynolds number in Tunnel B was not sufficient to produce fully turbulent flow during the reentry phase, boundary-layer trips were used to induce transition so that turbulent heating levels could be determined. The trip application method is discussed in Appendix I.

The data reduction procedures used were somewhat more involved than previously used for paint data since the melt lines were transformed into body coordinates and the corresponding heat-transfer coefficients. The fundamentals of this data reduction technique are described below.

During each run, the tunnel conditions and time of each picture were recorded on magnetic tape. The heat-transfer coefficient for each picture was calculated from the semi-infinite slab transient heat conduction equation.

$$\frac{T_{pc} - T_i}{T_{aw} - T_i} = 1 - e^{\beta^2} \operatorname{erfc} \beta$$

where

$$\beta = \frac{h\sqrt{\Delta t}}{\sqrt{\rho ck}} \text{ and } \sqrt{\rho ck} = 0.11 - 0.008 \sqrt{\Delta t}$$

The equation for the thermal properties ($\sqrt{\rho ck}$) of Stycast was obtained by evaluation of a considerable amount of hemisphere calibration data and supplemented by VKI laboratory measurements (see Appendix III).

Heat-transfer coefficients were calculated for assumed adiabatic wall temperatures of T_o , $0.9T_o$, and $0.85T_o$. The use of three values of T_{aw} provides an indication of the sensitivity of the heat-transfer coefficient (h) to the values of T_{aw} assumed. For the sake of consistency, all heat-transfer coefficients in this report are based on $T_{aw} = T_o$. A discussion of other assumptions associated with the phase-change paint technique is presented in Appendix V. All heat-transfer coefficients were nondimensionalized by the theoretical stagnation point heat-transfer coefficient (Ref. 20) on a 1-ft-radius sphere scaled down by the model scale (0.011 ft or 0.009 ft).

The transformation of the melt line coordinates, as viewed by the camera (picture plane), to model coordinates was accomplished as follows. The 70-mm film was projected onto an 8- by 10-in. glass plate, and the melt contours were recorded using an analog-to-digital tracer, and stored on magnetic tape. In regions of relatively constant heating, a distinct melt line was frequently difficult to define, and in some cases the melt line tracings were terminated because of poor definition. A considerable amount of engineering judgment was involved in the interpretation of the melt patterns; consequently this was performed, or closely supervised, by an experienced engineer. To obtain the melt line tracings in body coordinates the following additional steps were taken:

1. The model surface coordinates were measured at selected model stations with a modified Sheffield Cordax coordinate measuring machine (Model 200);
2. The camera location relative to the model was determined;
3. Using the principles of photogrammetry and the information obtained in steps 1 and 2, the model coordinates were transformed into the picture plane;

4. The body coordinates of a given melt line were then obtained by interpolation in the picture plane with the results being stored on magnetic tape.

The level of the heat-transfer coefficient associated with each melt line was obtained by the solution of the semi-infinite slab conduction equation as previously discussed. With the level and body coordinates of the heat-transfer coefficients stored on magnetic tape, any desired machine-generated plot within the limits of available data can be produced. Much of the phase-change paint data in this report are presented as data fairings obtained from machine-generated plots.

3.2.2 Pressure Data (Tunnel B)

Model centerline static pressures and flow-field surveys were obtained at the conditions shown in Table II. Static-pressure orifice locations are shown in Figs. 2 and 4, and details of the flow-field survey rakes are shown in Fig. 9. The static pressures were measured with 15-psid transducers referenced to a near vacuum, while the rake pressures required an atmospheric reference in some cases. From repeat calibrations, the estimated pressure measurement precision is ± 0.003 psi or ± 0.5 percent, whichever is greater.

The model flow-field data were obtained with a pitot-pressure rake and a single-shield total-temperature probe rake (Fig. 9). The rakes were mounted side-by-side so that pressure and temperature measurements could be made simultaneously. Most of the orbiter flow-field data were obtained with rake No. 1; however, it failed during the tests, and a new rake and support mechanism were fabricated for the booster survey data. The new rake (No. 2) was similar to the first with only small changes in probe spacing.

By assuming the flow-field static pressure equal to the wall static pressure (p_q), the local Mach number (M_q) was calculated from the Rayleigh pitot formula

$$\frac{p_R}{p_q} = \left(\frac{6M_q^2}{5} \right)^{7/2} \left(\frac{6}{7M_q^2 - 1} \right)^{5/2} \quad \text{for } M_q \geq 1$$

or from the compressible Bernoulli equation

$$p_R/p_q = (1 + 0.2 M_q^2)^{7/2} \quad \text{for } M_q < 1$$

In general, the assumption of constant flow-field static pressure becomes less valid as the distance from the model surface increases.

Estimated uncertainties of the primary measurements are given as follows:

<u>Parameter</u>	<u>Uncertainty</u>
p_{ℓ}	± 1.0 percent
p_R	± 0.015 psia (for $p_R \leq 15$ psia) ± 0.021 psia (for $p_R > 15$ psia)
T_R	± 2.0 percent

3.2.3 Gage Data (Tunnel F)

3.2.3.1 Phase I

Model heat-transfer rates were measured with slug calorimeters and coaxial surface thermocouples. The slug calorimeters have a thin-film platinum resistance thermometer to sense the temperature of an aluminum disk which is exposed to the heat flux to be measured. The calorimeters are designed to measure a given range of heat-transfer rates by appropriate selection of the aluminum disk thickness. The coaxial surface thermocouple is comprised of an electrically insulated Chromel wire enclosed in a constantan cylindrical jacket. A thin-film junction is made between the Chromel and constantan at the surface. In practical measurement applications, the surface thermocouple behaves as a homogeneous, one-dimensional, semi-infinite solid. The instrument provides an electromotive force (E.M.F.) directly proportional to surface temperature which may be related by theory to the incident heat flux. All heat-transfer gages were bench-calibrated prior to their installation into the model. The precision of these calibrations is estimated to be ± 3 percent. Posttest calibrations were made for the majority of gages with calibration repeatability being within ± 3 percent. A limited number of model pressure measurements were made by transducers developed at the AEDC-VKF. Strain-gage-type transducers were used on the windward surface; whereas the variable-reluctance-type transducers were used on the leeward surface.

3.2.3.2 Phase II

The same model that was used for Phase I was reinstrumented for Phase II. All previous instrumented locations were filled with metal plugs and contoured to the model except the windward centerline heat gage locations. The windward centerline pressure orifices were plugged along with the model stagnation point orifice. The heat gages were primarily of the coaxial surface thermocouple type.

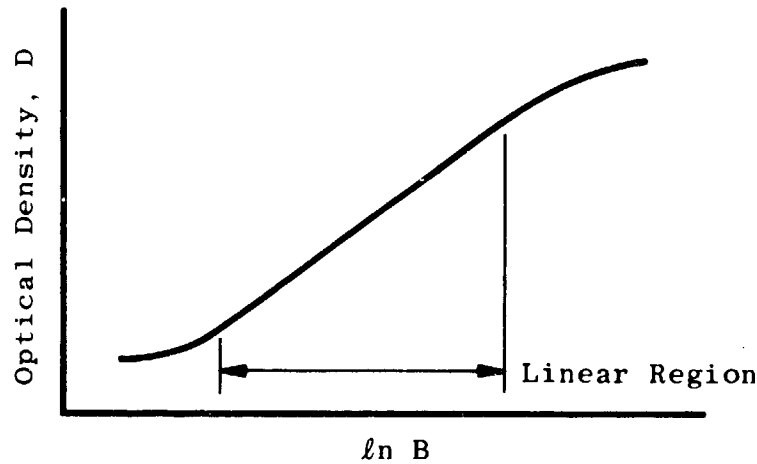
3.2.4 Phosphor Paint Technique (Tunnel F)

A relatively new thermal mapping test technique uses a phosphor material to coat the model surface. The phosphor when activated by ultraviolet light luminesces and this luminescence is temperature dependent. As temperature patterns develop during a test run, a photograph records the luminescence patterns. A densitometer analysis of the photograph provides a mapping of constant temperature contours. Heat-transfer rates are obtained from heat-rate gages located over the model surface so that the temperature

contours can be related to heating rates. The details of this technique are presented in the following subsections.

3.2.4.1 Theoretical Application

The phosphorescent paint technique consists of photographing the painted model surface and measuring the optical density of the recorded image. The optical density of a photographic image is a function of the logarithm of the intensity of the exposure, for a given exposure time (Ref. 23), as illustrated by the following figure.



Thus, if the exposure from the phosphorescent paint falls within the linear region (i.e., logarithmically linear), the optical density (D) is given by

$$D = A \ln B + C$$

From the paint characteristics,

$$\ln B = \ln f_1(I) + f_2(I, T_w)$$

therefore,

$$D = A \ln f_1(I) + A f_2(I, T_w) + C$$

where I is the u-v light intensity, B is the emitted light intensity (brightness) of the paint, and A and C are constants. For small changes in intensity (I), the functional relation f_2 is given by

$$f_2(I, T_w) \propto T_w$$

When using the phosphorescent technique in the wind tunnel, the procedure is to take a photograph of the model before the tunnel run (i.e., a tare) and then take another picture during the run. It is necessary that both pictures be taken in the "linear" region of the optical density curve. When the optical density of the tare photograph is subtracted from the optical density of the run photograph,

$$D - D_i \propto (T_w - T_{wi})$$

where the subscript i indicates the initial conditions; i.e., the tare photograph taken before the run.

It can be shown that the quantity $(T_w - T_{wi})$ is proportional to the heat-transfer rate to the model surface, for $T_w \ll T_{aw}$, and relatively short heating times ($\lesssim 1$ second) regardless of whether the "heat-transfer model" assumed for the technique is a semi-infinite slab (either a relatively thick layer of paint or a thin layer of paint mounted on a thick layer of material) or an infinite plate. This, of course, means that the optical density difference $(D - D_i)$ is then proportional to the model heat-transfer rate:

$$D - D_i = \Delta D \propto \dot{q}$$

The best way of evaluating the constant of proportionality is to measure a few heat-transfer rates with conventional heat-transfer instrumentation at the same time the paint data are taken. Heat-transfer rates as determined from gages give a calibration for the paint, so the paint data yield the detailed heat-transfer-rate distribution over the model.

3.2.4.2 Experiment

The ultraviolet light needed to excite the phosphorescence of the paint was generated by an Osram Xenon gas bulb XBO 1600w powered by an Ingersoll Product d-c supply. Three units were used for these tests. Each unit had a heat-absorbing glass and filter to eliminate all but the 3650 Å (black light) wavelength light.

Four view cameras with 4- by 5-in. Polaroid backs were used to record the pictures: two with 145-mm lens were located on the side of the tunnel, and two with 163-mm lens were on the bottom. Each camera had a set of filters to pass only the 5000 to 6000 Å light emitted by the paint. Type 57 Polaroid (ASA 3000) film was used to record the image.

The phosphor paint is a mixture of the phosphor material and a binder. The phosphor material is a fine grain powder ($\approx 10 \mu$ average size) of the ZCdS (zinc-cadmium-sulfate) with silver and nickel additives whose concentration control the temperature range of the phosphorescence. The binder can be any transparent or translucent liquid which can be sprayed. Normally, clear dope or epoxy is used.

The phosphor paint is applied as a thin coating to the model; therefore, the model wall material must be selected to give an observable temperature rise for the expected heat-transfer rate. The wall material selection, many times, is based on other things such as strength; hence, when the model material is not suitable to the paint technique, coatings are applied to produce the proper surface properties.

The following discussion documents the procedure using the microdensitometer to reduce the phosphor paint data. The optical density distributions on the tare and run pictures are read and recorded by a scanning microdensitometer P-1000 Photoscan[®] manufactured by Optronics International. The tare density is subtracted from the run density on the VKF-CDC 1604B digital computer, and the density differences are plotted on a CRT plotter (one density difference per plot). Each plot (i.e., density difference) is assigned a color and copied by hand in that color so that a color composite of all the plots is made. The boundaries of the colors are retraced, and the reference heat gages and model outline are located on this tracing.¹

The heat gage measurements and the optical density differences are plotted to obtain a relationship between the two. The relationship gives the heat-transfer values corresponding to the color regions. These values are noted on the color tracing, thereby resulting in a contour mapping of the heat-transfer rates on the model. Typical final contour mappings using the phosphor paint technique will be illustrated in a subsequent section.

The model image is distorted by the viewing angle of the camera. This distorted view is reflected in the final contour mapping. However, by using the heat-transfer-gage locations to scale the centerline and span results as was done herein, the final paint results can be obtained in a true normal projection. Automated procedures are now available whereby body coordinates may be obtained directly from the picture plane coordinates (see Section 3.2.1).

The uncertainty associated with the phosphor paint results is not a constant but varies from run to run. Some of the more important guidelines that determine the paint uncertainty are the range of optical density (affects the optical density resolution) and the uncertainty associated with relating the heat gage measurements with the paint distribution. These two uncertainties are interrelated and as a result the uncertainty generally quoted for the paint results is based on the agreement between heat-gage measurements and the paint distribution. Based on agreement between heat gages and paint distributions for all paint pictures reduced for this test, the following average uncertainties were computed for the maximum heat rate encountered on each run:

h/h_{ref} , Windward surface	± 12 percent
h/h_{ref} , Leeward surface	± 7 percent

¹Since the completion of these tests, a system has been installed at the VKF which automatically provides a density-color analysis of the black and white photographs.

SECTION IV RESULTS AND DISCUSSION

The space shuttle Phase B design studies were being completed during the time period of these tests, and shortly thereafter the fully reusable, flyback, two-stage system was abandoned by NASA. At present, a water recovery of an unmanned booster is planned, and the orbiter, while retaining its basic delta wing shape, is about two-thirds the size of the Phase B orbiter. The use of external fuel tanks for the orbiter ascent engines has made this size reduction possible without serious compromise of the payload capabilities.

In light of these developments, much of the data obtained from these tests may not be directly applicable. However, a wealth of knowledge was accumulated which can be applied to future programs. With these facts in mind, the major objective of this report is to review the basic results and the techniques employed during the course of the test program. Most of the orbiter results presented herein were previously presented in Ref. 24.

4.1 ASCENT

The ascent configuration tested is shown in Fig. 10. Heat-transfer measurements were obtained by the phase-change paint technique on 0.011-scale Stycast models. The orbiter nose was 1.86 in. downstream of the booster nose, and the gap between the models was between 0 and 0.02 in. No attempt was made to seal the mating line between the models, and the models were held together by the support bracket shown in the photograph (Fig. 10). The orbiter model used for this phase of the test was the same model used during the orbiter reentry phase.

The nominal test conditions were: Mach 8; free-stream unit Reynolds numbers of 0.8×10^6 , 2.5×10^6 , and 3.7×10^6 ft⁻¹ and angles of attack of -5, 0, and +5 deg. Additional information and a complete set of the data are presented in Refs. 2 and 3.

Because of the complexity of the configurations, the phase-change paint data are presented as data photographs. Typical phase-change paint photographs are presented in Figs. 11 through 14; and, of course, the heat-transfer ratios shown apply only to the melt lines in the corresponding photographs. The hotter regions are vividly depicted as the white paint melts and the black model shows through. Each figure presents four sequential photographs and, therefore, four levels of heat-transfer ratios (h/h_{ref}). In most cases, at least two different paint temperatures were required to span the range of h/h_{ref} shown.

As expected, the leading edges and noses were regions of relatively high heating ($h/h_{ref} = 0.271$, Fig. 11). However, shock interference produced relative "hot spots" in several other areas on both the orbiter and booster. In the second photograph of Fig. 11 ($h/h_{ref} = 0.126$), "hot spots" are observed in the region between the models, above the canard, and on the side of the booster. The remaining two photographs illustrate the extent of

these "hot spots" and provide some insight into the complexity of the flow field. The series of photographs presented in Fig. 12 was obtained at a Reynolds number of $2.5 \times 10^6 \text{ ft}^{-1}$, while those of Fig. 11 correspond to a Reynolds number of $3.7 \times 10^6 \text{ ft}^{-1}$. Comparisons of the extent of the melt on the second pictures of Figs. 11 and 12 ($h/h_{\text{ref}} \approx 0.125$) does not indicate any detectable Reynolds number effect since the melt patterns are very similar².

Figures 13 and 14 show the melt patterns for angles of attack of +5 and -5, respectively. In the bottom picture of Fig. 13 ($h/h_{\text{ref}} = 0.027$), the streaks caused by melted paint provide an indication of the local flow direction. Figure 14 clearly shows the orbiter bow shock interference heating on the booster top centerline. A plot of the booster top centerline heating distribution (Fig. 15a) at $\alpha = 0$ shows that two peaks exist with the first peak at $x \approx 7$ in. being about sixty times higher than the booster-alone data fairing. The maximum value of h/h_{ref} for the second peak at $x \approx 9$ in. was not measured; however, the indications are that the interference heating was more than 100 times higher than the booster-alone level. A typical posttest photograph is also presented in Fig. 15b, and a complete set of these pictures may be found in Ref. 2. The primary value of the posttest photographs is that regions which were hidden from camera view during the run are revealed by separating the two models, as shown.

A composite shadowgraph picture (Fig. 16) shows the interaction between the bow shock of the orbiter and booster which is the cause of the high heating in this region. Edney (Ref. 25) classified shock interference patterns and the associated heating amplifications into six types. The bow shock interactions of the present configuration can probably be classified as Type I. For the general cases studied by Edney, a Type I interaction has associated with it a factor of 10 increase in local heating; however, for the specific conditions of the present tests, the local heating was increased by a factor of at least 100 (see Fig. 15a). This discrepancy points out the danger in trying to apply generalized results to a specific case.

4.2 BOOSTER REENTRY

A 0.009-scale model of the booster was tested at simulated reentry conditions at Mach 8 in Tunnel B. Phase-change paint heat-transfer data were obtained at $\alpha = 40, 50$, and 60 deg at length Reynolds numbers of 5.0×10^6 and 7.3×10^6 . Windward centerline surface pressure and flow-field data were obtained at $\alpha = 40$ and 50 deg at a length Reynolds number of 7.3×10^6 . Figures 17 through 22 summarize the results of these tests, and a complete set of the data may be found in Refs. 4 and 5.

Theoretical analysis of the booster flow field is complicated by the interaction of the bow shock and canard shock which is shown in Fig. 17. However, comparison of modified Newtonian surface pressure distributions with the experimental measurements

²In the second picture of Fig. 12 ($h/h_{\text{ref}} = 0.125$), the series of short black dashes downstream of the canard should be ignored since they are not valid melt lines.

(Fig. 18) does exhibit reasonable agreement. Windward centerline Mach number profiles obtained by the procedures outlined in Section 3.2.2 are presented in Fig. 19. At $\alpha = 50$ deg, the profiles are smoother than those at $\alpha = 40$ deg, which may be attributed to the canard shock influencing the windward centerline flow field more at the lower angles of attack. Boundary-layer-edge Mach numbers were not determined from these data because of the relatively large total temperature probe spacing compared with the boundary-layer thickness.

A typical phase-change paint photograph of the booster windward surface is presented in Fig. 20. Regions of relatively high heating are clearly indicated on the canard and wing and the maximum measured level in these regions was about $(h/h_{ref}) \approx 0.5$. The cause of these relative "hot spots" can probably be attributed to bow shock impingement. A side view of the model (Fig. 21) shows "hot spots" just upstream and downstream of the canard and below the wing root. The maximum measured heating levels in these regions approached the level measured on the model nose region ($h/h_{ref} \approx 0.35 - 0.40$).

The effect of Reynolds number on windward centerline heat-transfer-rate distributions is presented in Fig. 22a. To ensure that turbulent heating levels were obtained, boundary-layer trips were used for several runs. A discussion of the tripping procedure may be found in Appendix IV. The level of peak heating caused by the canard ($x/L \approx 0.4$) was about $h/h_{ref} \approx 0.4$ at $\alpha = 40$ and 50 deg with a slight decrease at $\alpha = 60$ deg, all three data fairings are similar which implies turbulent flow existed for each case; however, at $\alpha = 60$ deg, the tripped data fairing is significantly higher than the others.

The theoretical distributions shown in Fig. 22b were obtained from numerical solutions of the governing three-dimensional laminar and turbulent boundary-layer equations for the stagnation line of a swept cylinder following Kaups and Keltner (Ref. 26) and Hunt, Bushnell, and Beckwith (Ref. 27). The turbulent eddy viscosity model used was that of Adams (Ref. 28). The local pressure levels and edge conditions were calculated, assuming that the shock was parallel to the model surface. On the cylindrical portion of the model, the crossflow velocity gradient was obtained from a Newtonian pressure distribution. On the remaining portions of the model (see Fig. 22b), the velocity gradient was calculated from the pressure distribution on the rounded-shoulder flat-face body. This pressure distribution was obtained by the one-strip method of integral relations from South (Ref. 29). Additional data comparisons and a more complete description of the theoretical method may be found in Ref. 18.

There is good agreement between the data fairing and the laminar theory ahead of the canard, while downstream of the canard the data agree with the turbulent theory. The implication is that the canard-bow shock interaction tripped the boundary layer and, therefore, produced turbulent heating levels downstream of the canard. Also illustrated in this figure is the obvious failure of crossflow theory to predict the spike in the heat-transfer distribution in the region of the canard.

4.3 ORBITER REENTRY

The orbiter tests were conducted on 0.011-scale models in the continuous hypersonic Tunnel B at Mach 8 and in the hypervelocity hotshot Tunnel F at Mach 10.5. Unless otherwise noted, all results reported herein at Mach 10.5, Tunnel F, refer to the Phase I entry. Photographic data are used to illustrate the regions of peak heating on the leeside. Windward centerline data include measurements of shock angle, surface pressure, flowfield pitot pressure and total temperature, and heat-transfer coefficient distributions. Shock angles, surface pressures, and local Mach number distributions are compared with tangent cone theory over an angle-of-attack range from 10 to 60 deg. The measured heat-transfer coefficient distributions are compared with both laminar and turbulent theories; and in the last section, boundary-layer transition is discussed.

4.3.1 Leeside Heating

Typical phase-change paint photographs of the model leeside at $\alpha = 20, 40,$ and 60 deg at $M_\infty = 8$ are shown in Fig. 23. Isotherm lines are indicated by the black model surface (Stycast) showing through the white paint (Tempilaq). Typical photographs illustrating the thermographic phosphor paint technique used in Tunnel F for obtaining heat-transfer data are shown in Fig. 24. Leeside wind-on photographs at $\alpha = 20, 40,$ and 50 deg are presented as well as an $\alpha = 20$ deg tare (wind-off) picture which shows the general lighting and emission of the paint with no temperature gradients. Note, for example, that the intensity of the left wing tip in the tare picture (Fig. 24a) is similar to that of the wind-on picture (Fig. 24b).

At both Mach numbers, the canopy is clearly a "hot region" (Figs. 23 and 24). The level of the heating on the canopy will be shown in a later figure. A second "hot region" can be seen on the centerline meridian between the nose and the canopy. For an orbiter at $\alpha = 20$ and 40 deg, Hefner and Whitehead (Ref. 30) also observed peak heating in this region and attributed it to vortices emanating from the model nose area. It was shown in Ref. 30 that the peak heating in this region increased as Reynolds number increased, but this trend could not be confirmed by the present data. However, it should be pointed out that the present patterns are significantly elongated compared with those in Ref. 30, and this supports the conclusion of Whitehead and Bertram (Ref. 31) that nose shaping is a dominant factor in the leeside meridian heating. At $\alpha \geq 40$ deg, dark streaks on either side of the central streak imply that secondary vortices are present. Also of some interest is the wavy shape of the dark regions particularly at $\alpha = 50$ deg (Fig. 24d) and 60 deg (Fig. 23c).

Quantitative heat-transfer-rate distributions on the lee surface obtained by the phosphor paint technique at $M_\infty = 10.5$ are shown in Fig. 25. These results were obtained using the microdensitometer technique and are the result of considerable computer time and manual effort. Since the peak heating on the top surface is essentially confined to the top meridian, a limited number of heat gages normally is adequate to establish the maximum heat rate. However, the vortex streaks evident off the top meridian indicate the value of the paint techniques in locating hot regions.

Side view photographs at $M_\infty = 8$ and 10.5 are presented in Figs. 26 and 27, respectively. At $\alpha = 20$ deg, a single elongated "hot region" is evident on the body above the wing. As the angle of attack was increased from 20 to 40 deg, the "hot region" (i.e., darker areas) moved toward the nose and appears to cover a somewhat larger surface area. At $\alpha = 40$ deg, there is a series of elongated streaks on the body below the canopy. This implies that a series of vortices exist in this region. No significant Reynolds number effects were discernible for the leeside results.

The value of the paint techniques is further illustrated in Fig. 28 for the side panel of the orbiter at $M_\infty = 10.3$. The location of the side panel hot regions is a function of angle of attack thus making it relatively impossible to instrument the side panel with a reasonable number of heat-transfer gages to define the hot regions. The results shown in Fig. 28 illustrate hot regions from the paint distributions approximately four times the value of gage measurements in that general area.

Mach 8 leeside meridian data fairings are compared with windward centerline data fairings for $\alpha = 20, 40$, and 60 deg in Fig. 29a. As previously pointed out, the canopy heating is quite severe despite the fact that it is in the shadow of the bottom surface at $\alpha = 40$ and 60 deg. Normally, one would expect all heating levels on the leeside to be less than those on the windward centerline. As can be seen at $\alpha = 20$ deg, the peak heating on the canopy ($h/h_{ref} \approx 0.1$) exceeded that on the windward centerline for a Reynolds number of 4.5×10^6 . The peak heating in the region upstream from the canopy where vortical flow was observed was $h/h_{ref} \approx 0.03$. However, as the angle of attack increased there was a slight decrease in the leeside heating levels. The $M_\infty = 8$ locations of the side panel "hot regions" were shown in Fig. 26, and the peak heating levels are included in the lower right side of the graphs in Fig. 29a. The side panel peak heating was $h/h_{ref} = 0.04$, and this value occurred at $\alpha = 20$ deg.

Mach 10.5 leeside meridian data fairings are compared with windward centerline data fairings for $\alpha = 20, 40$, and 50 deg in Fig. 29b. These thermographic phosphor data fairings also show relatively high heating on the canopy and nose region as did the phase-change paint data fairings which were presented in Fig. 29a. However, the magnitude of the canopy peak heating level was not obtained.

The photographic data presented in this section have shown various "hot spots"; however, it should be pointed out that inspection of the photographs also shows that the majority of the leeside surface area experienced heating levels of h/h_{ref} less than 0.008.

4.3.2 Windward Shock Angles and Flow Fields

Typical shadowgraph and schlieren photographs at $M_\infty = 8$ and 10.5 are shown in Fig. 30, and shock angle measurements from such pictures are presented in Fig. 31. The data are presented in terms of the angle between the local body slope and the local bow shock. This angle is about 5 deg for all angles of attack. For $\alpha \leq 40$ deg, the data agree within ± 2 deg with the tangent cone theory. For angles around shock detachment (i.e.,

$\alpha = 50$ and 60 deg), the data are compared with the $\alpha = 30$ deg fairing, and as can be seen, the incremental shock angle is relatively insensitive to model angle of attack. No significant Mach number effects were observed.

In Fig. 32, windward centerline pressure distributions at $M_\infty = 8$ and 10.5 are compared with tangent cone and modified Newtonian theories. Modified Newtonian theory shows satisfactory agreement with the data for both Mach numbers and for all angles of attack (i.e., $10 \leq \alpha \leq 60$). However, at the intermediate angles, tangent cone theory shows better agreement with the data at $M_\infty = 8$.

Mach 8 windward centerline flow-field data were obtained at four model stations ($x/L = 0.3, 0.5, 0.7$, and 0.92) and at $\alpha = 10$ through 60 deg. Typical flow-field rake measurements at $\alpha = 20$ deg and $x/L = 0.5$ are shown in Fig. 33, and a complete set of data showing the Mach number profiles is presented in Ref. 7. The rake consisted of a column of 15 pitot pressure probes and an adjacent column of 6 total-temperature probes (see Fig. 9). The pitot pressure distribution shown (Fig. 33) is representative of the case where the bow shock entropy layer has not been completely engulfed by the boundary layer. To determine an approximate lower bound of the inviscid flow, the total-temperature profiles were used to define a value of y^* (the minimum value of y where $T_R/T_0 \approx 1.0$).³ The measured pitot pressure at y^* and the local surface pressure at the corresponding station were used to calculate M^* , the local flow-field Mach number. These Mach numbers are presented in Fig. 34. The distributions are compared with tangent cone theory where applicable. The experimentally determined Mach numbers are equal to, or below, the theory with a maximum deviation of about 20 percent.

4.3.3 Windward Heating

Mach number 8 heat-transfer coefficient distributions obtained using phase-change paint at $\alpha = 10$ and 20 deg are presented in Fig. 35a. The 10-deg angle-of-attack data are compared with two-dimensional and axisymmetric laminar local similarity theory and two-dimensional Spalding-Chi turbulent theory (Ref. 32) using the Colburn Reynolds analogy factor (1.25). Local flow properties were calculated using fairings of the experimental pressure data and shock angles. The radius (r) used in the axisymmetric calculation is shown superimposed on the orbiter planform sketch. A more complete description of the theory used may be found in Appendixes VI and VII.

Since the laminar data are bracketed by the 2-D and the axisymmetric solutions, only a small amount of streamline divergence is indicated at 10-deg angle of attack. The turbulent data are in reasonable agreement (approximately 20 percent) with the Spalding-Chi theory. The boundary-layer trips consisted of 0.030-in.-diam steel spheres located 1.0 in. from the model nose with 3-diam spacing between centers.

³The actual boundary-layer thickness (δ) may be slightly less than y^* since continuous profiles would be required to define δ .

The 20-deg angle-of-attack data (Fig. 35a) are compared with axisymmetric laminar theory and turbulent Spalding-Chi theory corrected to axisymmetric values by the method of Ref. 33. These corrections were less than 10 percent at all points. The laminar data agree with the axisymmetric theory both in magnitude and distribution. The turbulent data are once again within 20 percent of the Spalding-Chi theory.

In Fig. 35b, Mach 10.7 heat-transfer-rate gage data at 10- and 20-deg angle of attack are compared with theoretical solutions calculated in the same manner as those of the preceding figure. The laminar data show good agreement with the theoretical laminar solutions. At the highest Reynolds number there was about 30 to 40 percent difference between data and turbulent theory near the model midsection. At the lowest Reynolds number, the data appear to be transitional. In Ref. 34, it was shown that surface roughness which was not large enough to move the end of transition significantly upstream could considerably increase the heating rates downstream of the roughness. The small surface roughness produced by the heat gages and surface pressure taps may have had a similar effect on the present data at the lowest Reynolds number. The effect of surface roughness will be discussed in more detail in the next section.

Mach 8 heat-transfer coefficient distributions obtained using the phase-change paint technique at $\alpha = 40$ and 60 deg are presented in Fig. 35c. The experimental data are compared with both laminar and turbulent theories. The theoretical distributions were calculated by the crossflow method described in Ref. 18. Inviscid conical flow was assumed for the 40-deg angle-of-attack calculations while a shock angle 5 deg greater than body angle was used at 60 deg. This assumption will be discussed later. The crossflow inviscid velocity gradient was obtained by approximating the local body lower surface with either a spherical segment or a rounded-shoulder flat-face cylinder using the one-strip method of integral relations from South (Ref. 29). Additional data comparison and a more complete description of the theoretical calculations used herein are presented in Ref. 18. Agreement between theory and experiment (Fig. 35c) is within 20 percent for the laminar and turbulent cases at both angles of attack. The boundary-layer trips used at these angles of attack consisted of small (0.025-in.) clusters of grit spaced approximately 1 in. apart on the entire windward surface (see Appendix IV).

Mach 10.5 heat-transfer-rate gage data (Fig. 35d) at 50- and 60-deg angles of attack are compared with theoretical solutions calculated in the same manner as those of the previous figure. Good agreement is noted between theory and experiment at 50-deg angle of attack for a large range of Reynolds numbers. Two different turbulent solutions are presented for the $\alpha = 60$ deg results. When experimental shock angles are not known, a priori, and a detached shock is predicted; one normally treats the shock angle as parallel to the local surface deflection. These results are shown in Fig. 35d as $(\theta_s = \alpha + \sigma)$. Taking an average value of the incremental angle between the body slope and the local bow shock (≈ 5 deg, see Fig. 31) and adding this value to the previously used shock angle improve agreement between theory and experiment. Since the Newtonian pressure used to make the theoretical calculations was in good agreement with experiment, the pressure values were not adjusted. These turbulent solutions are noted as $(\theta_s = \alpha + \sigma + 5)$. It should be noted that the 5-deg increment added to the shock angle lowered

the turbulent theory approximately 10 percent and essentially had no effect on the theoretical laminar results.

A more complete discussion of the effect of shock angle, wall temperature, and local conditions on theoretical solutions is given in Ref. 18. Other items discussed in Ref. 18 include spanwise pressure and heat-transfer distributions and Reynolds number scaling.

4.3.4 Transition Results

Based on the majority of the results from the Phase I entry in Tunnel F, it was concluded that surface roughness such as pressure orifices and heat gages unintentionally "tripped" the boundary layer at high angles of attack. The primary purpose of the Phase II entry in Tunnel F was to obtain natural transition results at a high angle of attack and large free-stream Reynolds numbers. This section deals with results from the Phase II entry with an analysis of transition results. With revised model surface preparation including the replacement of some gages with metal plugs, "natural" transition results were obtained for one tunnel run at 40-deg angle of attack. Phosphor paint was not used during this phase of testing.

A plot of the centerline heating rate distribution for $\alpha = 40$ deg is shown in Fig. 36 along with theoretical laminar and turbulent rates. Good agreement with the theoretical results is noted. Although the onset of the transition location is moving with changes in Reynolds number, it is not evident from a data plot of this type if these results are natural transition data. Based on transition analysis plots presented later in this section, it was concluded that all of the transition data in Fig. 36 (with the possible exception of the data at $Re_{\infty}, ft^{-1} = 2.13 \times 10^6$) were tripped by the roughness associated with the most forward three heat gages.

Boundary-layer transition locations obtained with the forward three heat gages replaced with metal plugs and contoured flush with the model surface are shown in Fig. 37 at 40-deg angle of attack. Good agreement is shown between the experimental results and the laminar and turbulent theory. These data are defined as "natural" transition results. The word "natural" is used to imply that surface roughness did not appreciably affect the data. However, the transition data were probably affected by free-stream aerodynamic noise disturbances as discussed in Ref. 35. Although transition moved aft in Fig. 37 as compared with the x_t locations shown in Fig. 36, the presentation of data in this manner is not sufficient to establish if "natural" transition occurred.

One of the easiest and most direct methods to determine if the boundary layer is tripped is to plot x_t vs Re_{∞} as was done in Refs. 36 and 37. A similar method is to plot Re_{∞, x_t} vs Re_{∞} as was done in Fig. 13 of Ref. 38. As clearly shown in Fig. 38, the deviation of the "tripped" data from the natural transition locations is quite dramatic. Even if there is some uncertainty about whether "natural" transition data were obtained during a test, the x_t data can be compared with an x_t trend determined from assumed variations, such as

$$Re_{\infty, x_t} \approx (Re_{\infty})^{0.2}$$

or

$$Re_{\infty, x_t} = \text{constant}$$

Both of these approximations for an x_t vs Re_{∞} trend are included in Fig. 38.

Posttest measurements of protuberances from heat gages were of the order 0.0005 to 0.001 in. These are relatively small surface irregularities and it might at first thought appear that the boundary-layer flow on lifting bodies at high angles of attack and high Mach numbers is fundamentally different than has been reported in previous studies at the AEDC-VKF; e.g., Ref. 39. However, this is not the case, as shown by the results presented in Fig. 39. The methods of Potter-Whitfield (Ref. 40) and van Driest-Blumer (Ref. 36) were used to estimate the surface roughness effects on x_t assuming a single row of spheres were located at $x = 0.9$ in., $x/\ell = 0.040$. The displacement thickness correlation method of van Driest was used.

The x_t vs Re_{∞} profiles for trip heights of 0.001 and 0.004 in. calculated using the Potter-Whitfield method are presented in Fig. 39 along with calculations of the "knee" or "effective" point location determined using the displacement thickness method of van Driest-Blumer for roughness heights (k) of 0.0015, 0.002, 0.003, and 0.004 in. The agreement between the two methods is considered good. These results show that very small amounts of roughness can be expected to trip the boundary layer on lifting bodies at high angles of attack even at hypersonic speeds. Furthermore, either of these two methods appear to be adequate for estimating the effects of surface roughness, even for geometries and flow conditions outside the range of the original correlating data. Of course, further work needs to be done before the validity of the two methods as applied to these geometries and flow conditions is completely established.

Transition Reynolds number data from both tunnels are presented in Fig. 40 in terms of the Kipp-Masek (Ref. 41) correlating parameters. Local flow properties are calculated using ideal gas properties for the wind-tunnel test conditions. Conical flow is used to determine the shock wave angle and flow properties. For surface angles for which a detached shock is predicted, the shock wave angle is assumed parallel to the local deflection angle with isentropic expansion from properties behind the shock to classical Newtonian local pressure. For comparison purposes at $\alpha = 60$ deg, calculations were made with the shock angle increased 5 deg, which agrees with experiment, but maintains the same local pressure, which also agrees with experiment. These results indicated approximately 1 to 2 percent change in the correlation parameter. There are several observations to note from Fig. 40:

1. The Kipp-Masek data correlation had a large scatter band,
2. The correlating parameters did not account very well for the Re_{∞} variation in the $M_{\infty} = 10.5$ data. The $M_{\infty} = 8$ data for two Reynolds number values indicated a similar trend, and

3. The Tunnels B and F "natural" transition data showed good agreement with the revised transition correlation curve of Kipp and Masek for $\alpha \leq 50$ deg. However, some of the artificially tripped data (Tunnel F) was within the scatter band of the data correlation which indicates the insensitivity of the correlating parameter. Agreement or disagreement of experimental data with the best fit correlating curve should not be the sole determining factor used to establish whether transition data are "good" or "bad."

SECTION V CONCLUSIONS

Extensive wind tunnel tests of the McDonnell Douglas-Martin Marietta space shuttle configurations have been conducted at the von Kármán Facility of the Arnold Engineering Development Center (AEDC). The tests were conducted in Tunnel B at Mach 8 and in Tunnel F at Mach 10.5. The major conclusions of these tests are:

Ascent Phase:

1. "Hot spots" ($h/h_{ref} \geq 0.125$) were observed between the models, above the canard, and on the side of the booster.
2. The booster top centerline heating distribution exhibited two distinct peaks; the first was about 60 times greater than the undisturbed (booster-alone) level, and the second was more than 100 times greater than the undisturbed level.

Booster Reentry:

3. In addition to the nose and leading edges, "hot spots" were observed around the canard, on the wing, and on the body below the wing root. The maximum measured value was about $h/h_{ref} = 0.5$.
4. The windward centerline heat-transfer distribution peaked in the region of the canard.
5. A shock disturbance from the canard probably tripped the boundary layer since laminar cross-flow theory agreed with the data upstream of the canard and turbulent theory agreed with the data downstream of the canard.

Orbiter Reentry:

Leeside

6. "Hot regions" were observed on the canopy and on the nose upstream of the canopy: $(h/h_{ref})_{max} \approx 0.1$ and 0.03, respectively.

7. The side panel exhibited "hot streaks" which moved forward as angle of attack increased: $(h/h_{ref})_{max} \approx 0.04$.

Windward

8. The angle between the local body slope and the bow shock was about 5 deg and varied only slightly (± 2 deg) with angle of attack.
9. The pressure distributions were bracketed by tangent cone and modified Newtonian theory.
10. At $\alpha = 10$ and 20 deg, 2-D and axisymmetric theory agreed with both the laminar and turbulent data at Mach 8 within 20 percent. At the higher Reynolds number at $M_{\infty} \approx 10.5$, there was at most 40 percent difference between the data and turbulent theory at the model midsection.
11. At $\alpha = 40$ to 60 deg, cross-flow theory and experimental data agreed within 20 percent.

REFERENCES

1. Martindale, W. R., Matthews, R. K., and Trimmer, L. L. "Heat Transfer and Flow Field Tests of the North American Rockwell/General Dynamics Convair Space Shuttle Configurations." AEDC-TR-72-169, January 1973.
2. Matthews, R. K., Martindale, W. R., and Warmbrod, J. D. "Heat Transfer Tests of the McDonnell Douglas Delta Wing Orbiter Mated with -17A Booster at Mach Number 8." NASA CR-120,067, May 1972.
3. Matthews, R. K., Martindale, W. R., and Warmbrod, J. D. "Heat Transfer Test of the McDonnell Douglas Delta Wing Orbiter and the -17A Booster (not Mated) at Mach Number 8." NASA CR-120,068, May 1972.
4. Matthews, R. K., Martindale, W. R., and Warmbrod, J. D. "Heat Transfer Rate Distributions on McDonnell Douglas Booster Determined by Phase Change Technique for Nominal Mach Number of 8." NASA CR-120,043, April 1972.
5. Matthews, R. K., Martindale, W. R., and Warmbrod, J. D. "Surface Pressure and Inviscid Flow Field Properties of McDonnell Douglas Booster Nominal Mach Number of 8." NASA CR-120,047, March 1972.
6. Martindale, W. R., Matthews, R. K., and Warmbrod, J. D. "Heat Transfer Rate Distributions on the McDonnell Douglas Delta Wing Orbiter at a Mach Number of 8." NASA CR-120,025, June 1972.

7. Warmbrod, J. D., Martindale, W. R., and Matthews, R. K. "Surface Pressure and Inviscid Flow Field Properties of the McDonnell Douglas Delta-Wing Orbiter for Nominal Mach Number of 8." NASA CR-120,037, January 1972.
8. Eaves, R. H., Buchanan, T. D., and Warmbrod, J. D. "Heat Transfer Investigation of the McDonnell Douglas Delta Wing Orbiter at a Nominal Mach Number of 10.5." NASA CR-120,024, May 1972.
9. Warmbrod, J. D., Martindale, W. R., and Matthews, R. K. "Heat Transfer Rate Measurements on Convair Booster (B-15B-2) and North American Rockwell Orbiter (161B) at Nominal Mach Number of 8." NASA CR-120,009, November 1971.
10. Warmbrod, J. D., Martindale, W. R., and Matthews, R. K. "Heat Transfer Rate Measurements on Convair Booster (B-15B-2) at Nominal Mach Number of 8." NASA CR-119,987, November 1971.
11. Warmbrod, J. D., Martindale, W. R., and Matthews, R. K. "Heat Transfer Rate Measurements on North American Rockwell Orbiter (161B) at Nominal Mach Number of 8." NASA CR-120,029, December 1971.
12. Matthews, R. K., Martindale, W. R., and Warmbrod, J. D. "Heat Transfer Rate Distribution on North American Rockwell Delta Wing Orbiter Determined by Phase Change Paint Technique at a Mach Number of 8." NASA CR-120,048, March 1972.
13. Matthews, R. K., Martindale, W. R., and Warmbrod, J. D. "Surface Pressure and Inviscid Flow Field Properties of the North American Rockwell Delta-Wing Orbiter for Nominal Mach Number of 8." NASA CR-120,046, March 1972.
14. Matthews, R. K., Martindale, W. R., and Warmbrod, J. D. "Ascent Heat Transfer Rate Distributions on Tests of the NR Delta Wing Orbiter and GD/C Booster at Mach Number 8 (Mated)." NASA CR-120,049, July 1972.
15. Matthews, R. K., Martindale, W. R., and Warmbrod, J. D. "Ascent Heat Transfer Rate Distributions on the NR Delta Wing Orbiter and the GD/C Booster at Mach Number 8 (not Mated)." NASA CR-120,071, July 1972.
16. Matthews, R. K., Martindale, W. R., Warmbrod, J. D., and Johnson, C. B. "Heat Transfer Investigation of Langley Research Center Transition Models at a Mach Number of 8." NASA CR-120,045, March 1972.
17. Eaves, R. H., Buchanan, T. D., Warmbrod, J. D., and Johnson, C. B. "Heat Transfer Investigation of Two Langley Research Center Delta Wing Configurations at a Mach Number of 10.5." NASA CR-120,036, March 1972.

18. Adams, J. C., Jr. and Martindale, W. R. "Hypersonic Lifting Body Windward Surface Flow-Field Analysis for High Angles of Incidence." AEDC-TR-73-2 (AD756499), February 1973.
19. Ledford, R. L., Smotherman, W. E., and Kidd, C. T. "Recent Developments in Heat-Transfer Rate, Pressure, and Force Measurements for Hotshot Tunnels." AEDC-TR-66-228 (AD645764), January 1967.
20. Fay, J. A. and Riddell, F. R. "Theory of Stagnation Point Heat Transfer in Dissociated Air." Journal of Aerospace Sciences, Vol. 25, No. 2, pp. 73-85, 121, February 1958.
21. Grabau, Martin, Smithson, H. K., Jr., and Little, Wanda J. "A Data Reduction Program for Hotshot Tunnels Based on the Fay-Riddell Heat-Transfer-Rate Using Nitrogen at Stagnation Temperatures from 1500 to 5000°K." AEDC-TDR-64-50 (AD601070), June 1964.
22. Griffith, B. J. and Lewis, C. H. "A Study of Laminar Heat Transfer to Spherically Blunted Cones at Hypersonic Conditions." AEDC-TDR-63-102 (AD408568), June 1963. Also AIAA Journal, Vol. 2, No. 3, pp. 438-444, March 1964.
23. Todd, H. N. and Zakier, R. D. Sensitometry, Rochester Institute of Technology, 1962.
24. Matthews, R. K., Buchanan, T. D., Martindale, W. R., and Warmbrod, J. D. "Experimental and Theoretical Aerodynamic Heating and Flow Field Analysis of a Space Shuttle Orbiter." NASA TM X-2507, Vol. II, p. 261, February 1972.
25. Edney, Barry E. "Shock Interference Heating and the Space Shuttle." NASA TMX-52876, Vol. I, July 1970.
26. Kaups, K. and Keltner, C. "Laminar Compressible Boundary Layer on a Yawed Infinite Wing." Douglas Aircraft Company Report No. LB32706, March 1967.
27. Hunt, J. L., Bushnell, D. M., and Beckwith, I. E. "The Compressible Turbulent Boundary Layer on a Blunt Swept Slab with and without Leading-Edge Blowing." NASA TN D-6203, March 1971.
28. Adams, John C., Jr. "Analysis of the Three-Dimensional Compressible Turbulent Boundary Layer on a Sharp Cone at Incidence in Supersonic and Hypersonic Flow." AEDC-TR-72-66 (AD743003), June 1972.
29. South, J. C., Jr. "Calculation of Axisymmetric Supersonic Flow Past Blunt Bodies with Sonic Corners, Including a Program Description and Listing." NASA TN D-4553, May 1968.

30. Hefner, Jerry H. and Whitehead, Allen H., Jr. "Lee-Side Heating Investigations, Part I--Experimental Lee-Side Heating Studies on a Delta-Wing Orbiter." NASA Space Shuttle Technology Conference, NASA TM X-2272, Vol. I, March 1971, pp. 267-287.
31. Whitehead, Allen H., Jr. and Bertram, Mitchel H. "Alleviation of Vortex-Induced Heating to the Lee-Side of Slender Wings in Hypersonic Flow." AIAA Journal, Vol. 9, No. 9, September 1971, pp. 1870-1872.
32. Neal, Luther, Jr. and Bertram, Mitchel H. "Turbulent-Skin-Friction and Heat-Transfer Charts Adapted from the Spalding and Chi Method." NASA TN D-3969, May 1967.
33. Vaglio-Laurin, R. "Heat Transfer on Blunt Nosed Bodies in General Three-Dimensional Hypersonic Flow." Heat Transfer and Fluid Mechanics Institute, University of California, Los Angeles, California, June 11-13, 1959.
34. Sterrett, J. R., Morrisette, E. L., Whitehead, A. H., Jr., and Hicks, R. M. "Transition Fixing for Hypersonic Flow." NASA TN-D-4129, October 1967.
35. Pate, S. R. and Schueler, C. J. "Radiated Aerodynamic Noise Effects on Boundary-Layer Transition in Supersonic and Hypersonic Wind Tunnels." AIAA Journal, Vol. 7, No. 3, March 1969, pp. 450-457.
36. Van Driest, E. R. and Blumer, C. B. "Boundary-Layer Transition at Supersonic Speeds: Roughness Effects with Heat Transfer." AIAA Journal, Vol. 6, No. 4, April 1968, pp. 603-607.
37. Pate, S. R. "Supersonic Boundary-Layer Transition: Effects of Roughness and Free-Stream Disturbances." AIAA Journal, Vol. 9, No. 5, May 1971, pp. 797-803.
38. Pate, S. R. and Adams, J. C. "Hypersonic Simulation for Lifting Body Transition Studies." Presented at Boundary Layer Transition Specialists' Workshop, Aerospace Corporation, San Bernardino, California, November 3-5, 1971.
39. Whitfield, J. D. and Iannuzzi, F. A. "Experiments on Roughness Effects on Cone Boundary-Layer Transition up to Mach 16." AIAA Journal, Vol. 7, No. 3, March 1969, pp. 465-470.
40. Potter, J. L. and Whitfield, J. D. "Effects of Slight Nose Bluntness and Roughness on Boundary Layer Transition in Supersonic Flow." Journal of Fluid Mechanics, Vol. 12, Part 4, 1962, pp. 501-535.

41. Kopp, H. W. and Masok, R. O. "Aerodynamic Heating Constraints on Space Shuttle Vehicle Design." ASME Paper 70-HI/SPI-45, June 1970.
42. Jones, Robert A. and Hunt, James L. "Use of Fusible Temperature Indicators for Obtaining Quantitative Aerodynamic Heat-Transfer Data." NASA-TR-R-230, February 1966.
43. Throckmorton, David A. "Heat Transfer Testing Procedures in Phase B Shuttle Studies with Emphasis on Phase-Change Data Improvement." NASA Tech. Memo, NASA TMX-2507, February 1972.
44. Thomas, Alfred C. and Perlbachs, Andrew. "Application of Ground Test Data to Reentry Vehicle Design." AFFDL-TR-66-229, January 1967.
45. Nagel, A. L., Fitzsimmons, H. D., and Doyle, L. B. "Analysis of Hypersonic Pressure and Heat Transfer Tests on Delta Wings with Laminar and Turbulent Boundary Layers." NASA CR-535, August 1966.
46. Marvin, Joseph G. and Sinclair, A. Richard. "Convective Heating in Regions of Large Favorable Pressure Gradient." AIAA Journal, Vol. 5, No. 11, November 1967, pp. 1940-1948.
47. Dewey, C. Forbes, Jr., and Gross, Joseph F. "Exact Similar Solutions of the Laminar Boundary-Layer Equations." Advances in Heat Transfer, Vol. 4, New York: Academic Press, Inc., 1967, pp. 317-446.

APPENDIXES

- I. ILLUSTRATIONS**
- II. TABLES**
- III. EVALUATION OF STYCAST THERMAL PROPERTIES**
- IV. VKF BOUNDARY LAYER TRIP PROCEDURES USED
DURING THE NASA-AEDC STS HEATING TEST IN
TUNNEL B**
- V. PHASE-CHANGE PAINT DATA REDUCTION ASSUMPTIONS**
- VI. FLOW FIELD REGIMES OF THE WINDWARD SURFACES
OF THE McDONNELL DOUGLAS ORBITER**
- VII. LOCALLY SIMILAR BOUNDARY LAYER CALCULATIONS
USING THE TABULATED SOLUTIONS OF DEWEY AND
GROSS**

Sym	Test Phase
○	Ascent
□	Booster Reentry
△	Orbiter Reentry ($10 \leq \alpha \leq 60$ deg)

Flagged Symbols: Boundary Layer Trips Used

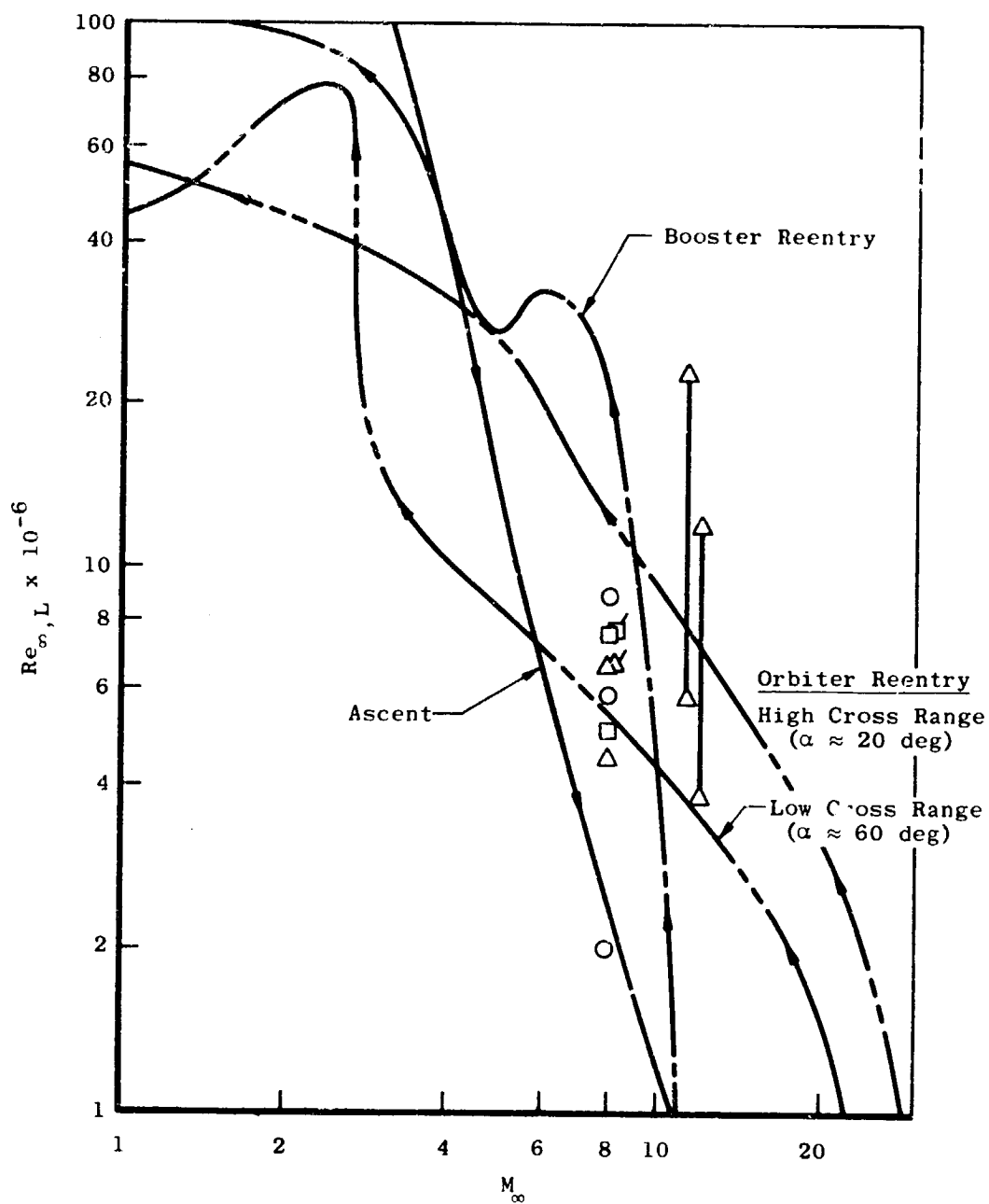


Fig. 1 Typical Space Shuttle Trajectories and VKF Simulated Conditions

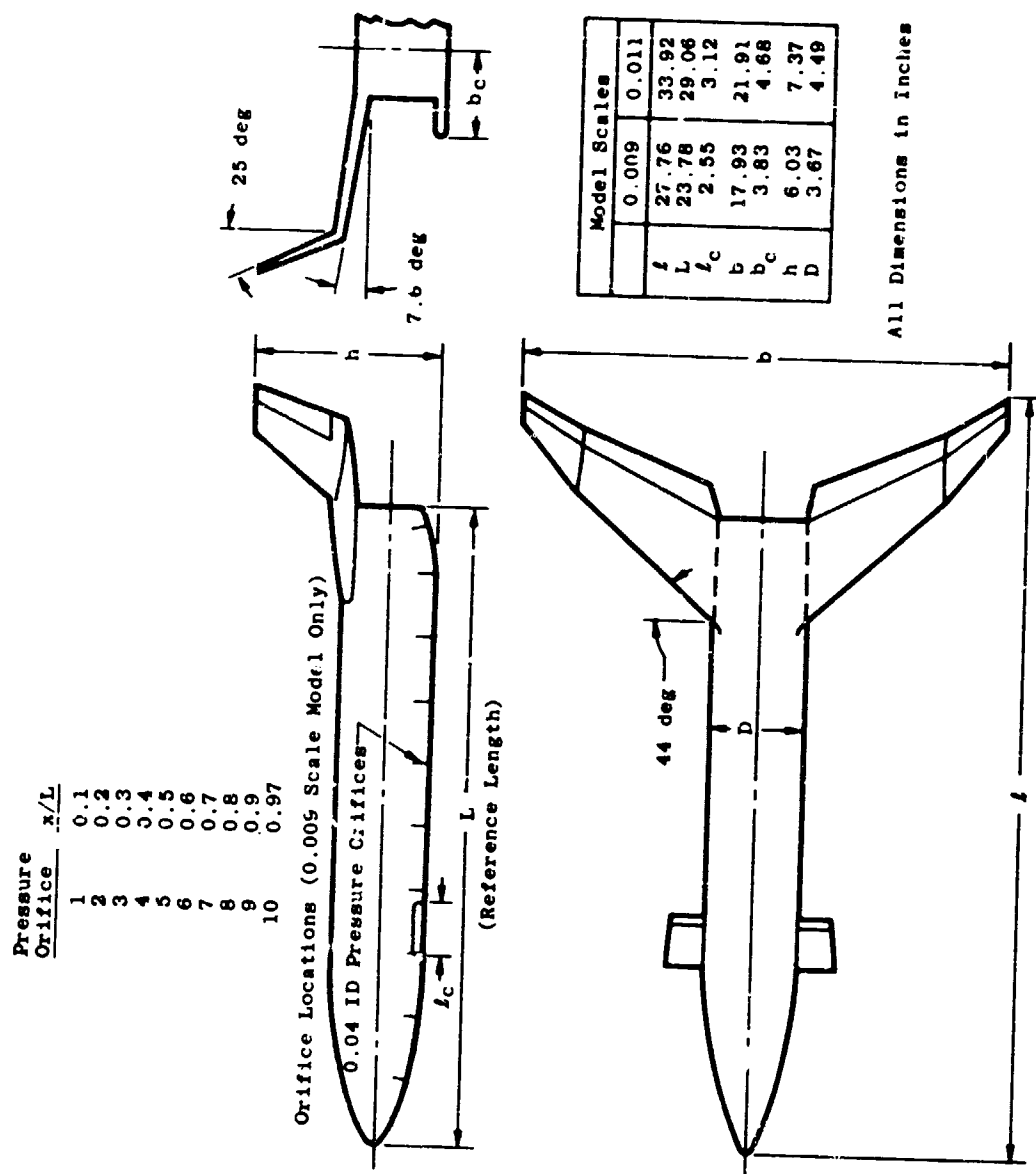
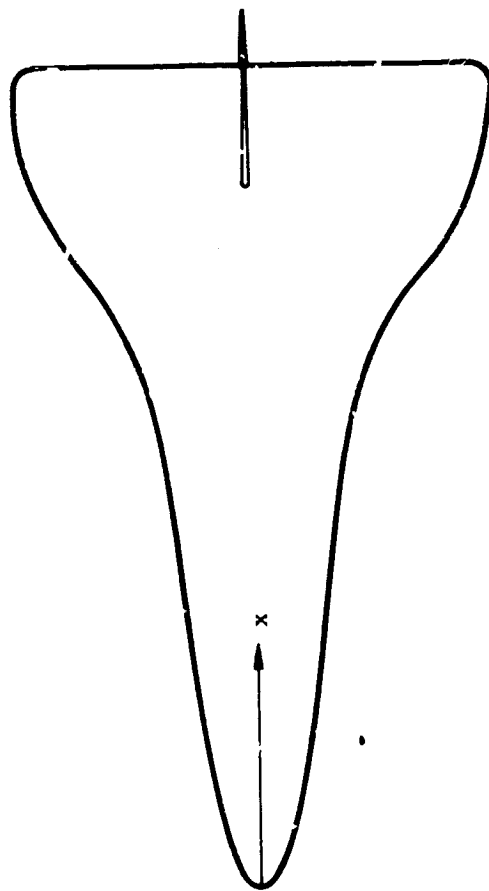


Fig. 2 McDonnell Douglas Booster Model Sketch



A E D C
71-813

Fig. 3 Photograph of McDonnell Douglas Booster Model



Tunnel B Model Only

Pressure Orifice	x/L
1	0.1
2	0.2
3	0.3
4	0.4
5	0.5
6	0.6
7	0.7
8	0.8
9	0.916
10	0.970

All Dimensions in Inches

Model Scale - 0.011

34

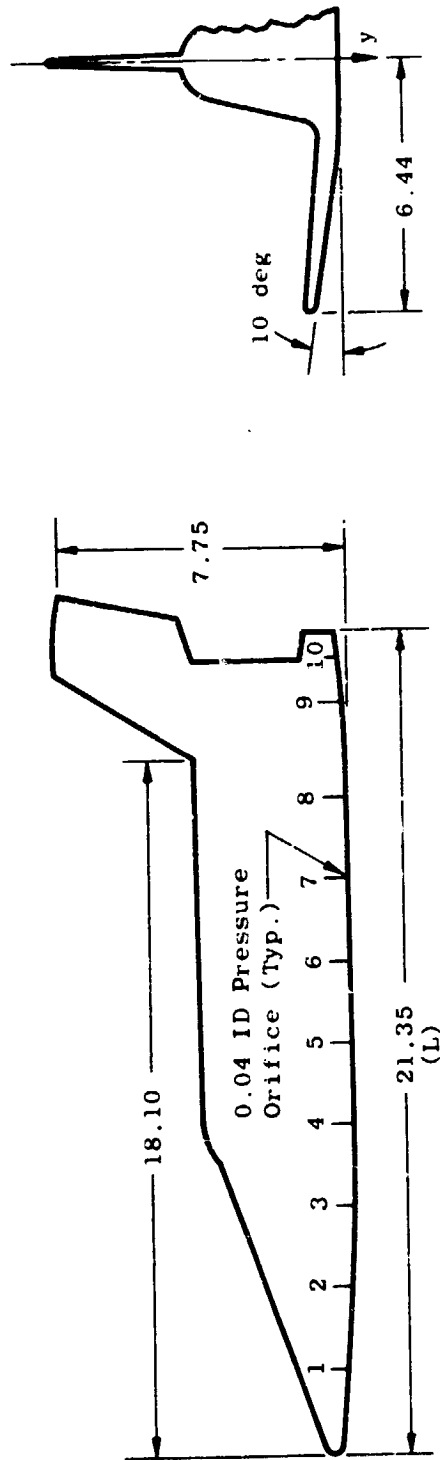


Fig. 4 McDonnell Douglas Delta Wing Orbiter Model Sketch

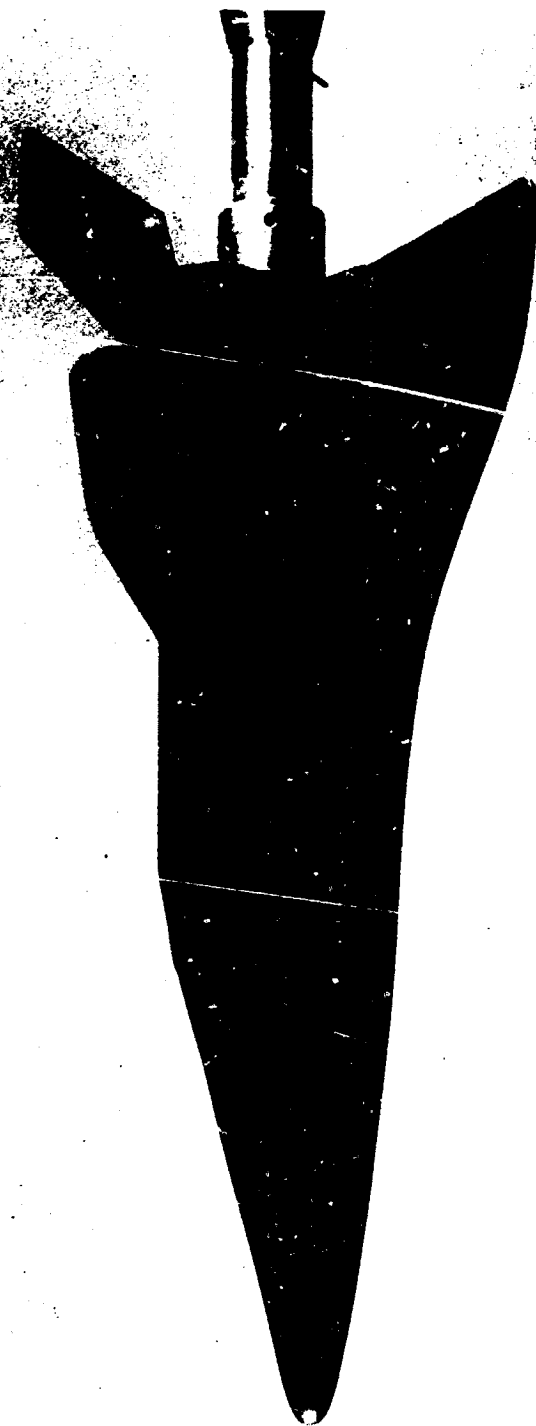


Fig. 5 Photograph of McDonnell Douglas Orbiter Model (used in Tunnel B)

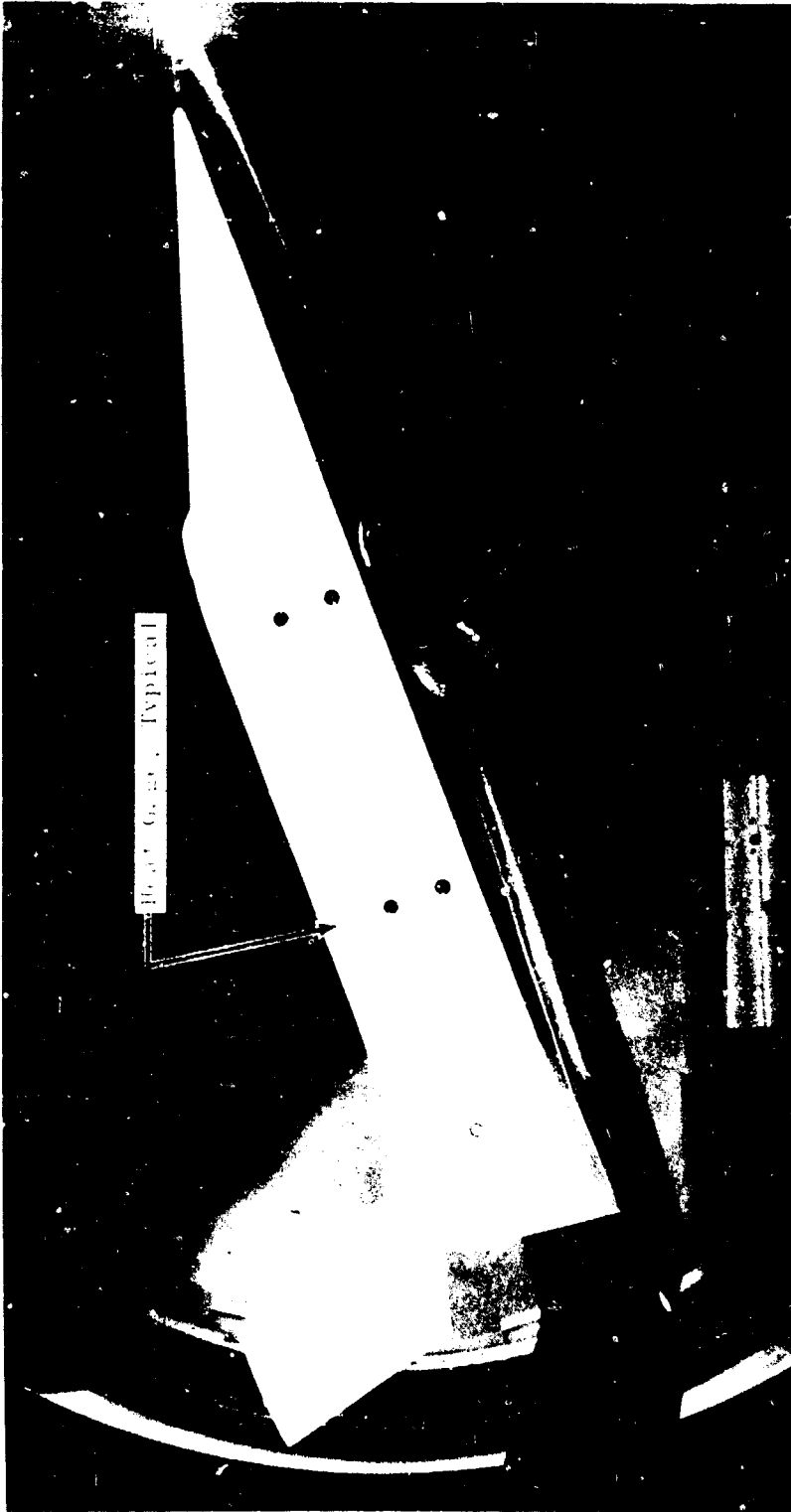


Fig. 6 Photograph of the McDonnell Douglas Delta Wing Orbiter Installed in Tunnel F

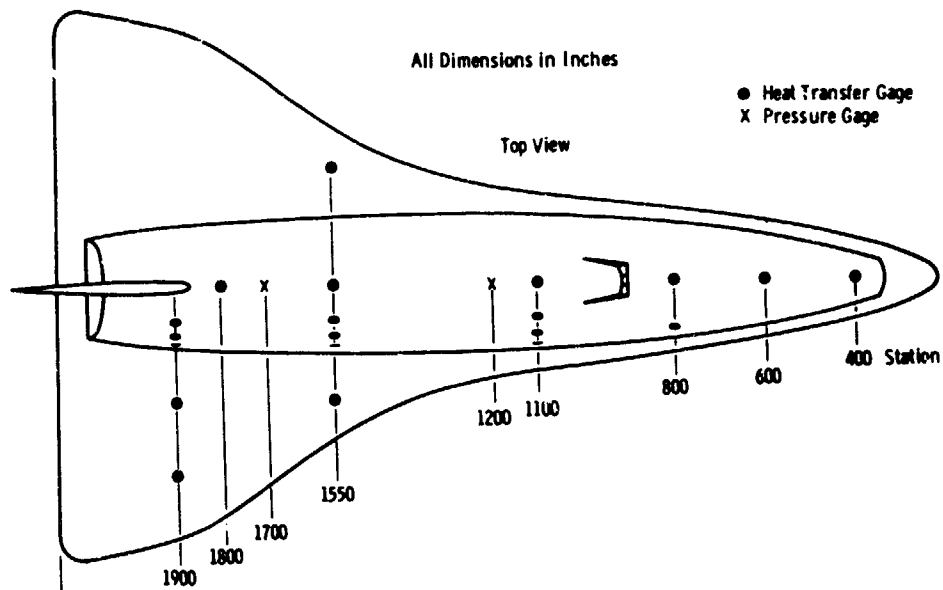
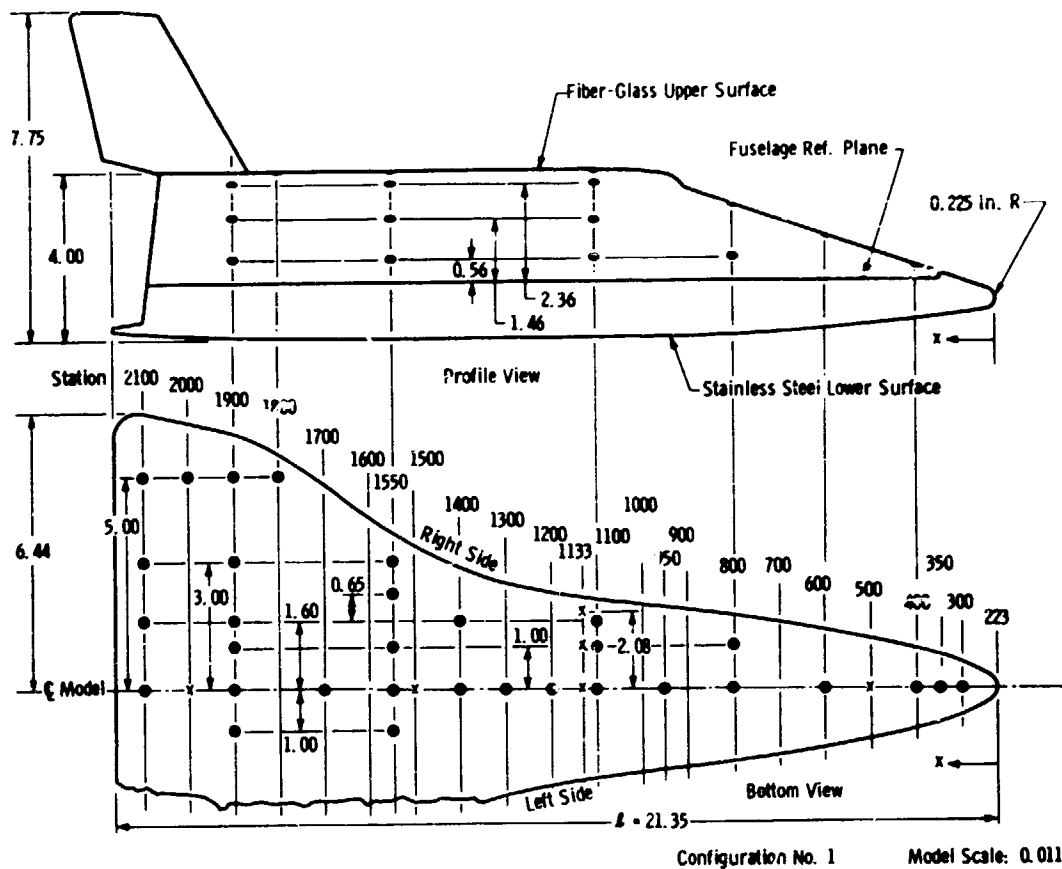


Fig. 7 Instrumentation Layout of Tunnel F Orbiter Model

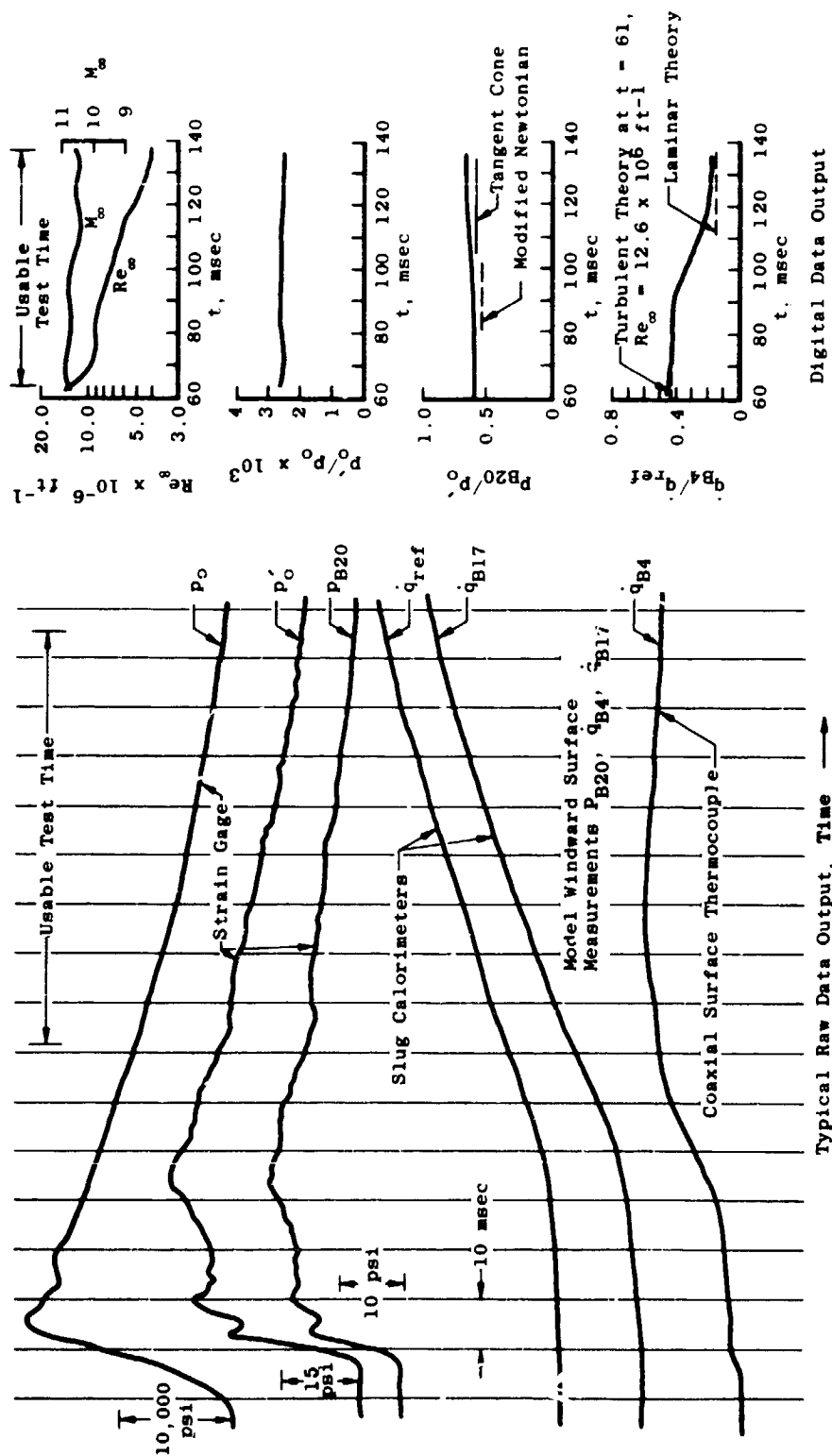


Fig. 8 Typical Timewise Variation of Tunnel F Conditions and Model Data

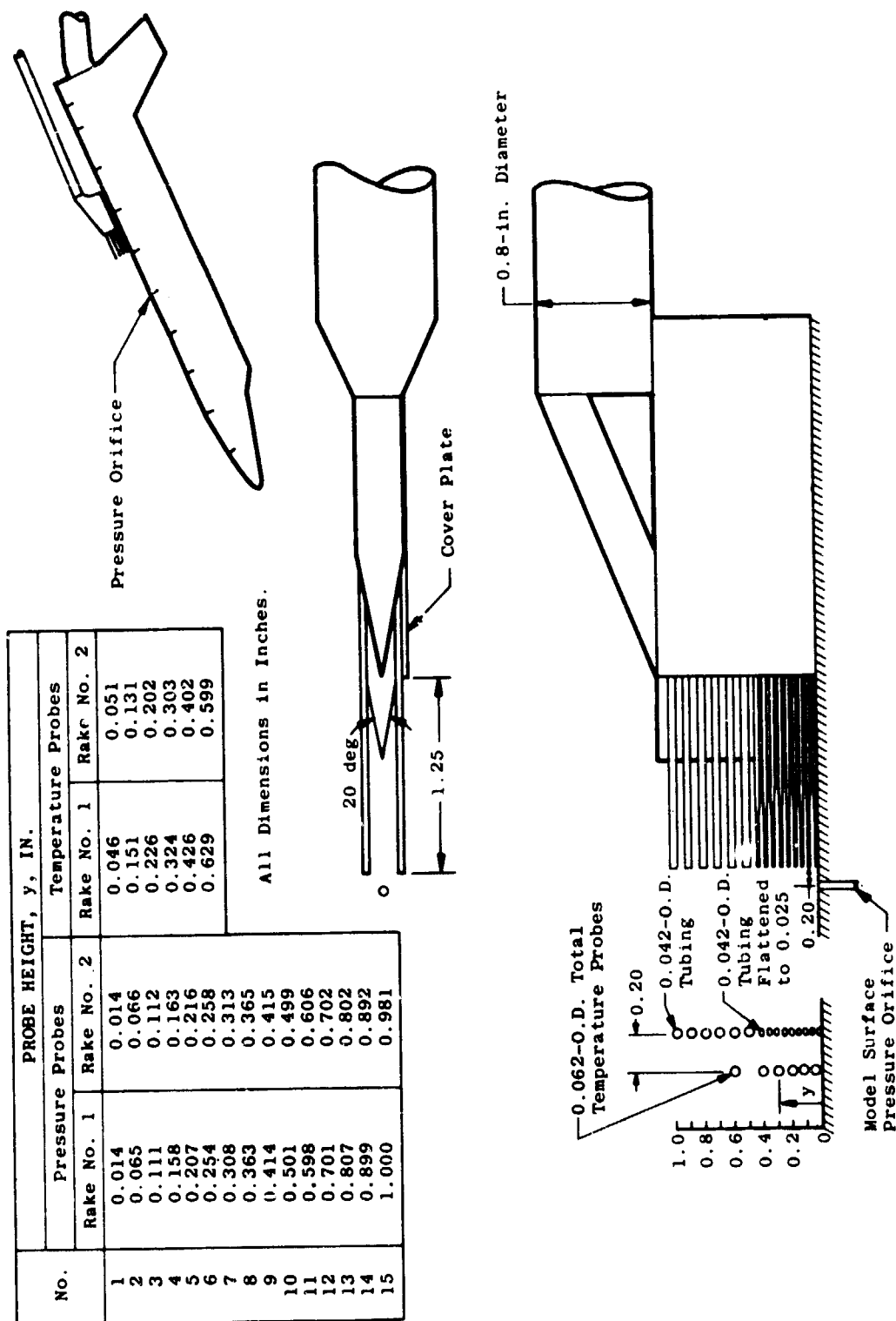


Fig. 9 Probe-Rakes and Support (Tunnel B)

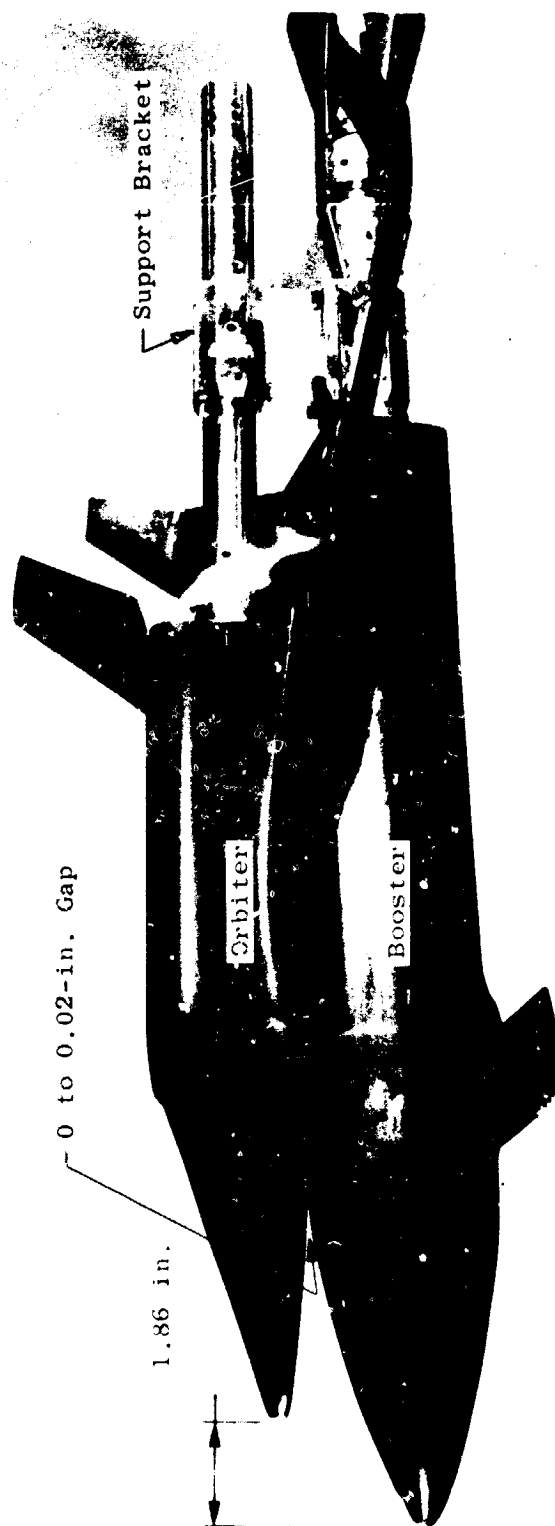
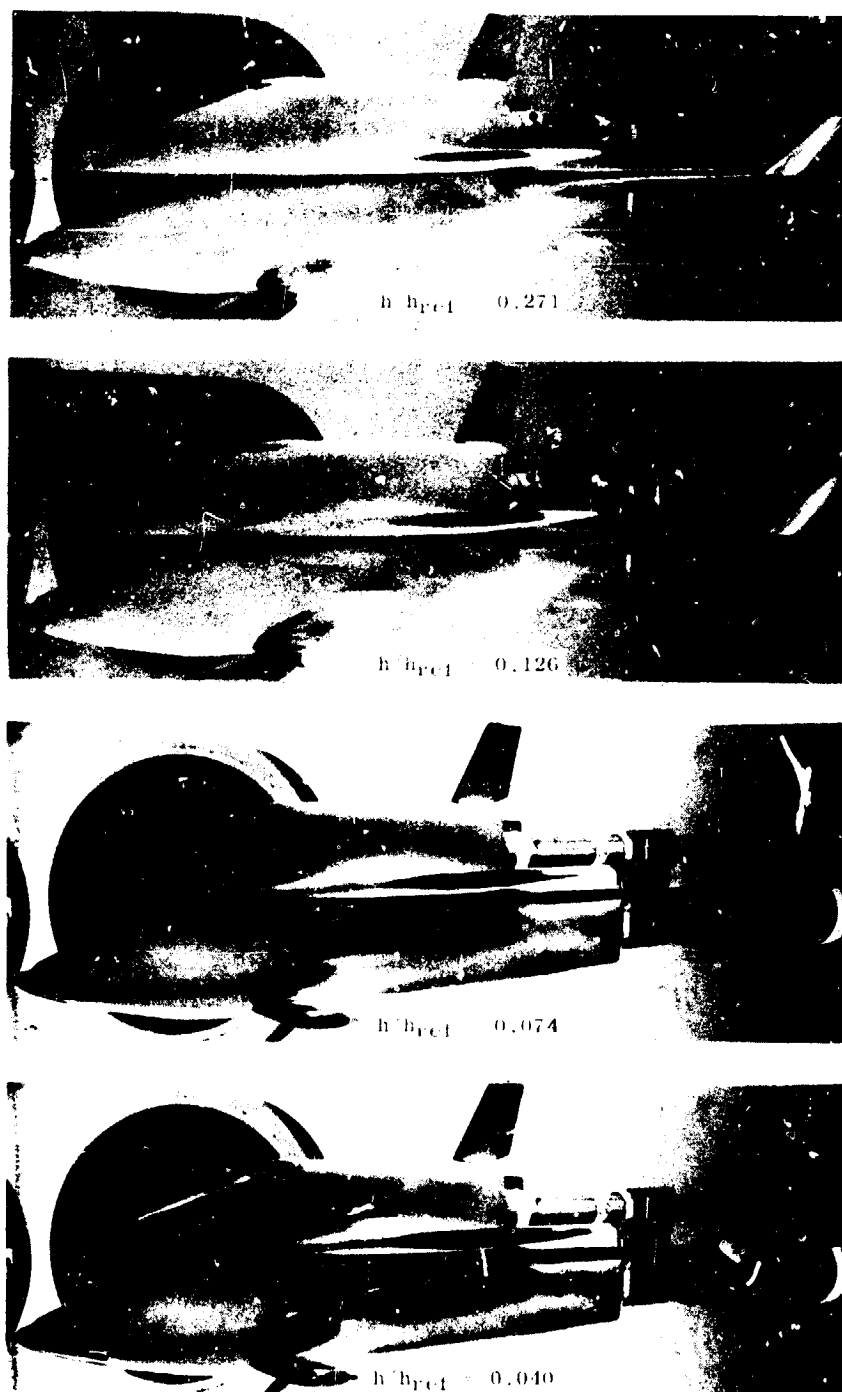


Fig. 10 Photograph of Mated Configuration



**Fig. 11 Phase-Change Paint Photographs of Mated Configurations
at $\alpha = 0$, $M_\infty = 9.0$, $Re_\infty = 3.7 \times 10^6 \text{ ft}^{-1}$**

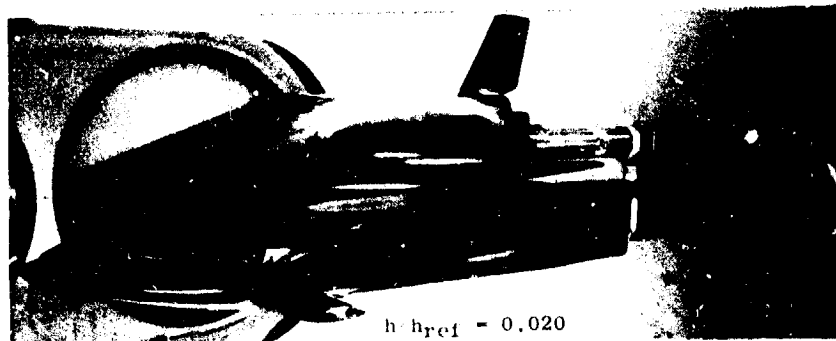
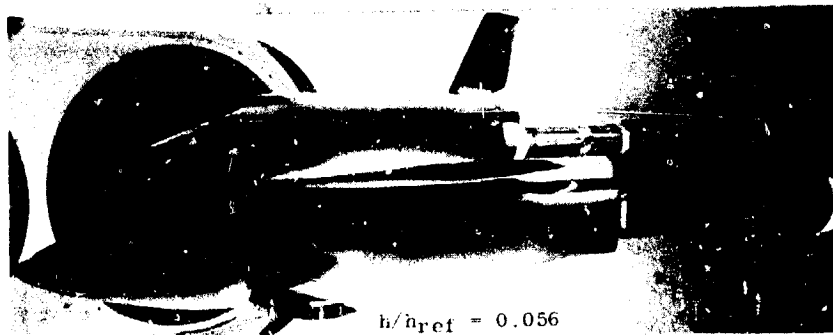
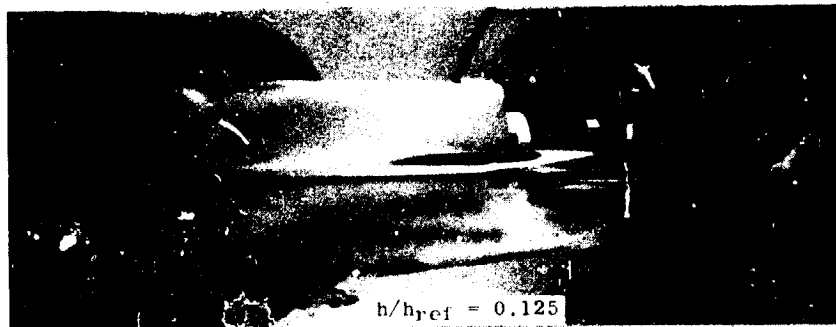
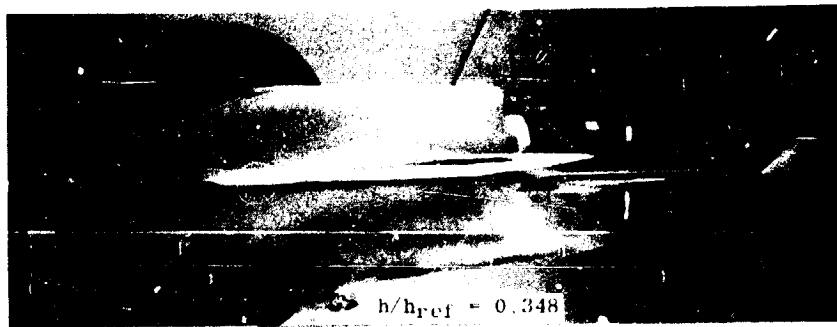


Fig. 12 Phase-Change Paint Photographs of Mated Configurations
at $\alpha = 0$, $M_\infty = 8$, $Re_\infty = 2.5 \times 10^6 \text{ ft}^{-1}$

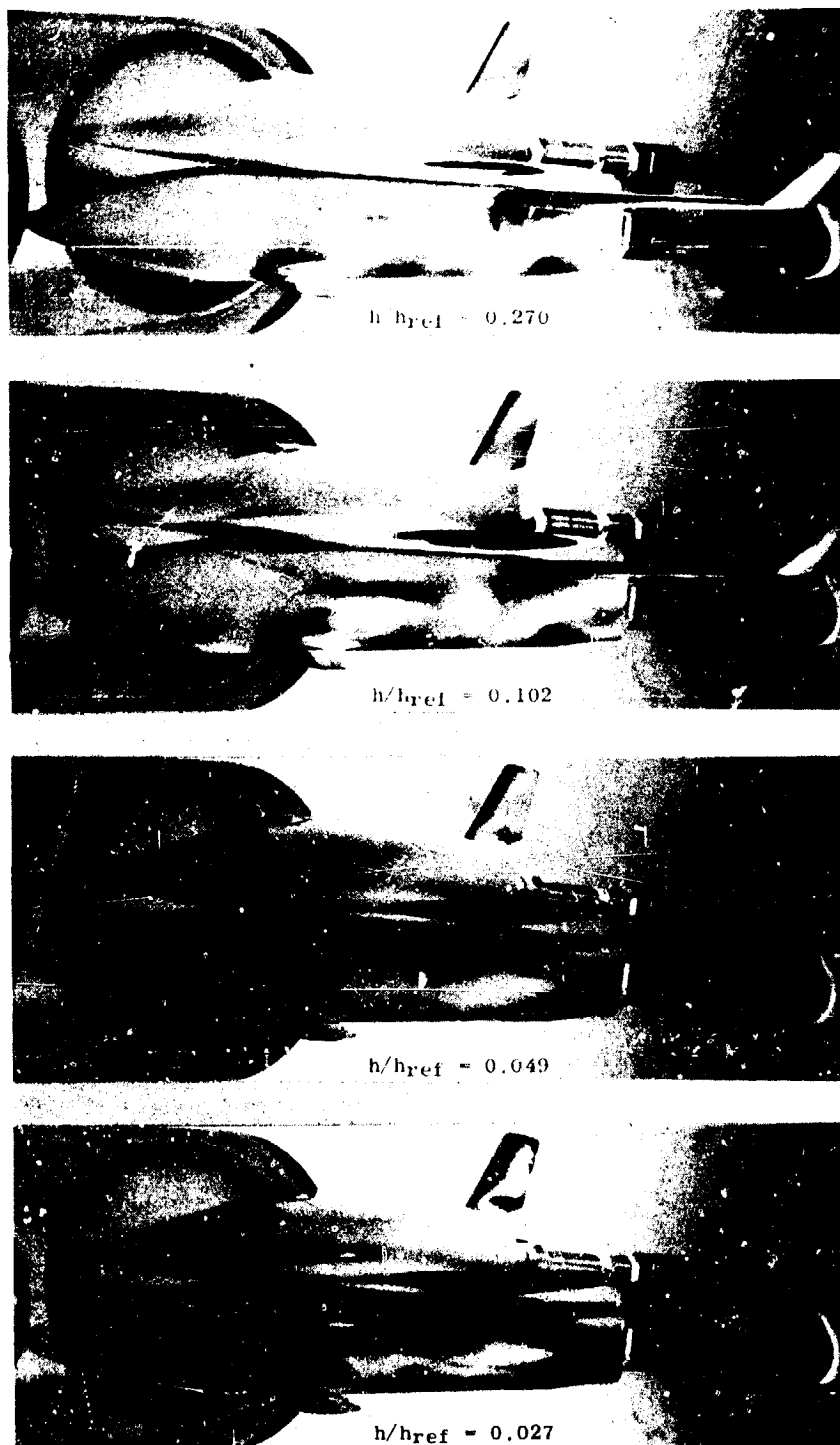


Fig. 13 Phase-Change Paint Photographs of Mated Configurations
at $\alpha = +5$, $M_\infty = 8$, $Re_\infty = 2.5 \times 10^6 \text{ ft}^{-1}$

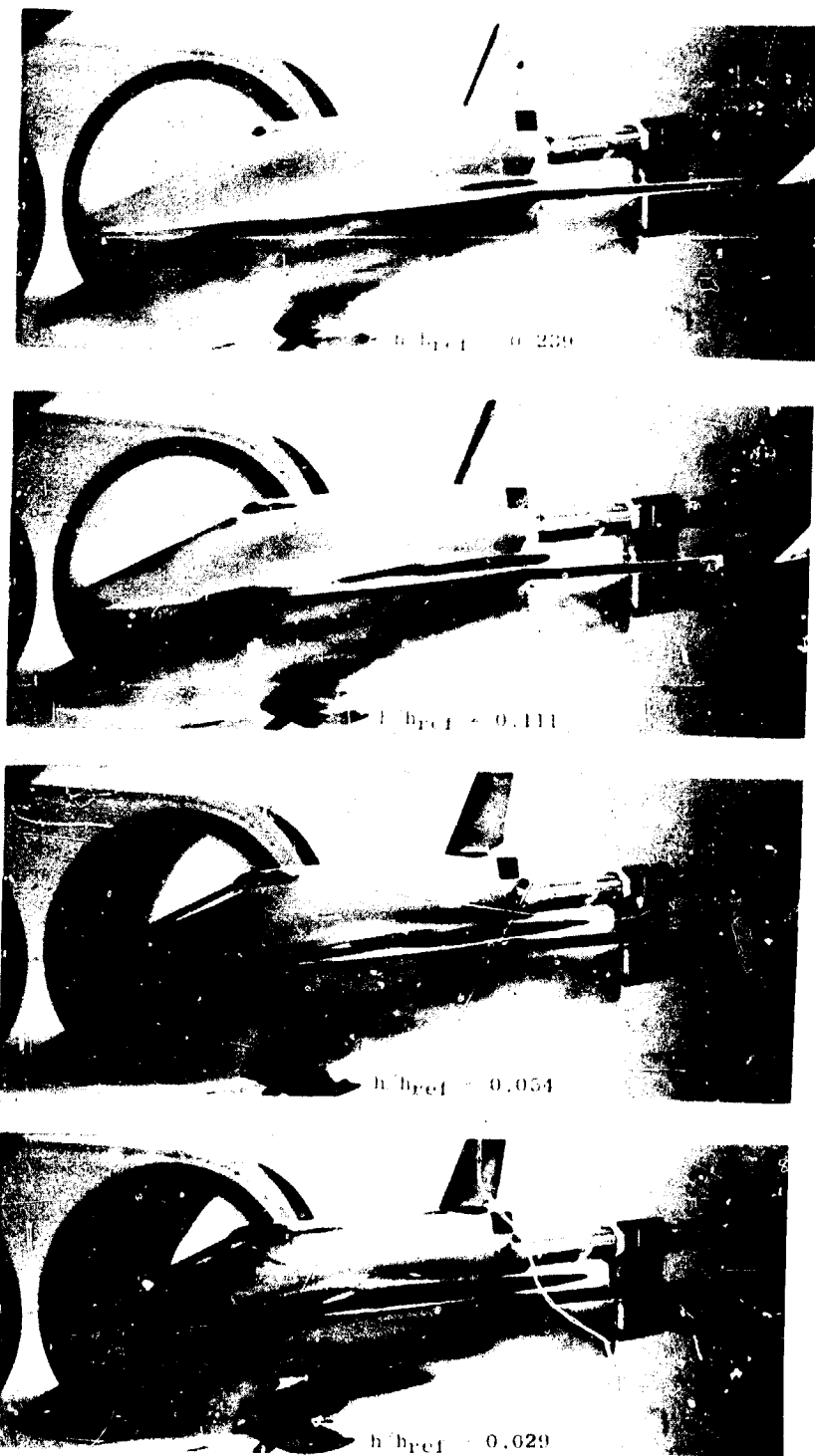
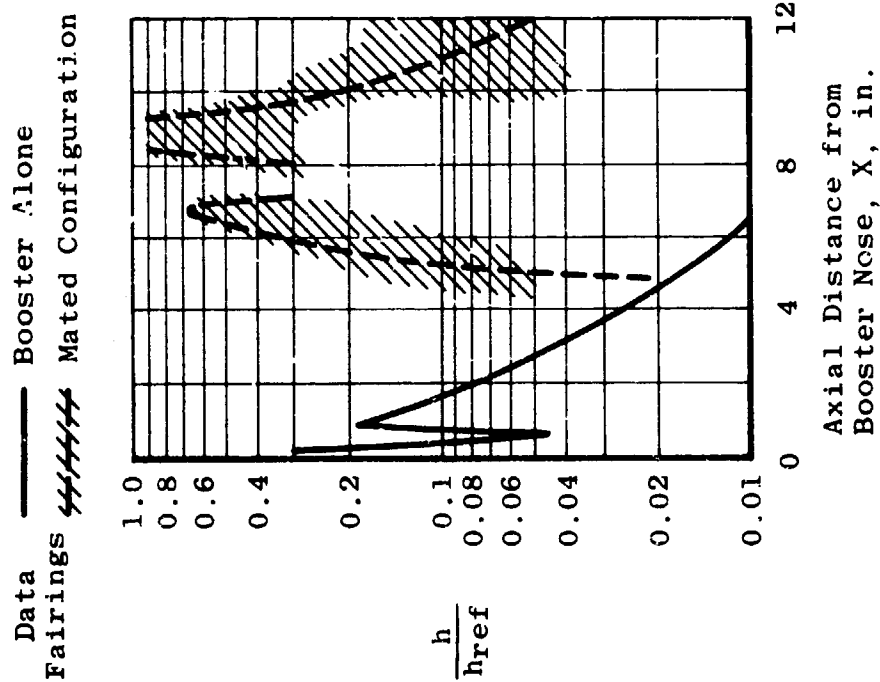


Fig. 14 Phase-Change Paint Photographs of Mated Configurations
at $\alpha = -5$, $M_\infty = 8$, $Re_\infty = 2.5 \times 10^6 \text{ ft}^{-1}$



a. Booster Top Centerline Distributions



b. Posttest Photograph of Interference Region

Fig. 15 Mated Configuration Interference Heating at $\alpha = 0$, $M_\infty = 8$

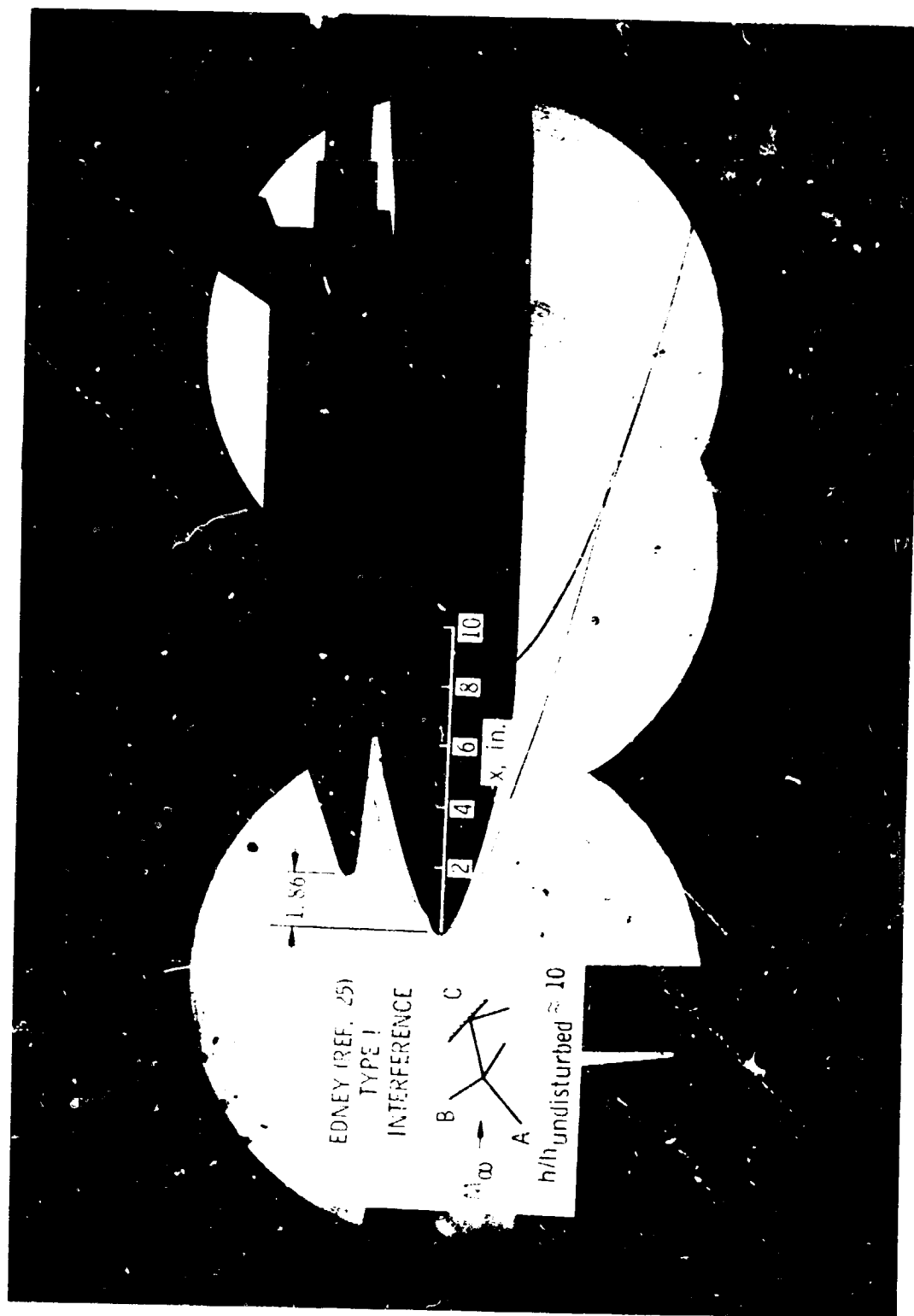


Fig. 16 Composite Shadowgraph of Mated Configuration at $\alpha = 0$, $Re_{\infty} = 2.5 \times 10^6 \text{ ft}^{-1}$, $M_{\infty} = 8$

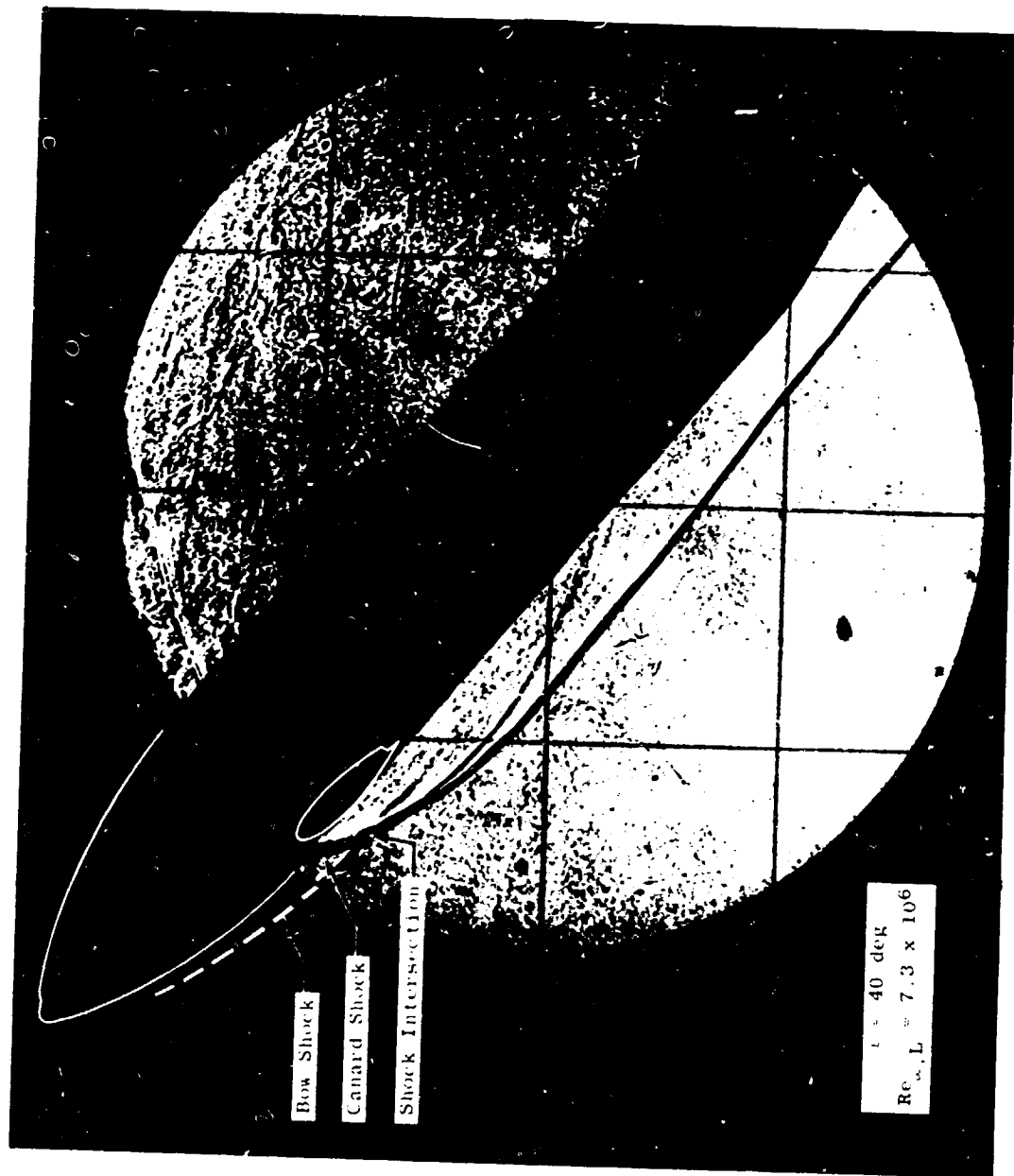


Fig. 17 Typical Booster Reentry Shadowgraph at $M_{\infty} = 8$

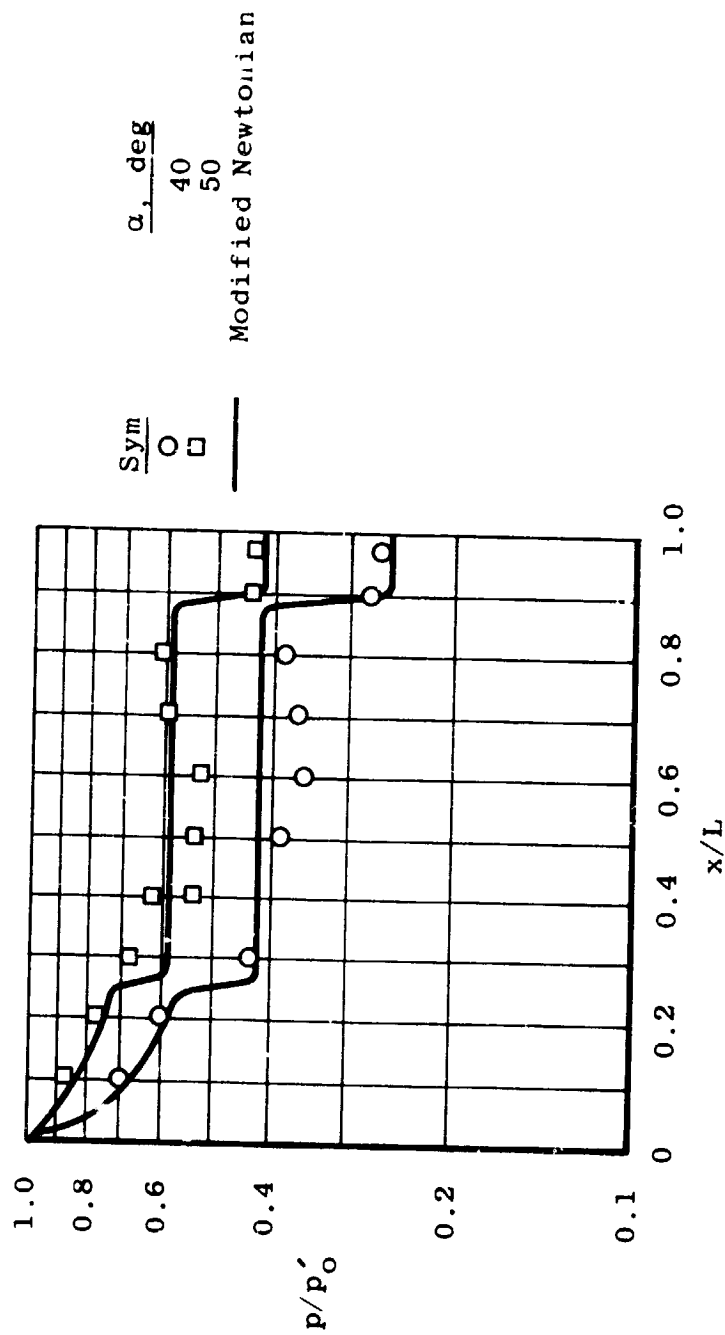
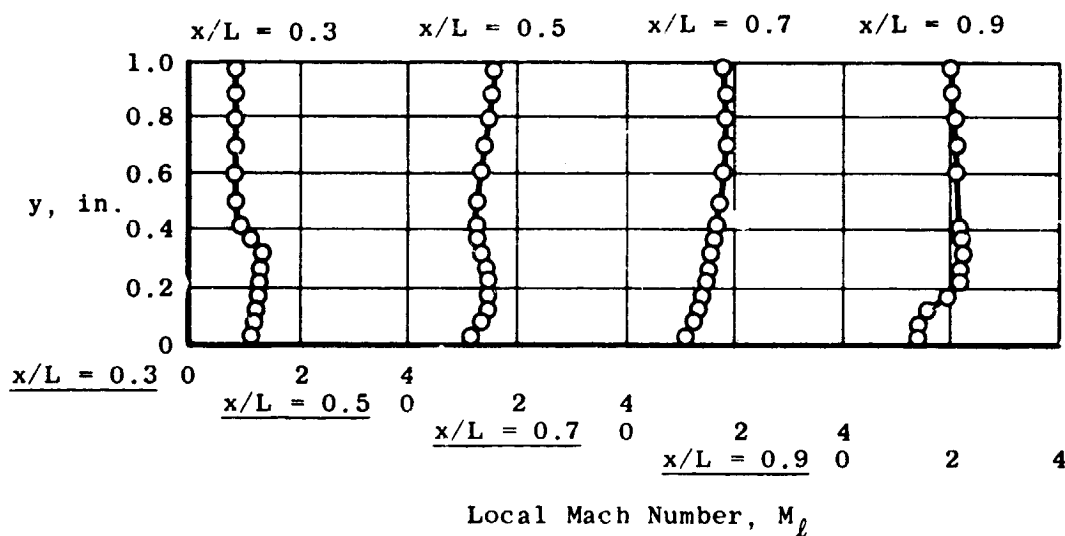
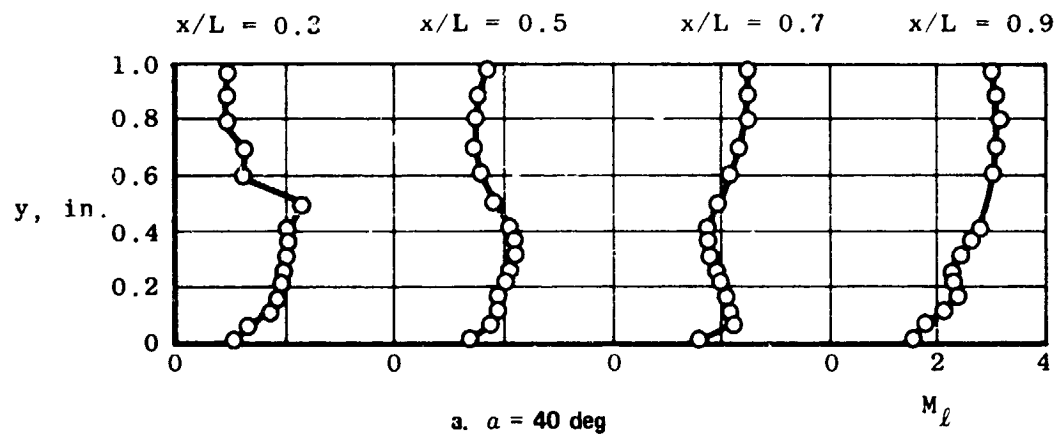


Fig. 18 Booster Windward Centerline Pressure Distributions
at $M_\infty = 8$, $Re_{\infty, L} = 7.3 \times 10^6$



b. $\alpha = 50$ deg

**Fig. 19 Booster Windward Centerline Mach Number Profiles
at $M_\infty = 8$ and $Re_{\infty,L} = 7.3 \times 10^6$**



Fig. 20 Typical Phase-Change Paint Photograph of Booster Bottom Surface
at $M_\infty = 8$, $\alpha = 50$ deg

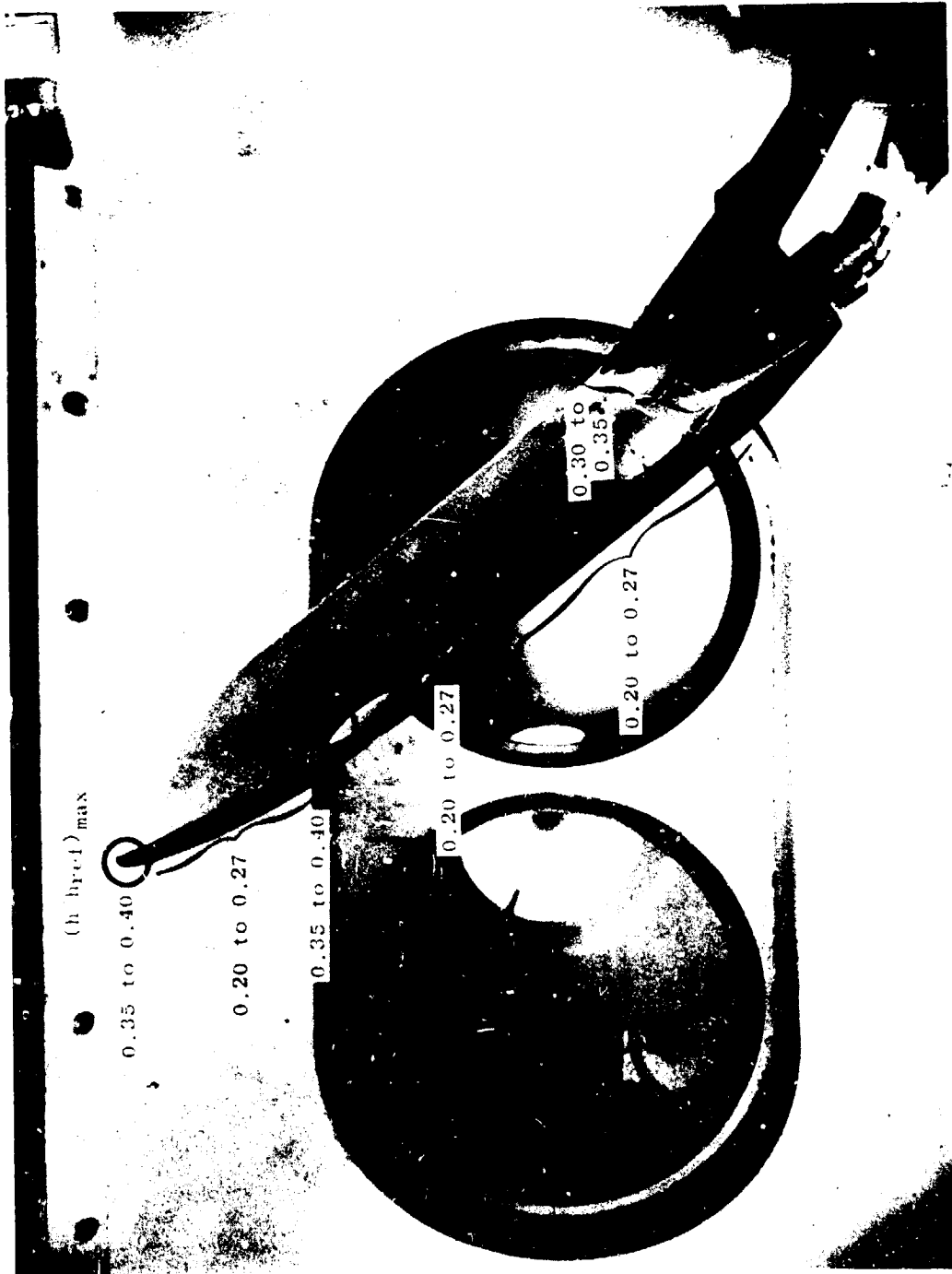


Fig. 21 Typical Side View Phase-Change Paint Photograph of Booster
at $M_\infty = 5$, $\alpha = 50$ deg

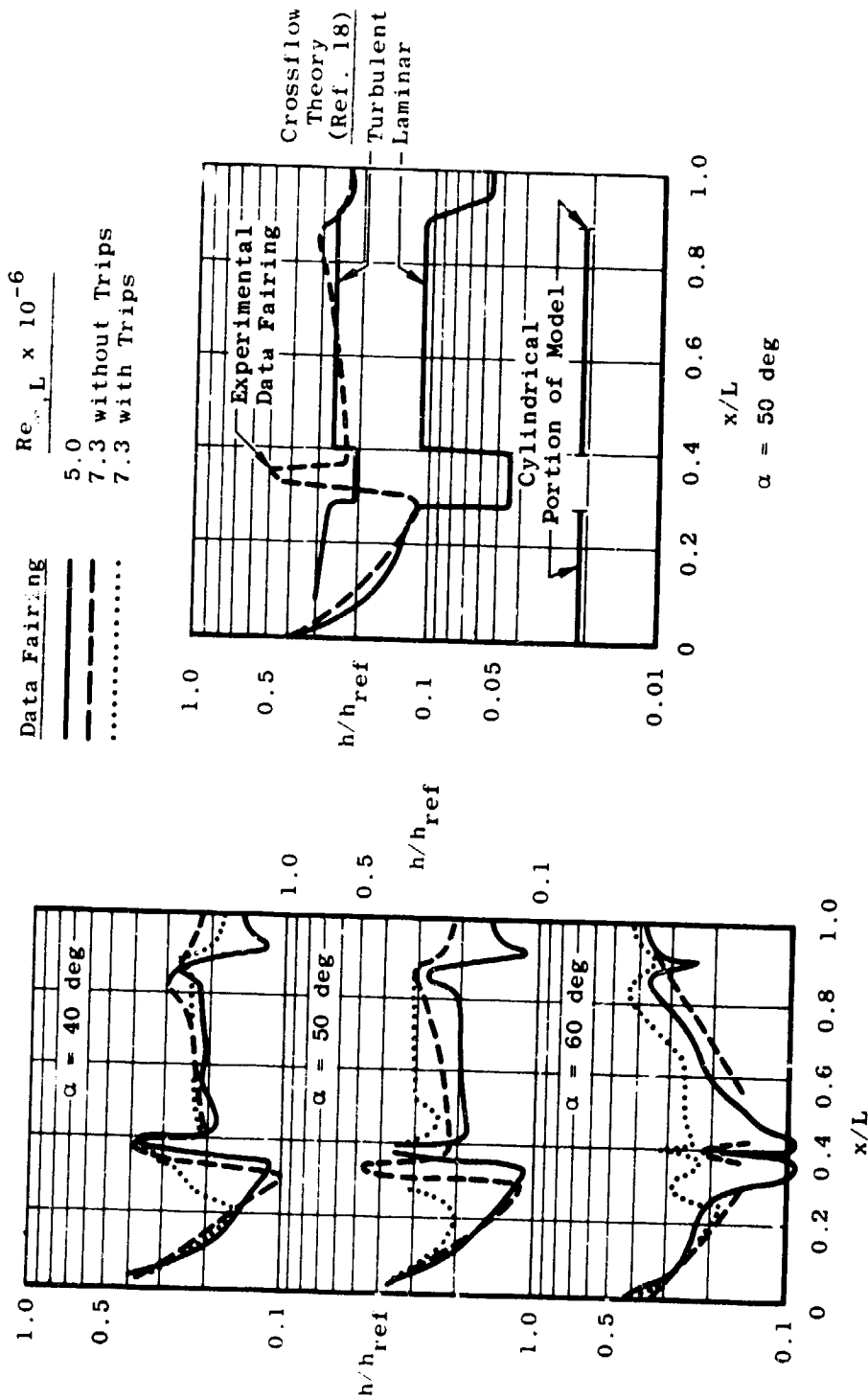


Fig. 22 Booster Windward Centerline Heat Transfer Distributions, $M_\infty = 8$



a. $\alpha = 20$ deg, $h/h_{ref} = 0.0217$, $Re_{\infty,L} = 4.5 \times 10^6$



b. $\alpha = 40$ deg, $h/h_{ref} = 0.0175$, $Re_{\infty,L} = 4.5 \times 10^6$



c. $\alpha = 60$ deg, $h/h_{ref} = 0.0114$, $Re_{\infty,L} = 4.5 \times 10^6$



d. $\alpha = 40$ deg, $h/h_{ref} = 0.0179$, $Re_{\infty,L} = 6.6 \times 10^6$

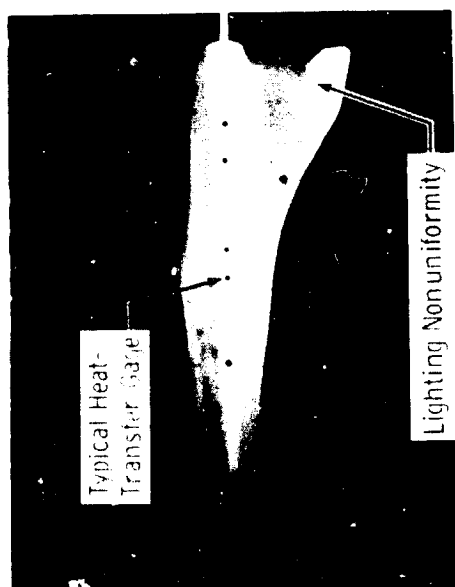
Fig. 23. Orbiter Lee Surface Phase-Change Paint Photographs, $M_\infty = 8$



b. $\alpha = 20$ deg, $Re_{\infty,L} = 9.1 \times 10^6$



d. $\alpha = 50$ deg, $Re_{\infty,L} = 7.3 \times 10^6$



a. $\alpha = 20$ deg, Tare Picture



c. $\alpha = 40$ deg, $Re_{\infty,L} = 9.4 \times 10^6$

Fig. 24 Lee Surface Thermographic Phosphor Photographs, $M_{\infty} = 10.5$

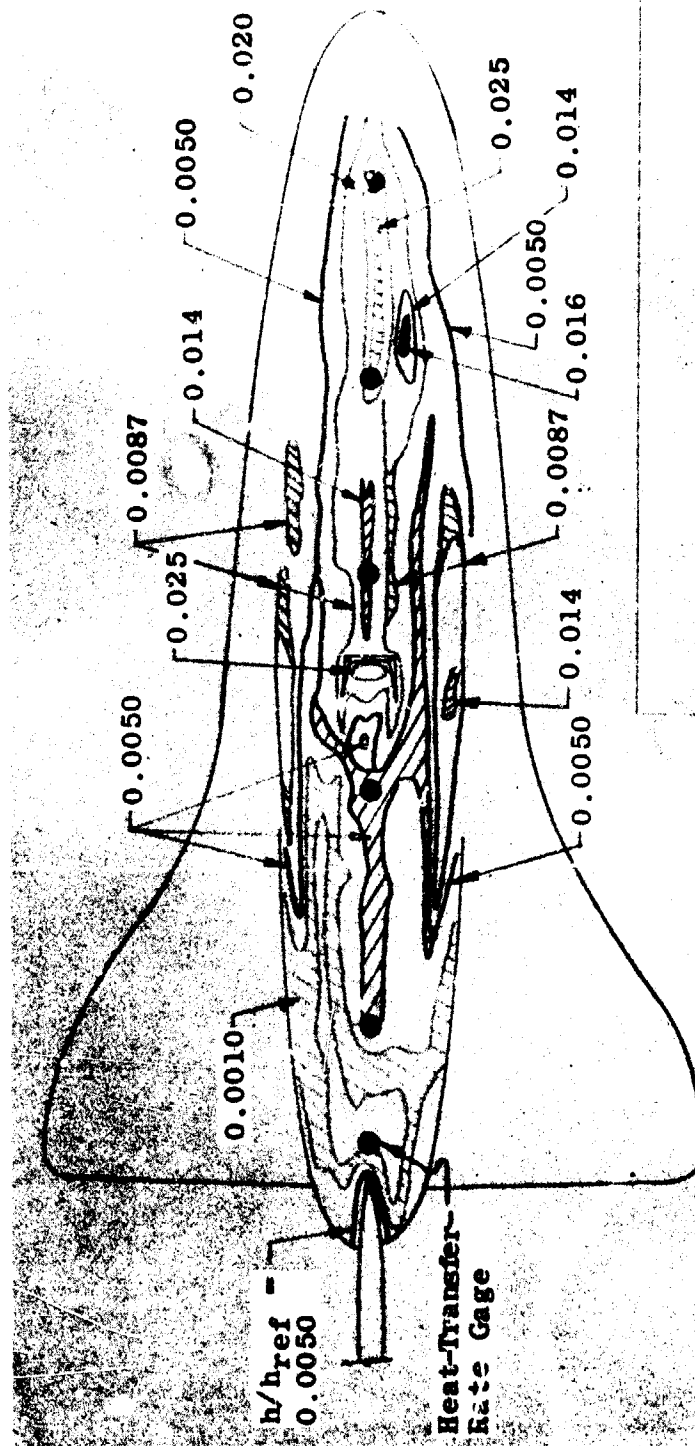
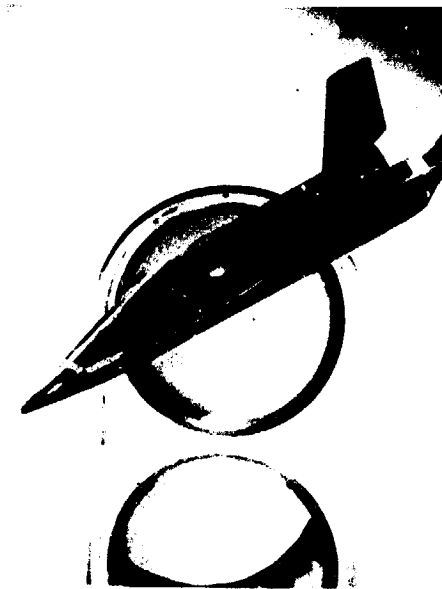


Fig. 25 Top Surface Heat Transfer Distributions, $\alpha = 50$ deg, $M_\infty = 10.5$, $Re_{\infty,L} = 7.4 \times 10^6$



a. $\alpha = 20$ deg, $h/h_{ref} = 0.0341$, $Re_{\infty,L} = 4.5 \times 10^6$



c. $\alpha = 60$ deg, $h/h_{ref} = 0.0077$, $Re_{\infty,L} = 4.5 \times 10^6$

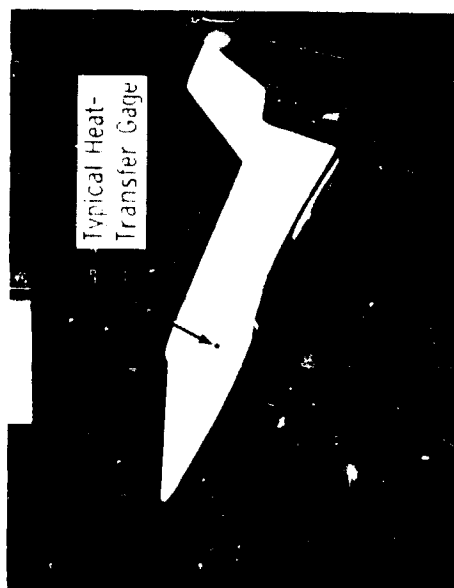


b. $\alpha = 40$ deg, $h/h_{ref} = 0.0132$, $Re_{\infty,L} = 4.5 \times 10^6$

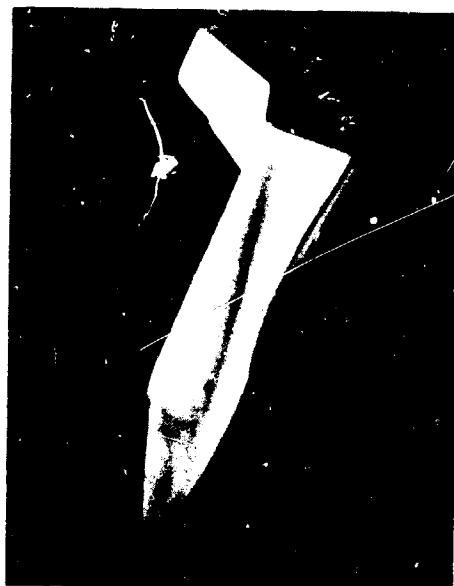


d. $\alpha = 40$ deg, $h/h_{ref} = 0.0093$, $Re_{\infty,L} = 6.6 \times 10^6$

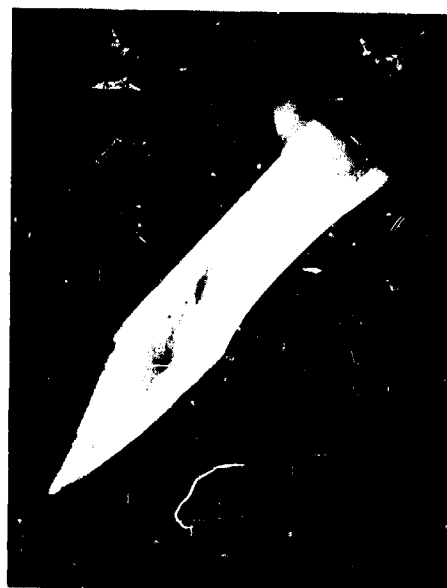
Fig. 26 Orbiter Side Panel Phase-Change Paint Photographs, $M_{\infty} = 8$



a. $\alpha = 20$ deg, Tare Picture



b. $\alpha = 20$ deg, $Re_{\infty,L} = 9.1 \times 10^6$



c. $\alpha = 40$ deg, $Re_{\infty,L} = 9.1 \times 10^6$



d. $\alpha = 50$ deg, $Re_{\infty,L} = 7.3 \times 10^6$

Fig. 27 Side Panel Thermographic Phosphor Photographs, $M_{\infty} = 10.5$

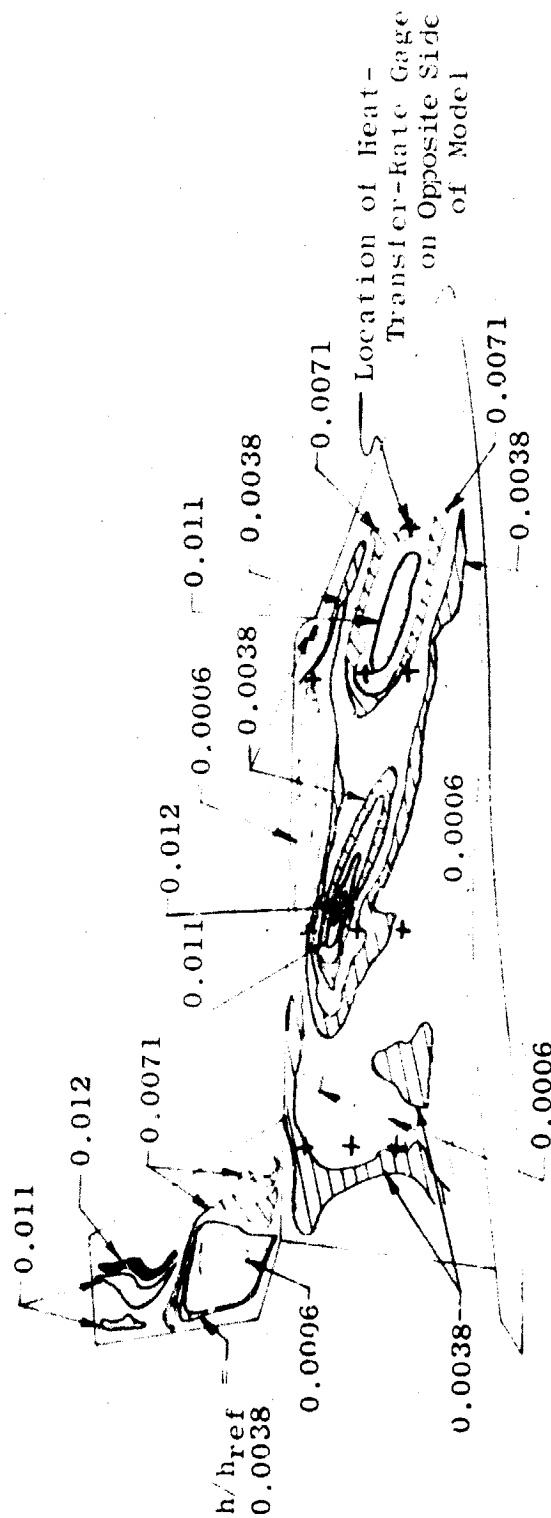
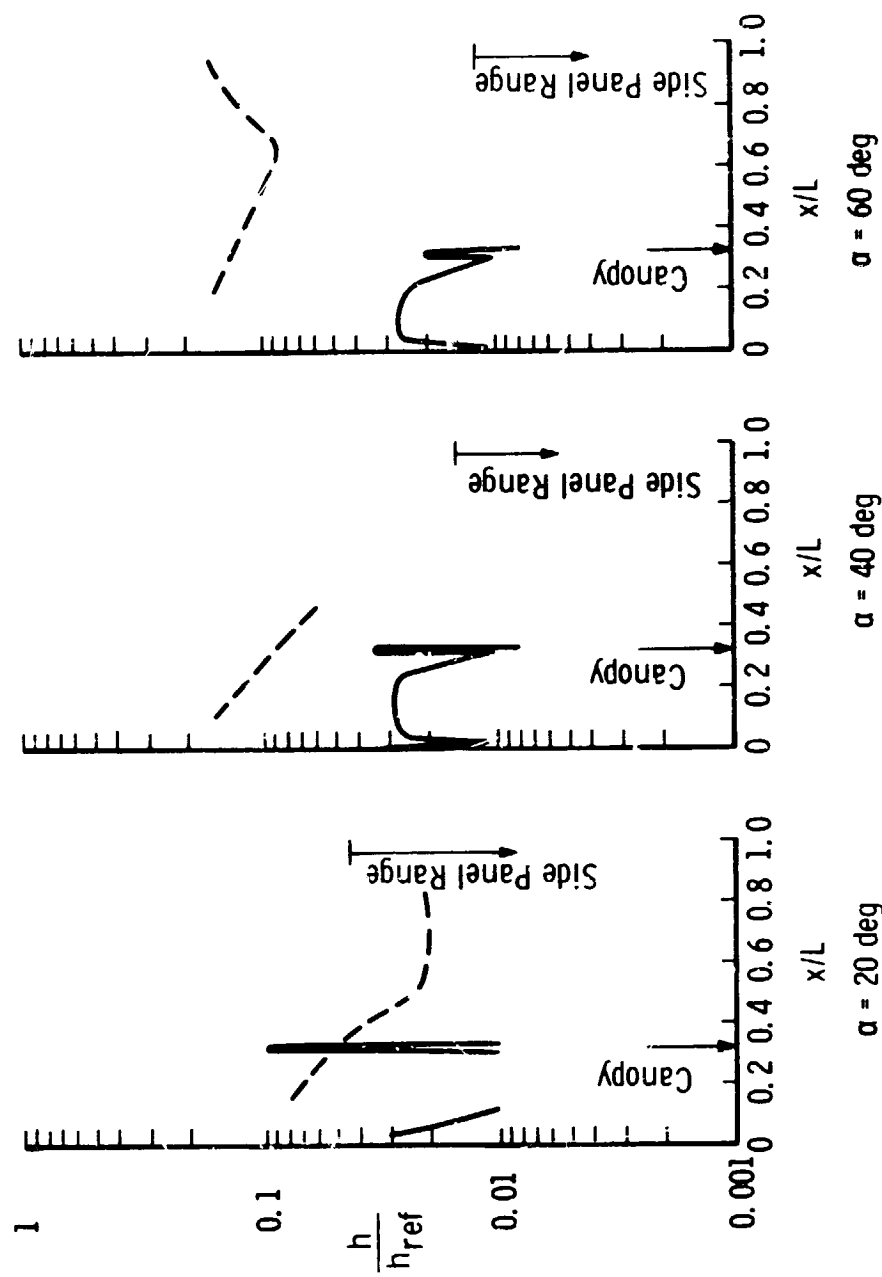


Fig. 28 Side Panel Heat Transfer Distributions, $\alpha = 30$ deg, $M_\infty = 10.3$, $Re_{\infty,L} = 4.9 \times 10^6$

— Lee-Side Data Fairing
 --- Windward Data Fairing

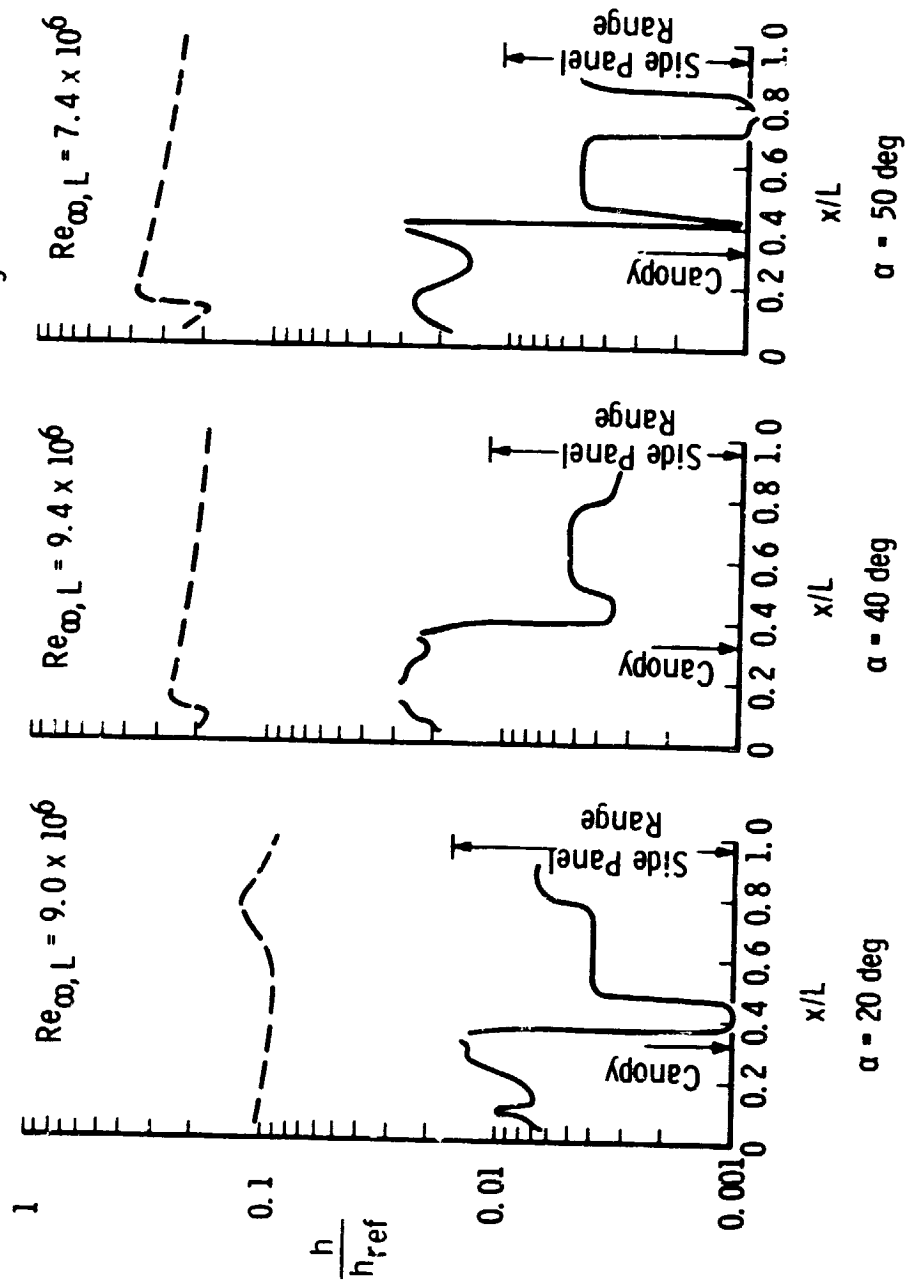


a. Tunnel B, $M_\infty = 8$, $Re_{\infty,L} = 4.5 \times 10^6$

Fig. 29 Comparison of Windward and Lee-Side Centerline Heating Distributions

— Lee-Side Data Fairing

- - - Windward Data Fairing



b. Tunnel F, $M_{\infty} = 10.5$
Fig. 29 Concluded

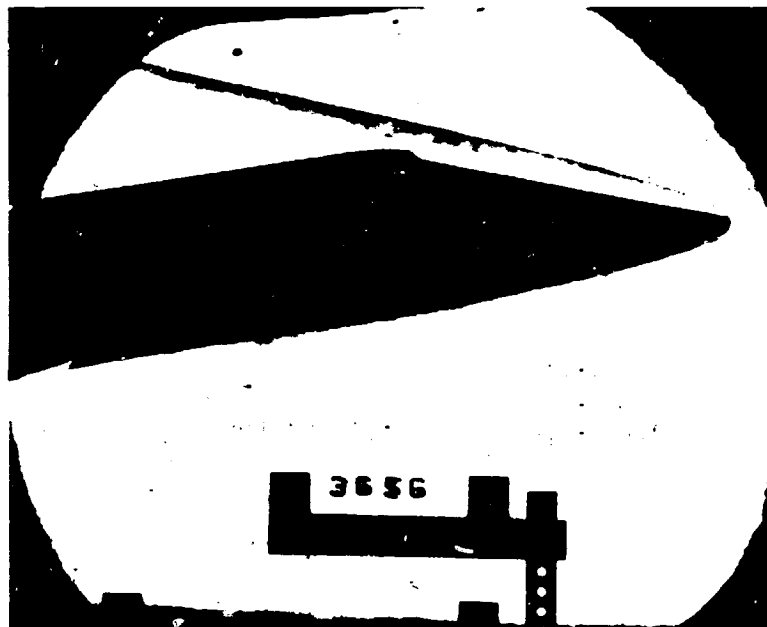


Fig. 30 Flow Field Photographs of Orbiter

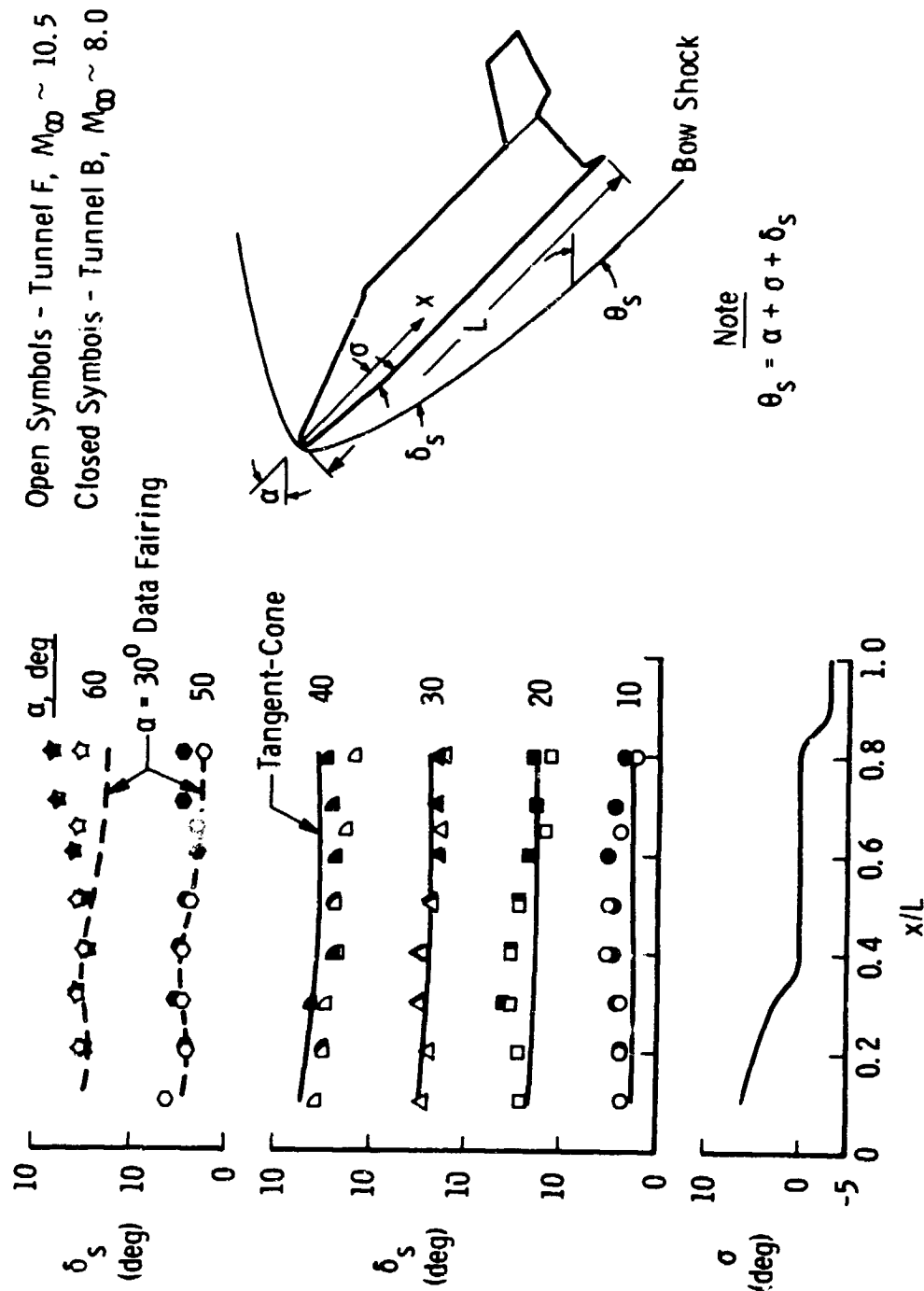


Fig. 31 Comparison of Experimental and Theoretical Shock Angles

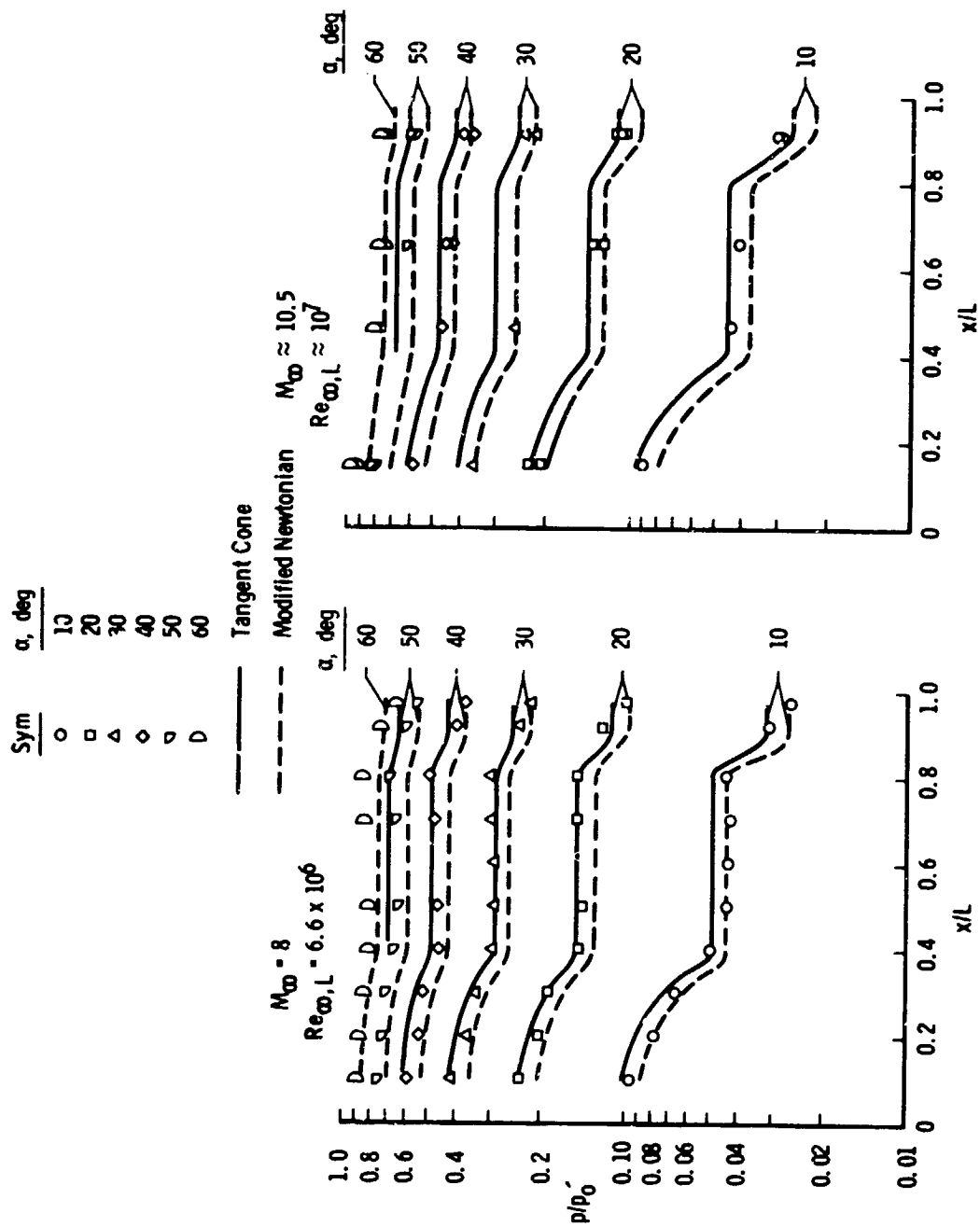


Fig. 32 Orbiter Windward Centerline Pressure Distributions

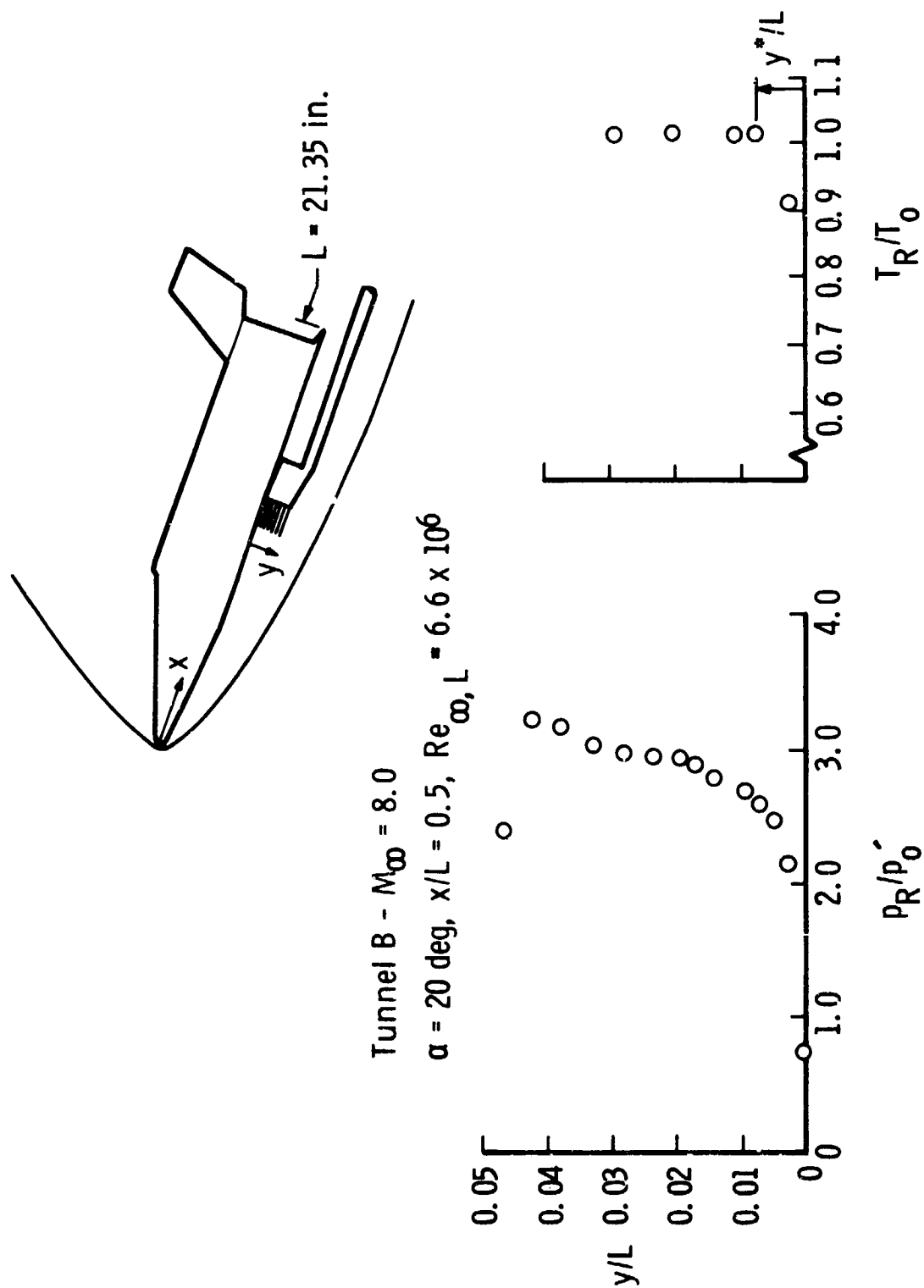


Fig. 33 Typical Orbiter Pitot Pressure and Total Temperature Profiles

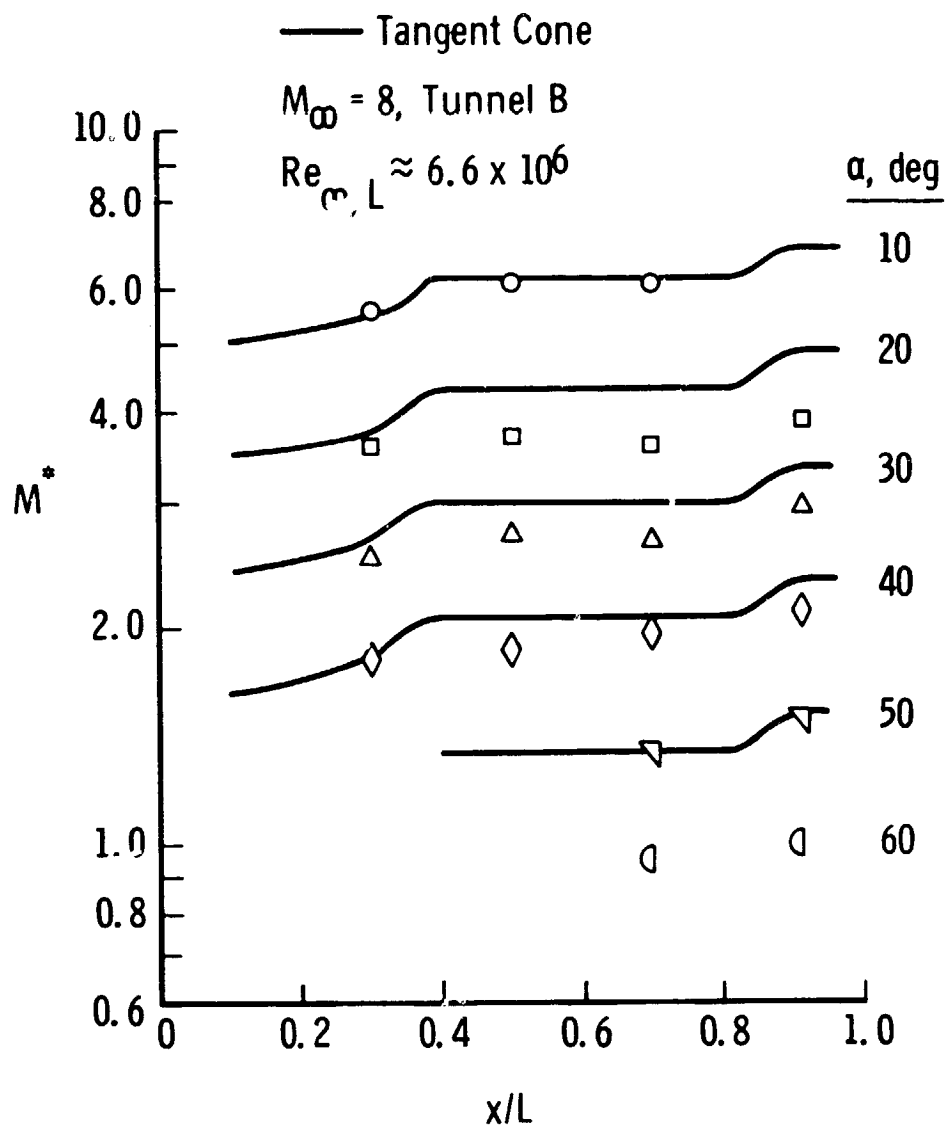
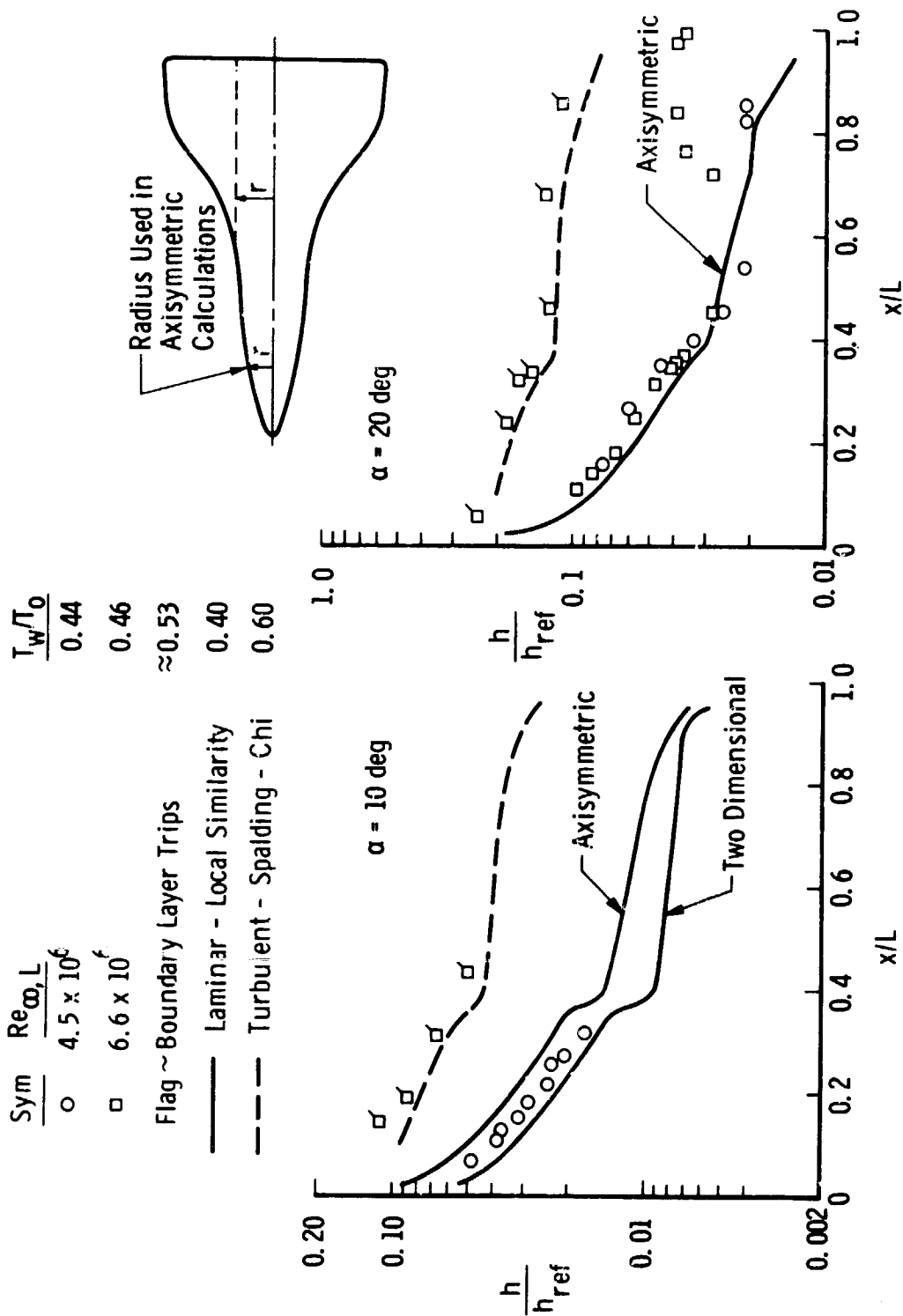
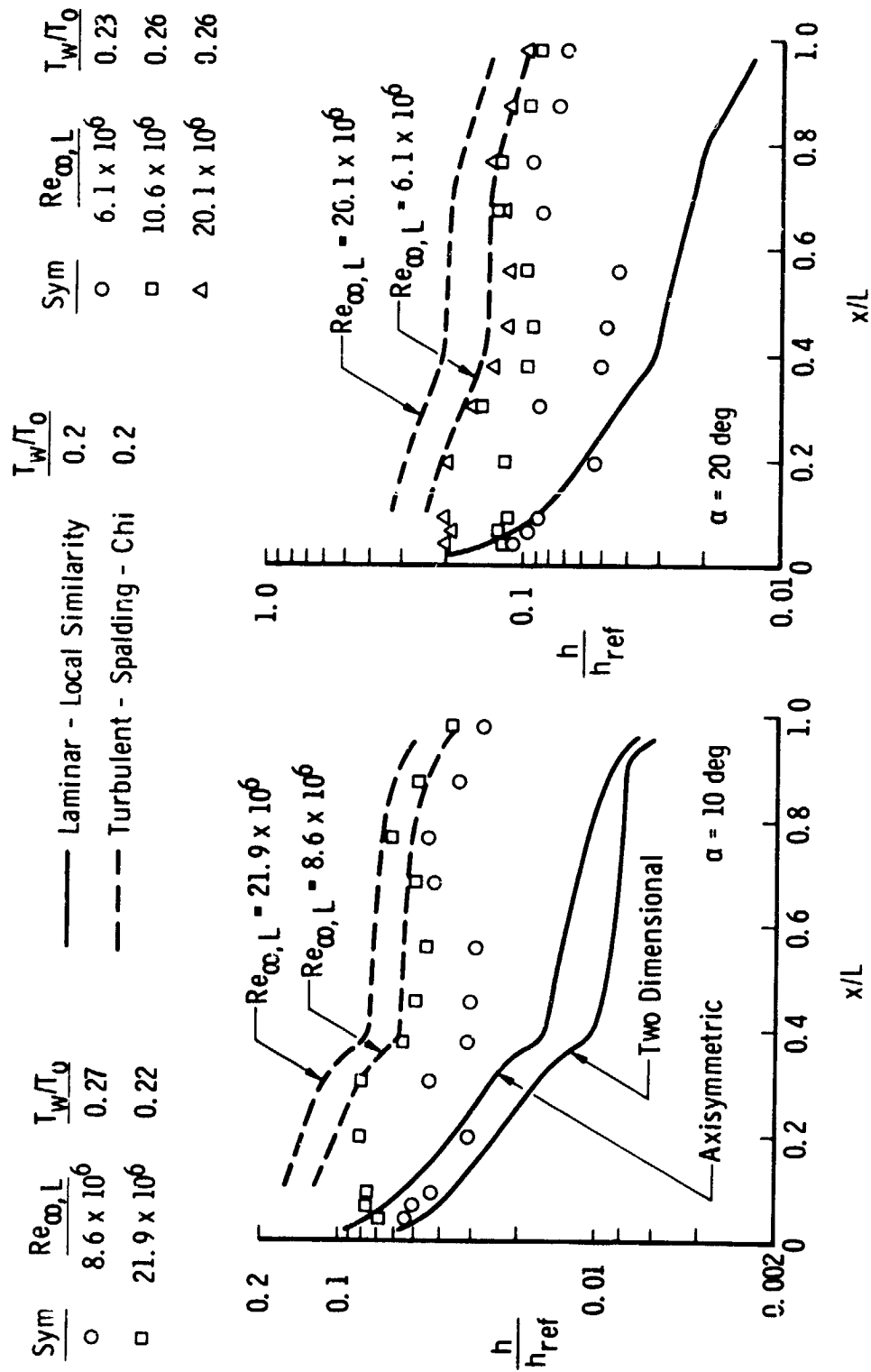


Fig. 34. Orbiter Windward Centerline Inviscid Mach Number Distributions



a. $M_\infty = 8$, $\alpha = 10$ and 20 deg

Fig. 35 Comparison of Experimental and Theoretical Orbiter Windward Centerline Heating Distributions



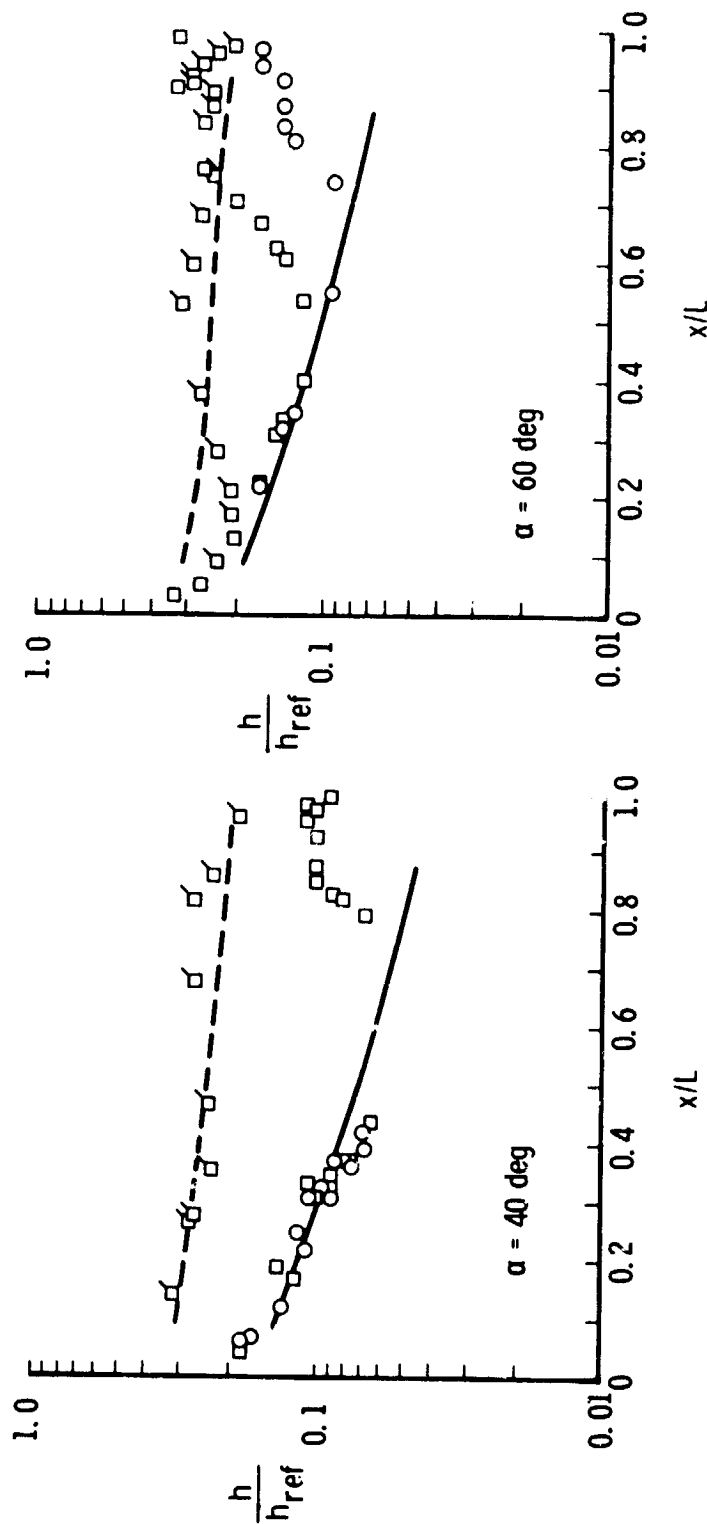
b. $M_\infty = 10.7$, $\alpha = 10$ and 20°
Fig. 35 Continued

Cross-Flow Theory		T_w/π_0
—	Laminar	0.40
---	Turbulent	0.60

T_w/π_0
≈ 0.53
≈ 0.53
≈ 0.60

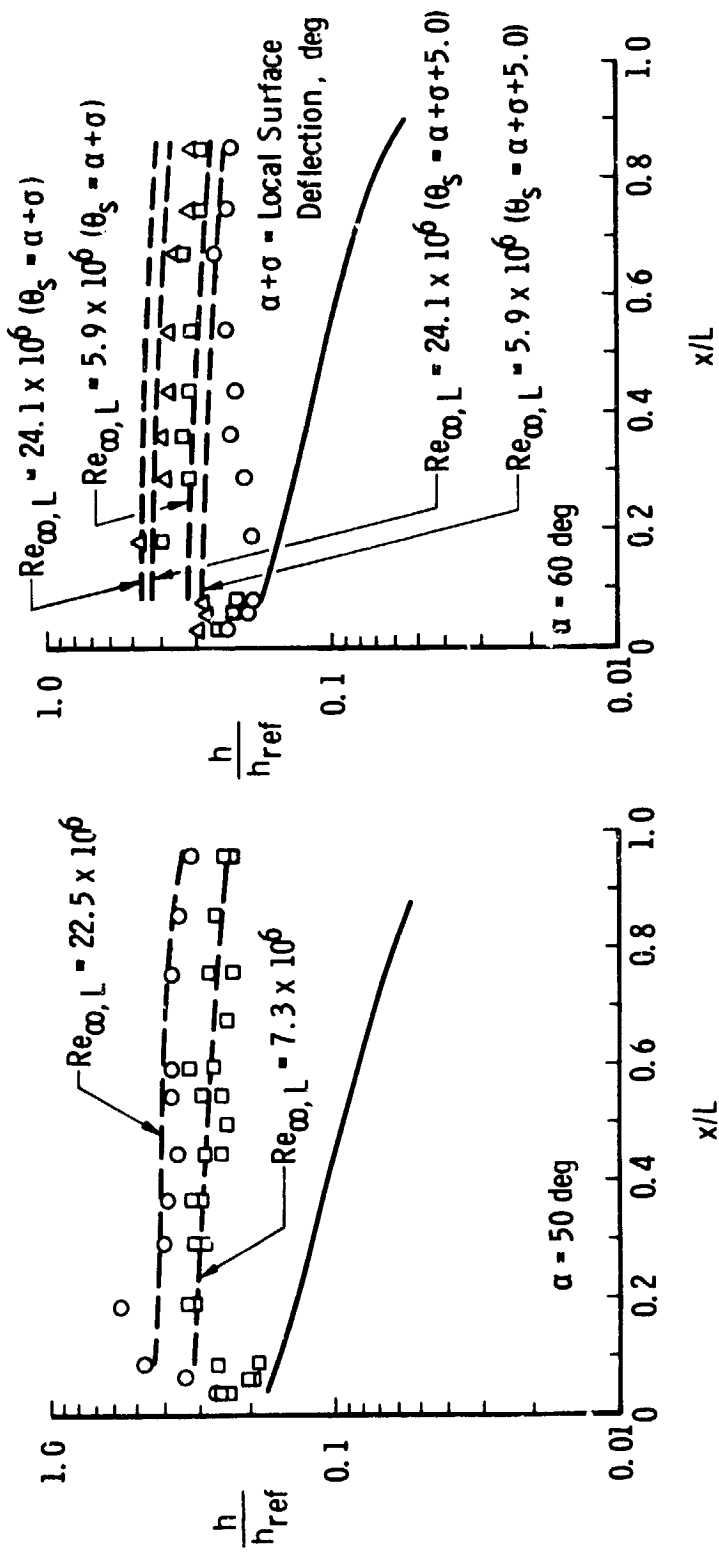
Sym	$Re_{\omega_2 L}$
○	4.5×10^6
□	6.6×10^6

Flag ~ Boundary Layer Trips



c. $M_\infty = 8$, $\alpha = 40$ and 60 deg
Fig. 35 Continued

Sym	$Re_{\infty, L}$	T_w/T_o	Cross-Flow Theory	T_w/T_o	Sym	$Re_{\infty, L}$	T_w/T_o
○	6.1×10^6	0.22	— Laminar	Same	○	5.9×10^6	0.18
□	13.1×10^6	0.27	--- Turbulent	as Data	□	12.9×10^6	0.23
					△	24.1×10^6	0.29



d. $M_\infty = 10.5$, $\alpha = 50$ and 60 deg
Fig. 35 Concluded

Run 3825

Sym	Time, msec	M_∞	$Re_\infty \times 10^{-6}$	$Re_\infty \times 10^{-6}$	x	$Re_\infty, L \times 10^{-6}$	x_t , in.
○	55	10.7	5.60	9.97	1.07		
□	85	10.7	3.85	6.84	2.45		
▽	139	10.9	2.48	4.41	8.55		
◇	148	10.9	2.24	3.98	11.72		
◇	151	10.9	2.13	3.79	19.20		

Note: J ion location for
 $Re_\infty = 2.13 \times 10^6 \text{ ft}^{-1}$
 $(x_t/L = 0.90)$ was only
marginally affected by
roughness.

Theory - Turbulent Flow
with Cross Flow (Ref. 18)

$Re_\infty, L \times 10^{-6}$

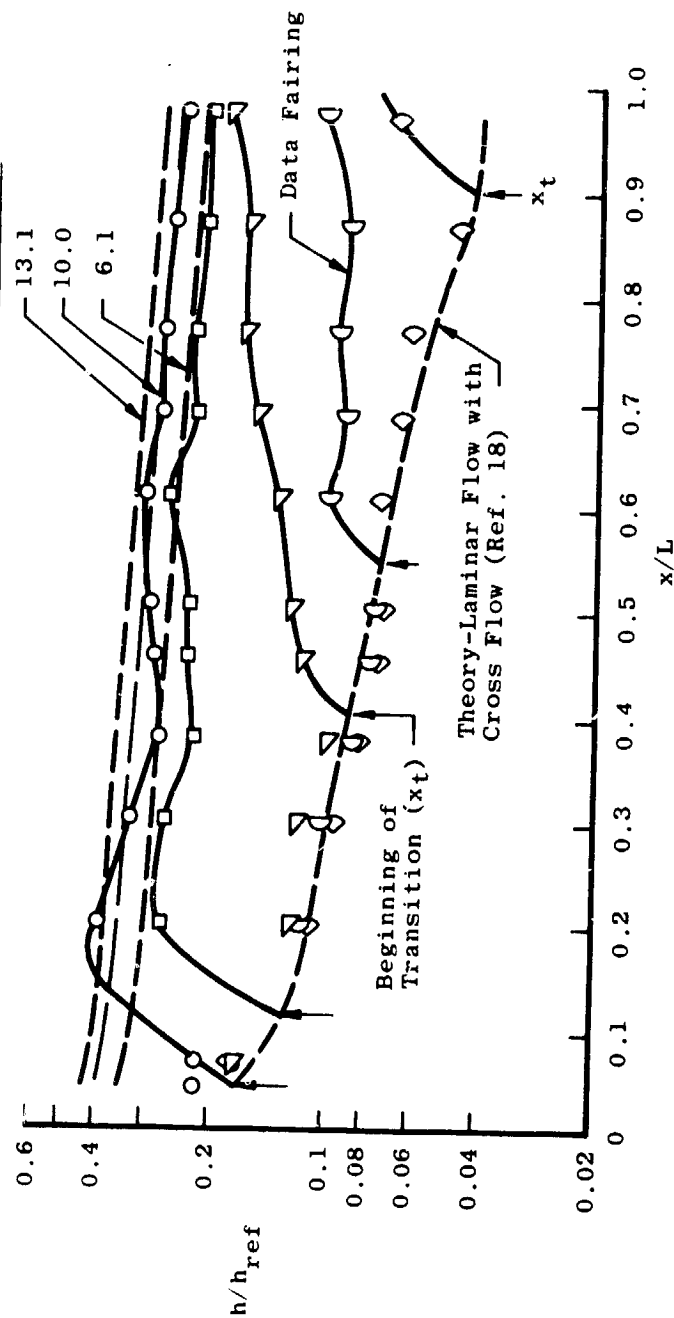


Fig. 36 Laminar and Turbulent Heat Transfer Results from Tunnel F,
Phase II, $M_\infty = 10.8$, $\alpha = 40$ deg

Run 3828

Sym	msec	M_∞	$Re_\infty \times 10^{-6}$	$Re_\infty, L \times 10^{-6}$	$x_t, \text{in.}$
O	85	10.8	6.17	10.97	5.8
△	91	10.8	5.82	10.35	6.9
□	103	10.8	4.82	8.57	9.5
◇	113	10.8	4.47	7.96	10.1
▽	130	10.9	3.86	6.87	11.4
○	152	10.9	3.29	5.86	14.6

Theory - Turbulent Flow
with Cross Flow (Ref. 18)

$Re_\infty, L \times 10^{-6}$

13.1

10.0

6.1

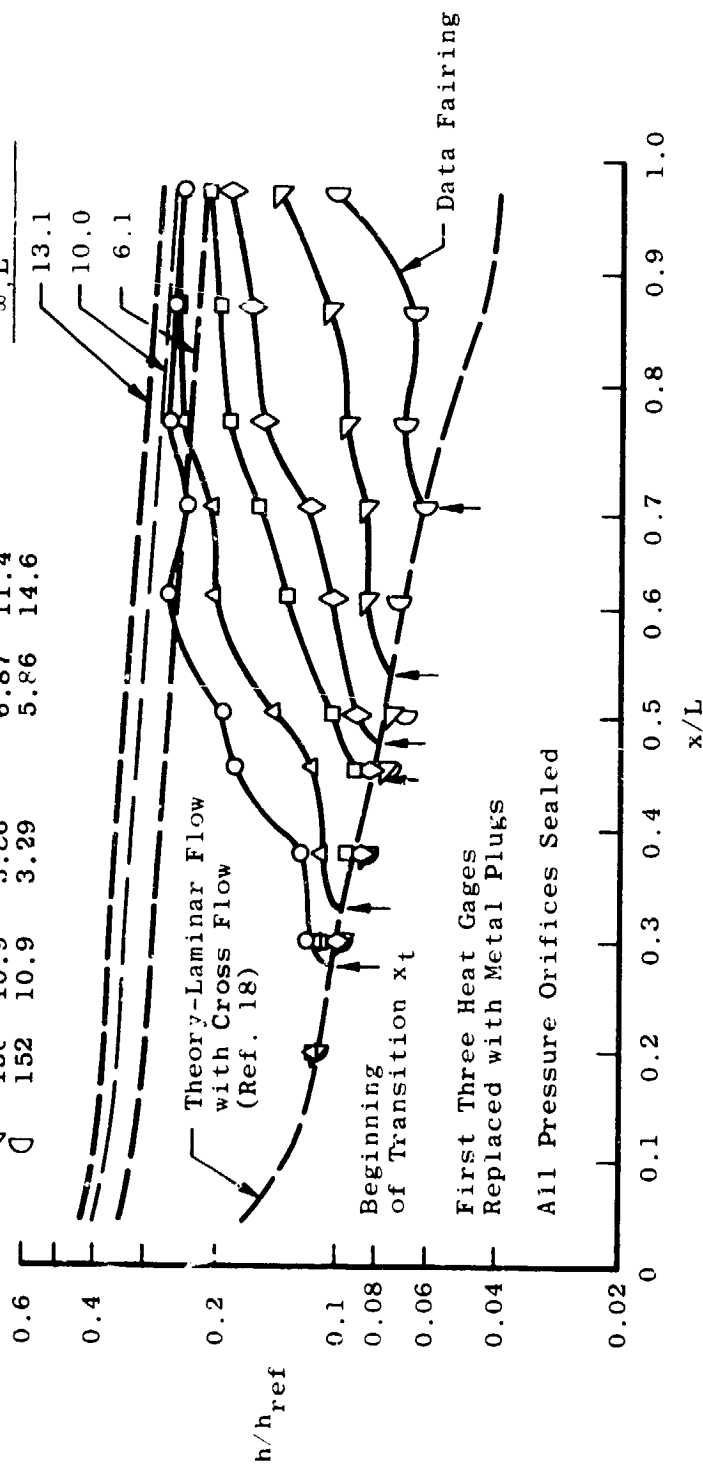


Fig. 37 Laminar, Natural Transitional, and Turbulent Heat Transfer: Results from Tunnel F.
Phase II, $M_\infty = 10.8$, $\alpha = 40$ deg

Sym	Date	Run No.	α , deg	Surface Instrumentation Location (x)	
				First Q Gage	Pressure Orifice
○	Jan 72	3825	40	0.85 in.	None
△	Jan 72	3826	40	0.85 in.	None
□	Jan 72	3828	40	4.15 in.	None
◇	Jan 72	3829*	40	4.15 in.	None
●	May 71	3662	45	0.85 in.	0, 3.05, 10.0, 14.05, 19.55 in.
●	May 71	3660	45	0.85 in.	0, 3.05, 10.0, 14.05, 19.55 in.
●	May 71	3663	45	0.85 in.	0, 3.05, 10.0, 14.05, 19.55 in.

*Burr was found in model ϕ surface at $x = 0.85$ in. after run.

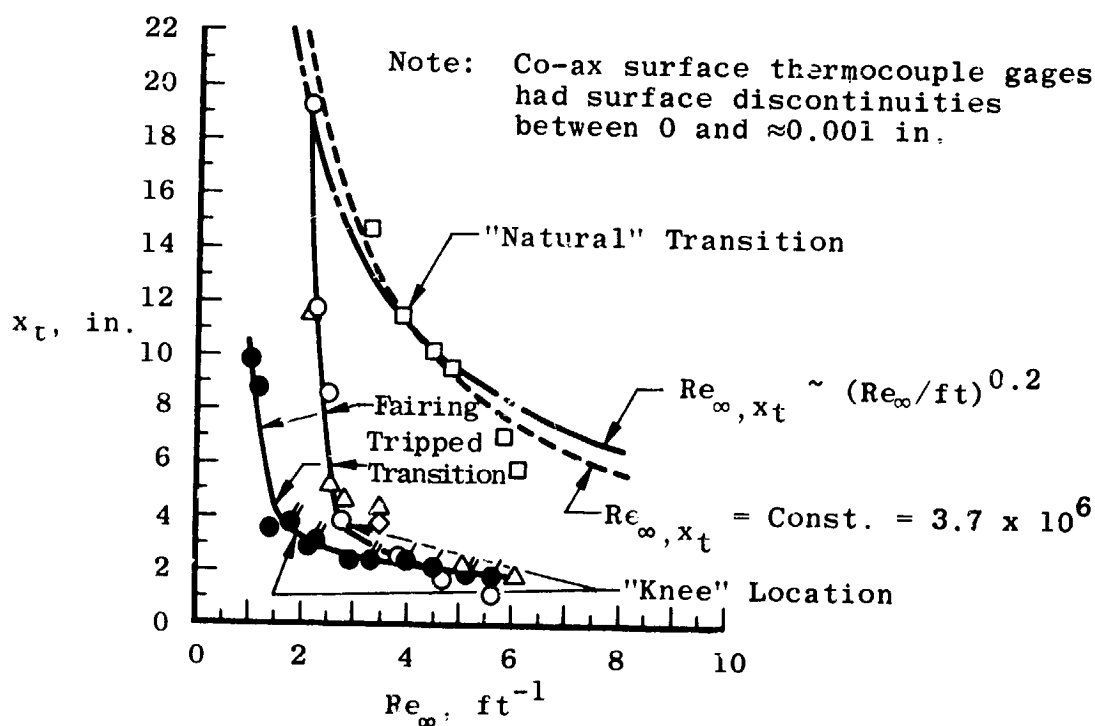


Fig. 38 Effect of Unintentional Surface Roughness on Transition Results from Tunnel F at $M_{\infty} = 10.8$, $\alpha = 40$ deg

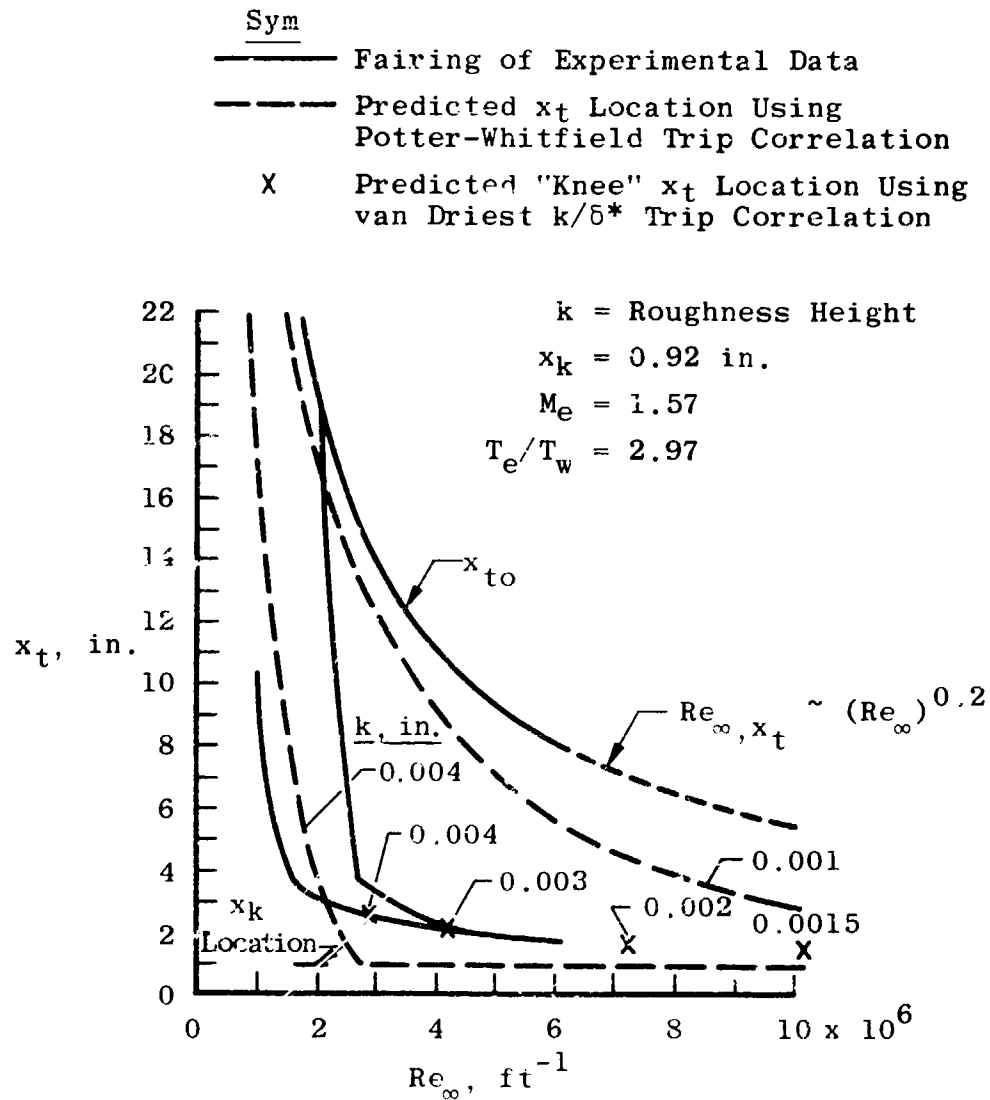


Fig. 39 Predicted Effect of Surface Roughness on Transition Results from Tunnel F at $M_{\infty} = 10.8$, $\alpha = 40$ deg

Sym	Tunnel	M_∞	α , deg	Run
O	F	10.8	40	3825
	F	10.8	40	3828
△	F	10.5	20	3650
	F	10.5	20-60	----
X	B	8.0	20-60	----
				(Tempilaq)

"Natural" Transition, Phase II
 "Natural" Transition, Phase I
 Affected by Surface Roughness, Phase I

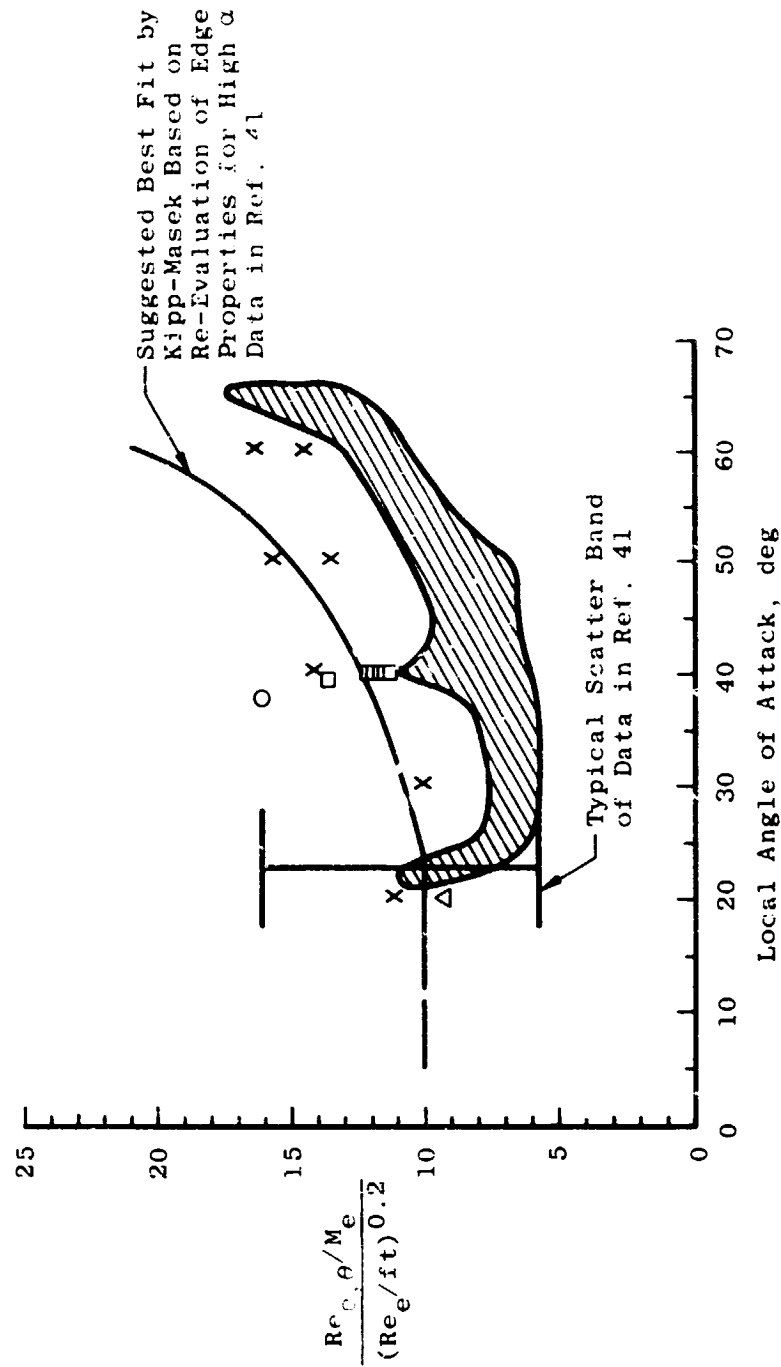


Fig. 40 Comparison of Transition Results with the Kipp-Masek Correlation

TABLE I
SUMMARY OF MODELS

Configuration No.	Model	Scale	Ref. Length, in.	Type Model:	Instrumentation and Test Technique	Builder	Tunnel
1	Orbiter	0.011	21.35	Steel: Gages and Phosphor Paint		AFDC	F
21 and 22	Orbiter	0.011	21.35	Stycast: Phase-change Paint and Pressure		Grumman	B
31 and 32	Booster	0.011	29.06	Stycast: Phase-change Paint			B
41 and 42	Booster	0.009	23.78	Stycast: Phase-change Paint and Pressure			(Mated) B (Reentry)

TABLE II
NOMINAL TEST CONDITIONS

Test Phase Tunnel	Model Scale	Ref. Length, in.	M _∞	P ₀ , psia	T ₀ , °R	Re ₀ , ft ⁻¹ x 10 ⁻⁶	Re ₀ , ft ⁻¹ x 10 ⁻⁶	α, deg	Type Data
Ascent VKF(B)	0.011	29.06	8.0	150	1180	0.8	2.0	-5, 0, 5	P
				555	1310	2.5	6.0	-5, 0, 5	P, S, O
				860	1340	3.7	9.0	0	P
Booster Reentry VKF(B)	0.009	23.78	9.0	555	1310	2.5	5.0	40, 50, 60	P
				860	1345	3.7	7.3	40, 50, 60	P, S, O, PF, SP
				860	1345	3.7 (trips)	7.3	40, 50, 60	P
Orbiter Reentry VKF(B)	0.011	21.35	8.0	555	1310	2.5	4.5	10, 20, 40, 50, 60	P
				860	1345	3.7	6.6	10, 20, 30, 40, 50, 60	P, S, PF, SP
				860	1345	3.7 (trips)	7.3	10, 20, 30, 40, 50, 60	P
Orbiter I Reentry VKF(F) II	0.011	21.35	10.2/10.9	3620/11,600	1770/2960	2.6/14.0	4.6/24.1	10, 20, 30, 40, 50, 60	Ph, G, SP, S
			11.2/11.9	2800/9300	2,000/3540	0.8/6.2	1.5/11.0	25, 45	Ph, G, SP, S
			10.7/11.0	2400/5800	1780/2350	2.1/6.2	3.8/11.0	40	G, S

Data Type Legend

P ~ Phase-Change Paint Data

S ~ Shadowgraph or Schlieren Photographs

O ~ Oil-Flow Photographs

FF ~ Rake Flow-Field Data

SP ~ Model Surface Pressure

Ph ~ Phosphor Paint Data

G ~ Heat-Gage Data

TABLE III
TUNNEL CONDITIONS CORRESPONDING TO TUNNEL F PLOTTED RESULTS

Run No.	Results	Figure	Figure Symbol	α , deg	M_∞	$Re_\infty L$	p_∞ , psia	ρ_∞ , lbm/ft ³	u_∞ , ft/sec	H_o , Btu/lbm	T_o , °R	P_o , psia	P_{o1} , psia	q_{ref} , Btu/ft ² -sec	h_{ref} , Btu/ft ² -sec-°R
	Pressure (Nominal)	16	□ □ □ □	10, 20, 30, 40, 50, 60	10.6	10×10^6	0.132	2.98×10^{-3}	5680	674	2460	7620	19.1	230	0.120
3654	Heat-Transfer (Phase I)	17	□ □ □ □	10	10.5	8.6×10^6	0.117	2.57×10^{-3}	5710	681	2500	6570	16.7	217	0.111
3654					10.9	21.9×10^6	0.195	5.58×10^{-3}	5170	557	1980	11600	29.7	216	0.150
3650					10.3	6.1×10^6	0.0798	1.83×10^{-3}	5470	625	2330	3920	10.8	153	0.0855
3651					20	9.9×10^6	0.0967	2.64×10^{-3}	5170	557	2060	5490	14.0	149	0.0979
3651					20	20.1×10^6	0.183	5.14×10^{-3}	5250	573	2050	11330	28.1	219	0.145
3659		18	□ □ □ □	50	10.5	7.4×10^6	0.0977	2.19×10^{-3}	5660	669	2470	5620	14.0	194	0.101
3664					10.5	7.2×10^6	0.0965	2.15×10^{-3}	5670	670	2470	5440	13.7	194	0.101
3659					10.7	22.5×10^6	0.213	5.91×10^{-3}	5170	557	1990	11410	31.4	222	0.154
3658					60	5.9×10^6	0.113	2.01×10^{-3}	6250	817	2960	6210	15.4	266	0.110
3658					60	12.9×10^6	0.167	3.81×10^{-3}	5610	658	2390	8850	23.9	248	0.134
3658	Heat-Transfer (Phase II)	19	□ □ □ □	40	10.7	24.1×10^6	0.209	2.01×10^{-3}	5010	522	1860	10830	30.7	196	0.149
3825					10.7	9.97×10^6	0.0856	2.54×10^{-3}	5000	520	1920	5040	12.6	125	0.0905
					10.7	6.84×10^6	0.0613	1.76×10^{-3}	5110	543	2020	3920	9.1	115	0.0779
					10.9	4.41×10^6	0.0351	1.08×10^{-3}	5030	525	1960	2620	5.4	83	0.0583
					10.9	3.98×10^6	0.0327	0.99×10^{-3}	5060	533	2000	2430	5.0	82	0.0563
		20	□ □ □ □		10.9	3.79×10^6	0.0321	0.95×10^{-3}	5110	542	2030	2380	4.9	85	0.0566
3828					10.8	10.97×10^6	0.0832	2.66×10^{-3}	4940	488	1780	5050	12.4	112	0.0901
					10.8	10.35×10^6	0.0778	2.50×10^{-3}	4940	487	1780	4810	11.6	101	0.0870
					10.8	8.57×10^6	0.0673	2.10×10^{-3}	4930	507	1870	4370	10.1	109	0.0820
					10.8	7.96×10^6	0.0606	1.93×10^{-3}	4900	500	1840	4030	9.2	101	0.0778
					10.9	6.87×10^6	0.0504	1.64×10^{-3}	4870	494	1820	3530	7.7	91	0.0712
					10.9	5.86×10^6	0.0428	1.40×10^{-3}	4850	489	1810	2990	6.5	85	0.0652

TABLE IV
TUNNEL F TEST SUMMARY

a. Phase I

α , deg	Run	$\sim M_\infty$	$\sim Re_\infty, L$
10.0	3654	10.0	$8-22 \times 10^6$
10.0	3656	10.2	8×10^6
20.0	3650	10.4	$6-10 \times 10^6$
20.0	3651	10.7	$10-20 \times 10^6$
20.0	3652*	10.3	9×10^6
25.0	3667	11.2	$2-6 \times 10^6$
30.0	3653	10.4	$7-20 \times 10^6$
30.2	3655	10.5	$5-17 \times 10^6$
40.5	3657	10.4	$9-11 \times 10^6$
40.2	3661	10.5	$6-13 \times 10^6$
45.0	3660	11.9	$7-10 \times 10^6$
45.2	3662	11.4	$2-5 \times 10^6$
45.0	3663	11.8	$3-9 \times 10^6$
51.0	3659	10.7	$7-22 \times 10^6$
50.2	3664	10.5	$5-9 \times 10^6$
60.5	3658*	10.6	$6-24 \times 10^6$
60.2	3665	10.4	$5-11 \times 10^6$

*Three Point Pitot Survey

b. Phase II

α , deg	Run	$\sim M_\infty$	$\sim Re_\infty, L$
40	3825	10.9	$4-10 \times 10^6$
↓	3826	↓	$4-11 \times 10^6$
	3828		$6-11 \times 10^6$ (Natural Transition)
	3829		$6-11 \times 10^6$

APPENDIX III EVALUATION OF STYCAST THERMAL PROPERTIES

INTRODUCTION

An extensive Space Shuttle heating test program sponsored by NASA-MSFC has recently been completed at AEDC-VKF. A large portion of this program was devoted to testing phase-change paint models fabricated from Stycast 2762. Stycast has been used for this purpose for several years because of its low diffusivity, ability to withstand the high temperatures experienced in hypersonic wind tunnels, and its molding characteristics.

The reduction of phase-change paint data to quantitative results requires knowledge of the model material thermal properties. Normally, models are fabricated from materials having low diffusivity, and semi-infinite solid assumptions are used to infer heating rates from the observed surface temperature response. Specifically, the product (ρck), where ρ is density, c is specific heat, and k is the thermal conductivity, is needed. There are two basic methods of obtaining the ρck values. First, an analysis of the material can provide values for the individual properties. Second, a technique which utilizes a known heat input to the material can be used to infer the material properties from the surface temperature response. This method normally takes the form of a wind tunnel test of a sphere model of the subject material. For this test program, both techniques were employed to provide a check of the procedures and to optimize data precision.

ANALYSIS

Phase-change paint data reduction, including the sphere calibration technique, utilizes the equation governing the surface temperature response of a semi-infinite solid which experiences a step heating input:

$$\frac{T_w - T_{wi}}{T_{aw} - T_{wi}} = 1 - e^{\beta^2} \operatorname{erfc} \beta$$

where

$$\beta = \frac{h \sqrt{\Delta t}}{\sqrt{\rho ck}}$$

For normal data reduction, this equation is solved for h , the heat-transfer coefficient. The sphere calibration technique uses a theoretical value for h , and the model thermal properties ($\sqrt{\rho ck}$) are determined.

For the Space Shuttle test program, a 6-in. diam hemisphere model was cast and cured with each Stycast model to permit evaluation of batch-to-batch uniformity. Because of apparent inconsistencies in the hemisphere data, a number of repeat runs were made on one hemisphere model, and these results follow.

Prior to testing, the model was striped with a thin coat of high-temperature paint to permit visual identification of the phase-change locations. The stripes were applied circumferentially at 10-deg intervals from the stagnation point ($\theta = 0$) to the shoulder ($\theta = 90$ deg). During a typical test run, the model was exposed to the tunnel flow about 20 sec. Several longer runs were made when the test conditions (i. e., the model wall temperature) permitted. The progression of the phase-change paint melt line over the model surface was recorded on 70-mm black and white film at 0.5-sec intervals.

The results of five runs shown in Fig. III-1 are plotted versus the model location at which the data were obtained. Two paint temperatures were used on runs 296 and 297 (the model was masked along the vertical centerline and the paints were sprayed on either side) to increase the amount of data from each run. The data scatter (± 20 percent) was in excess of that expected, and a reason for the scatter was sought. The data were obtained at two Reynolds numbers and with four different paint temperatures. Since some variation of the material properties with temperature was expected, the data from Fig. III-1 were replotted versus paint (or wall) temperature, as shown in Fig. III-2. The results of an analysis of the model material (individual ρ , c , k measurements) are also shown and indicate a slight trend with temperature for the lower wall temperatures. The hemisphere data, however, show no discernible trend with temperature. Note that the symbols defined in Fig. III-1 are used in all figures to permit identification of the individual data points.

As shown in Fig. III-1, a trend with θ is observed; that is, as θ increased, $\sqrt{\rho ck}$ generally decreased. It was speculated that, since the model was cast with the nose ($\theta = 0$) down, heavier parts of the material may have settled toward the nose during curing, thus altering the material thermal properties. To experimentally evaluate this possibility, a run was made with the hemisphere at 30-deg angle of attack. The

results of this run are compared with run 296 in Fig. III-3. To facilitate data comparison, θ was measured from the stagnation point in each case so that, if the material properties varied around the model, a shift of 30 deg in the data should be evident. In fact, no shift occurred, and it was concluded that material uniformity in the θ direction was not a problem. Note that these additional data increased the total data spread to ± 34 percent.

Since the only discernible trends appeared to be related to θ , the theoretical predictions used for h versus θ were reviewed and compared with data from thermocouple and heat-rate gage models. This comparison confirmed the technique being used and thus shed no light on the problem.

Attention was turned to the heating time since this is one of the basic experimental variables. Injection of the model through the tunnel boundary layer could introduce up to 0.5-sec uncertainty in the heating time. However, an error of about three seconds would be required to produce the $\sqrt{\rho ck}$ variation shown in Fig. III-3. The data were plotted versus \sqrt{t} as shown in Fig. III-4, and some improvement in data scatter was observed, although the $\sqrt{\rho ck}$ variation still existed. A straight-line fairing of the data is shown and correlates the $\sqrt{\rho ck}$ variations within about ± 10 percent. A variation of $\sqrt{\rho ck}$ with time could be caused by variation of thermal properties with material depth since the diffusion of heat in a solid is basically a function of time. To check this possibility, two investigations were made. First, the model was sliced normal to the surface, and the sliced surface was polished to expose the structure of the material. A 40-X photographic enlargement of this surface is shown in Fig. III-5. The photograph clearly shows a concentration of lighter colored particles (< 0.050 in.) near the model surface. Since Stycast is a mixture of epoxy (black) and alumina (Al_2O_3), the light particles are assumed to be alumina. The epoxy has thermal properties quite different from alumina. Typical values for $\sqrt{\rho ck}$ are 0.04 for epoxy and 0.35 for alumina. Obviously the thermal properties of the mixture (Stycast) are sensitive to the distribution of the alumina particles.

To check the effect of the apparent alumina concentration near the surface, the second investigation was made. Two samples of the model material were checked for thermal properties in the VKF Instrument

Laboratory. Thin-film resistance elements were deposited on the surface of the samples. Temperature-resistance calibrations of the elements were made, and the surface were then subjected to a very short (0.1-sec) calibrated convective heat pulse. This procedure is commonly used to calibrate heat-rate gages for short-duration test applications and permitted a $\sqrt{\rho ck}$ evaluation similar to the sphere calibration technique. The $\sqrt{\rho ck}$ values thus obtained are plotted in Fig. III-4 and identified as VKF laboratory data. Each point represents the average of three runs, and about ± 10 percent scatter existed in these data. These results present a strong confirmation of the time correlation since the fairing of the hemisphere data extrapolates very near to the laboratory points.

To check the compatibility of the $\sqrt{\Delta t}$ correlation with the observed material nonuniformity, an analytical model was formulated. A distribution of material thermal properties with depth was assumed, and the surface temperatures response to a convective heat input was computed. This surface temperature response was compared with constant property solutions to infer an effective constant $\sqrt{\rho ck}$. From these solutions, the variation of the effective $\sqrt{\rho ck}$ with time was plotted and compared with the hemisphere data. These results are presented in Fig. III-6 and basically confirm the validity of the $\sqrt{\Delta t}$ correlation. The analytic models of $\sqrt{\rho ck}$ variation with depth were chosen to approximate the limits in $\sqrt{\rho ck}$ variation shown in Fig. III-4 and the alumina distribution shown in Fig. III-5.

CONCLUSIONS AND RECOMMENDATIONS

1. The scatter in the Stycast 2762 thermal property data obtained at VKF was reduced from ± 34 percent to ± 10 percent by correlation with time. The equation used in the data reduction was
$$\sqrt{\rho ck} = 0.11 - 0.008\sqrt{\Delta t}.$$
2. The validity of the time correlation is attributed to variation in the alumina filler distribution in the material.
3. These results should not be applied directly to other test data since the cause of the nonuniform filler distribution is unknown.

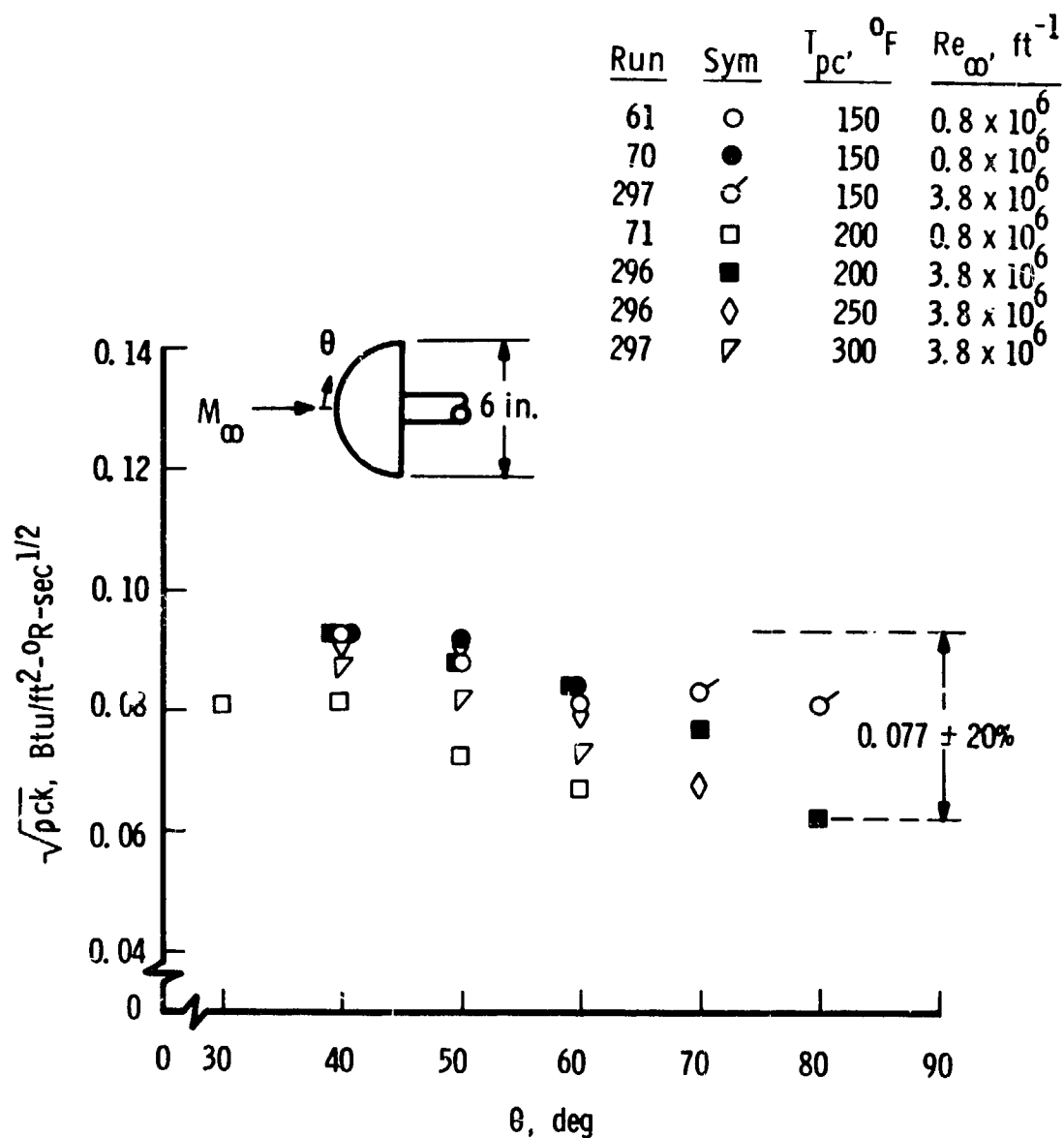


Fig. III-1 Model Material Thermal Property Variation with Model Location

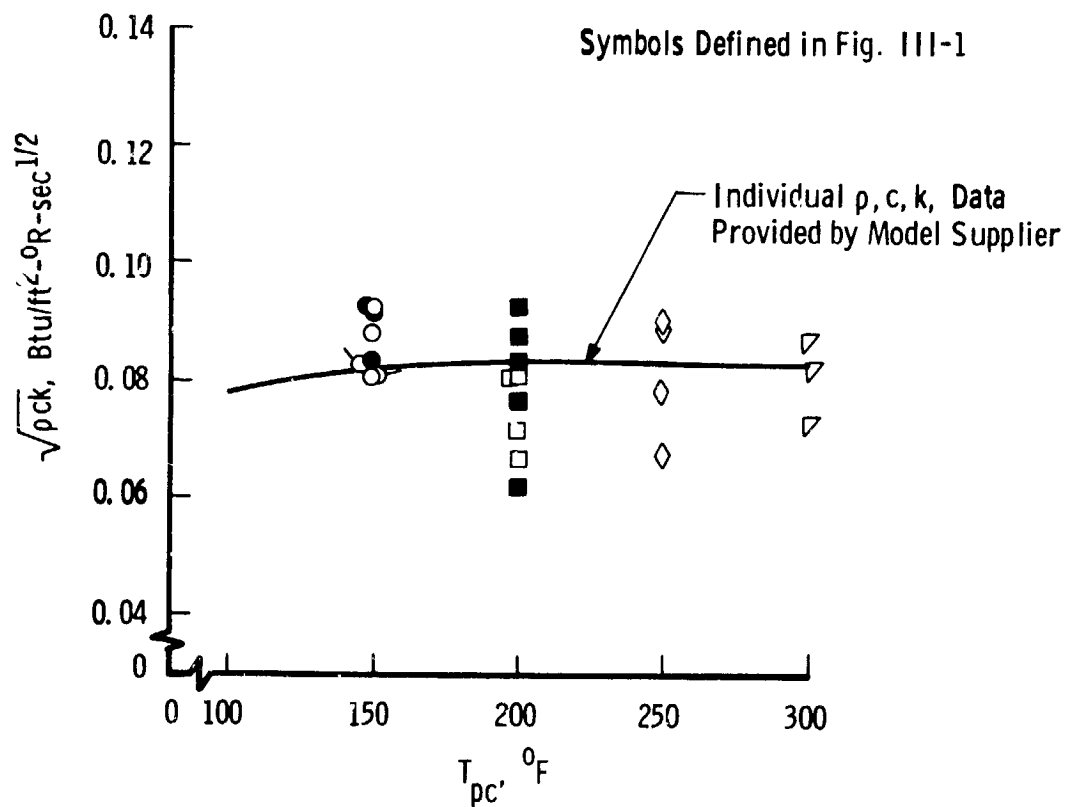


Fig. III-2 Thermal Property Variation with Wall Temperature

Run	Sym	T_{pc} , °F	α , deg
296	◇	250	0
298	◆	250	30

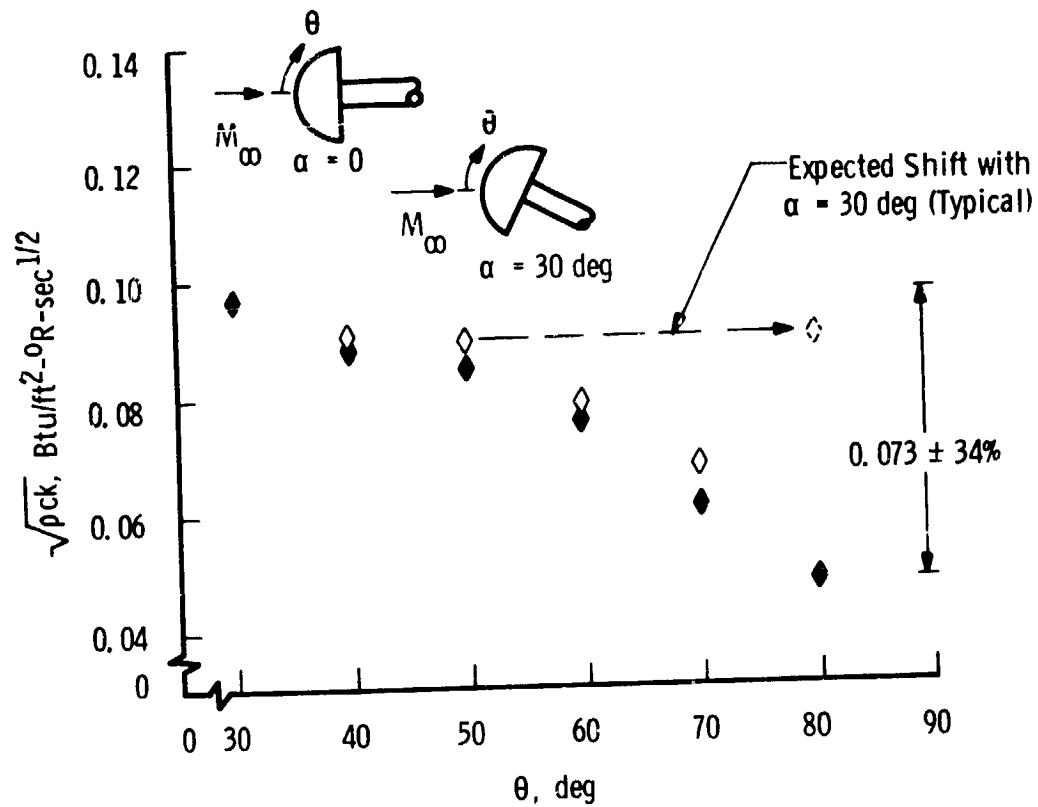


Fig. III-3 Thermal Property Variation with Location for 0- and 30-deg Angle of Attack

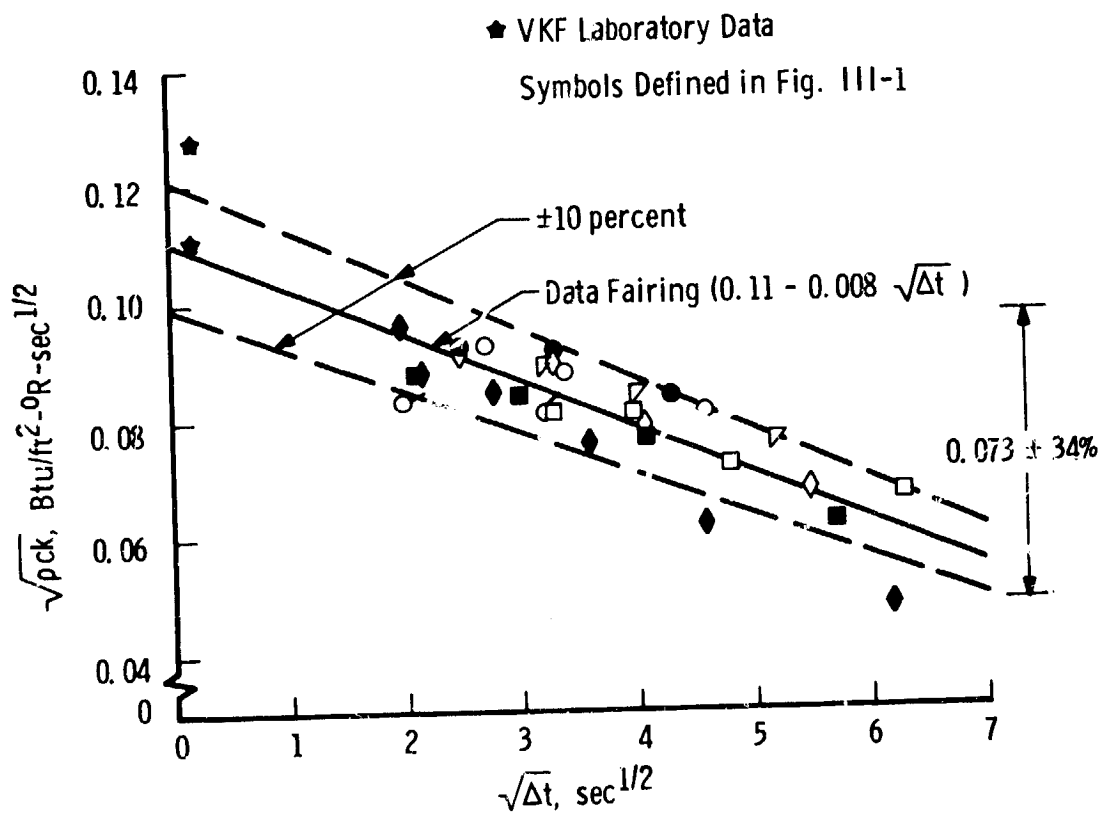
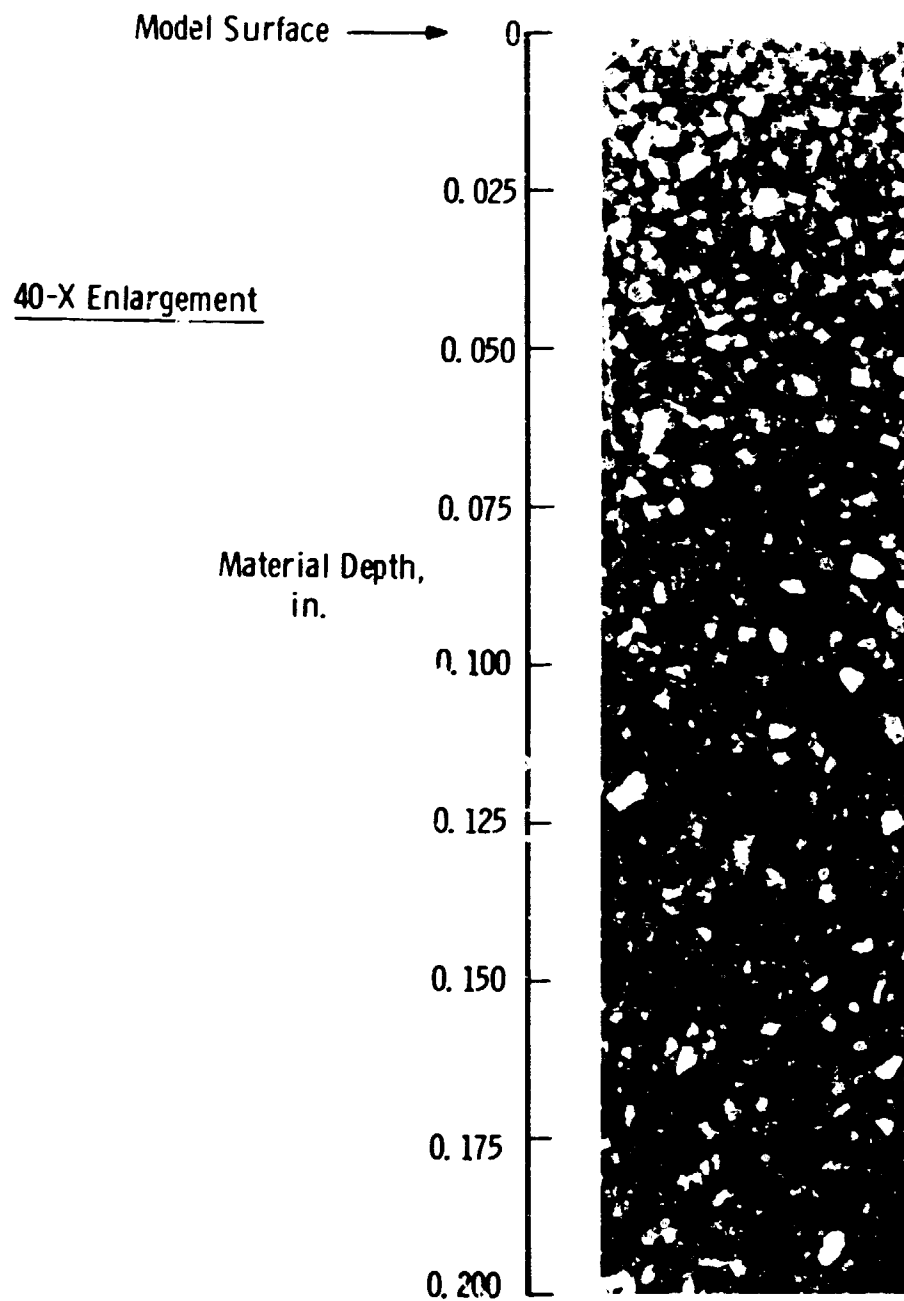


Fig. III-4 Correlation of Thermal Properties with Time



**Fig. III-5 Photographic Enlargement of Stycast Structure
near the Model Surface**

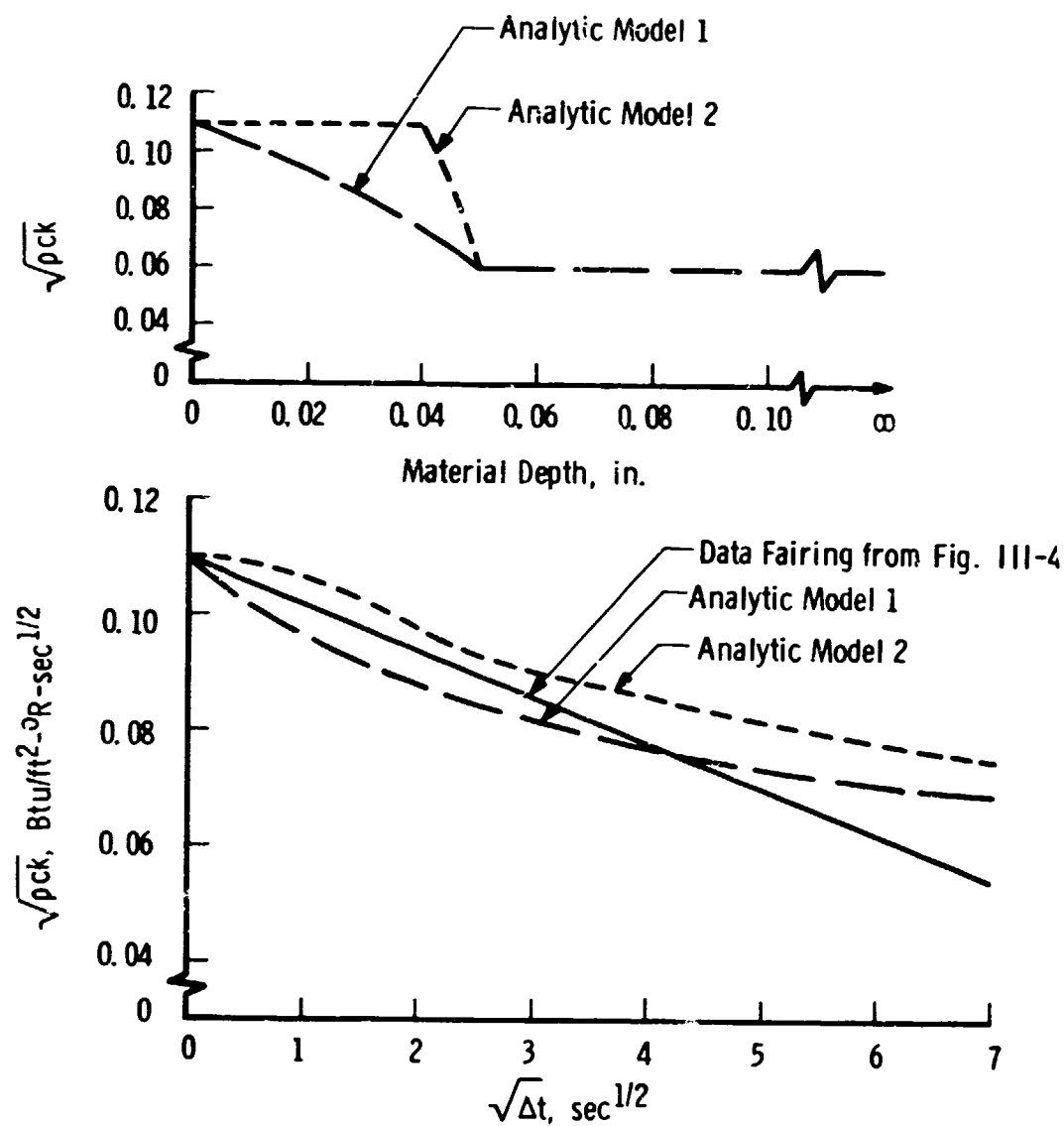


Fig. III-6 Comparison of Analytic Results with Hemisphere Calibration Data

APPENDIX IV

VKF BOUNDARY LAYER TRIP PROCEDURES USED DURING THE NASA-AEDC STS HEATING TEST IN TUNNEL B

The use of the phase-change paint heat-transfer technique can provide a complete mapping of the heat transfer distribution on a given model surface. This is not practical with the thin skin or heat gage techniques. However, this new wealth of data has brought to light new problems. Tests of delta wing type models at relatively high angles of attack (30 to 60 deg) at the VKF and other test facilities have shown that small surface irregularities are sufficient to produce boundary layer transition. In fact, it has been observed that small (<0.010 in.) particles in the paint can promote transition. Since the heating rates downstream of the particles are significantly higher (i. e., turbulent levels) than those upstream of the particles, a characteristic spiked melt pattern originates from the particle or surface irregularity.

To obtain turbulent heating levels over a major portion of the model, advantage was taken of the above phenomenon. That is, closely spaced surface irregularities were placed on the entire windward surface (bottom) of the delta wing orbiter and booster. The application method consisted of dabbing small dots of Barco Bond⁴ in about 1-in. intervals on the bottom surface of the models and then sprinkling the surface with No. 46 grit (~ 0.015 -in. diameter). Several pieces of grit adhered to each dot, resulting in a small surface irregularity approximately 0.025 in. high. With the exception of the nose region, these surface irregularities were sufficiently large enough to trip the laminar boundary layer producing the desired turbulent heating levels.

For angles of attack of 10 and 20 deg, the grit did not trip the boundary layer. For these angles, 0.030-in. -diam steel spheres were welded about one diameter apart on the steel nose cap of the MDAC-DWO (Configuration 22).

⁴Epoxy adhesive (Kit No. MB-165).

APPENDIX V

PHASE-CHANGE PAINT DATA REDUCTION ASSUMPTIONS

A complete description of the phase-change paint technique, including the assumptions made, was presented in Ref. 42. A summary of the assumptions listed in Ref. 42, and others applicable to the present tests, is given below.

1. The depth of heat penetration into the wall is less than the wall thickness and very small compared with the surface radius of curvature so that the wall acts like a one-dimensional semi-infinite slab. The present models were solid Stycast, and therefore, this assumption should be valid with the exception of small radius edges.
2. The model is isothermal before injection into the air-stream. Thermocouples embedded within the model were monitored to ensure that the model was isothermal before injection.
3. The surface experiences an instantaneous step in local aerodynamic heat-transfer coefficient at time zero, and this coefficient is invariant with time. The models were exposed to the tunnel airflow approximately 0.7 sec before reaching the tunnel centerline and this time is considered in determining time zero. By not considering photographs obtained during the first 3 sec of model exposure, uncertainties in heat-transfer coefficient attributable to errors in time are minimized.
4. The thermal diffusivity and conductivity of the wall is invariant with temperature. An evaluation of the Stycast thermal properties was presented in Appendix III.
5. The phase-change coating melts when the wall temperature reaches the specified value (i. e., $T_{pc} = T_w$). Uncertainties in the specified phase-change temperature are estimated by the manufacturer to be ± 1 percent.
6. The radiation heating produced by the fluorescent lighting and model radiation to the tunnel walls are negligible compared with the aerodynamic heating.

7. The metallic noses did not distort either the temperature distribution in the model material or the development of the boundary layer.
8. As discussed by Throckmorton (Ref. 43) the largest uncertainty in the reduction of phase-change paint data is probably caused by observer interpretation. The reduction of phase-change paint data requires the visual identification of the melt line, and its identification may vary from one observer to another.

APPENDIX VI FLOW FIELD REGIMES ON THE WINDWARD SURFACE OF THE MCDONNELL DOUGLAS ORBITER

The planform of the McDonnell Douglas orbiter can be fairly well represented by a 81.5-deg sweep delta wing for values of x/L between 0.1 and 0.6. Even though the bottom surface is curved, the flow field should be basically similar to that of a flat-bottomed sharp-edged wing of approximately the same sweep angle.

The $\rho_r \mu_r$ heat transfer method presented in Ref. 44 relates the variation in inviscid flow field properties to delta wing centerline heating through the use of the variable (n) which is the centerline flow divergence angle derivative, $(\frac{d\omega}{d\phi})_{\phi=0}$. By assuming that the influence of the spanwise pressure gradient is negligible and combining equations A10A, A10C, and A18 of Ref. 44, the following expression is obtained:

$$\frac{h}{h_{2D}} = \sqrt{1 + 2n} \quad (\text{VI-1})$$

Note that for $n = 1.0$, the result is the same as that obtained for the sharp cone to flat plate heating ratio, i. e.

$$\frac{h}{h_{2D}} = \sqrt{3}$$

An estimate of $(\frac{d\omega}{d\phi})_{\phi=0}$ for sharp-edged delta wings of various sweep angles at Mach number 9.6 is shown in Fig. 74 of Ref. 45 and is reproduced here as Fig. VI-1. It can be seen from this figure that for an 80-deg sweep wing, $(\frac{d\omega}{d\phi})_{\phi=0}$ is between 0.7 and 1.0 for angles of attack between 10 and 30 deg. Substitution of $n = 0.7$ into Eq. (VI-1) results in heating ratios only slightly below the conical value. The conclusion then is that the heating rates on an 80-deg sweep delta wing at angles of attack between 10 and 30 deg are approximately the same as those on an equivalent axisymmetric body; i. e., a body whose local radius is equal to the local semispan of the delta wing which in this case is a cone.

This result was applied to the McDonnell Douglas orbiter by using solutions to the axisymmetric boundary layer equations presented in

Appendix VII. The radius used in this solution for values of x/L less than 0.6 was the local semispan of the body in analogy with the sharp-edged delta wing result.

At values of x/L greater than 0.6, the McDonnell Douglas orbiter has an effective sweep angle of about 55 deg. Values of $(\frac{dw}{d\phi})_{\phi=0}$ for a 60 deg sweep wing are shown in Fig. VI-1. From these results for $\alpha = 20$ deg, it would appear that $(\frac{dw}{d\phi})_{\phi=0}$ would be 0.4 or less and hence the heating rate ratio would be closer to the two-dimensional value. In order to obtain the two-dimensional result from the axisymmetric equations, the radius is held constant.

The radius distribution resulting from these considerations and which was used in the 10- and 20-deg angle of attack heating calculations is shown graphically in Fig. 35a.

By returning once again to the 80-deg sweep results in Fig. VI-1, it may be seen that the value of $(\frac{dw}{d\phi})_{\phi=0}$ is greater than 1.0 for angles of attack greater than 33 deg. A streamline path illustrating this condition is shown on the sketch in Fig. VI-1. This flow pattern is similar to that produced on an infinite swept cylinder which implies that spanwise strip theory (crossflow theory) may be valid. This is shown to be the case in Ref. 18 where a complete discussion of this approach is given.

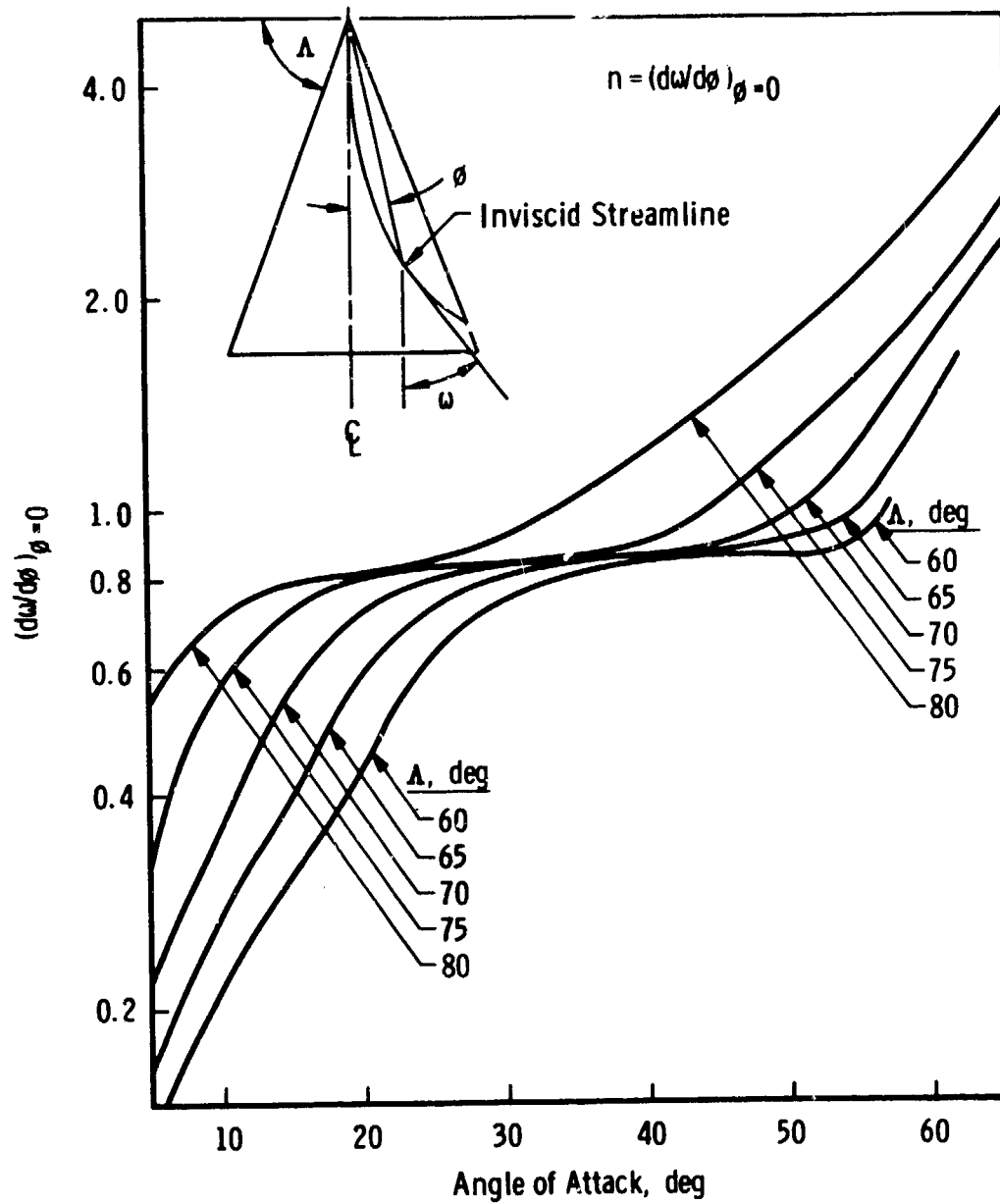


Fig. VI-1 Rate of Change of Inviscid Streamline Angle Along the Centerline of a Sharp Delta Wing, $M_\infty = 9.6$

APPENDIX VII
LOCALLY SIMILAR BOUNDARY LAYER CALCULATIONS USING
THE TABULATED SOLUTIONS OF DEWEY AND GROSS

It was shown in Appendix VI that the flow near the orbiter surface was axial at 10- and 20-deg angle of attack. To make reliable heating rate and boundary-layer thickness parameter calculations, a suitable method of solution of the two-dimensional and axisymmetric boundary layer equations is necessary. It was shown in Ref. 46 that the locally similar solutions of the boundary layer equations give accurate heating rate and boundary-layer thickness parameter predictions when pressure gradients are mild. This condition was met by the flows currently under consideration.

Dewey and Gross (Ref. 47) solved the boundary-layer equations for a wide range of conditions and tabulated values of ϕ'_w , I_1 , and I_2 .⁵ In the present application, the parameters St_∞ , θ , and δ^* were computed from the following equations:

$$St_\infty = \frac{\rho_w \mu_w u_e H_o (1 - \frac{T_w}{T_o}) r^j \phi'_w}{\rho_\infty u_\infty (H_o - H_w) Pr \sqrt{2\xi}}$$

$$\theta = \frac{\sqrt{2\xi}}{\rho_e u_e r^j} I_2$$

$$\delta^* = \frac{\sqrt{2\xi}}{\rho_e u_e r^j} \left(\frac{T_o}{T_e} \right) \left(I_1 - \frac{T_e}{T_o} I_2 \right)$$

Note: for a perfect gas,

$$\frac{h}{h_{ref}} = \frac{St_\infty}{St_{\infty, ref}}$$

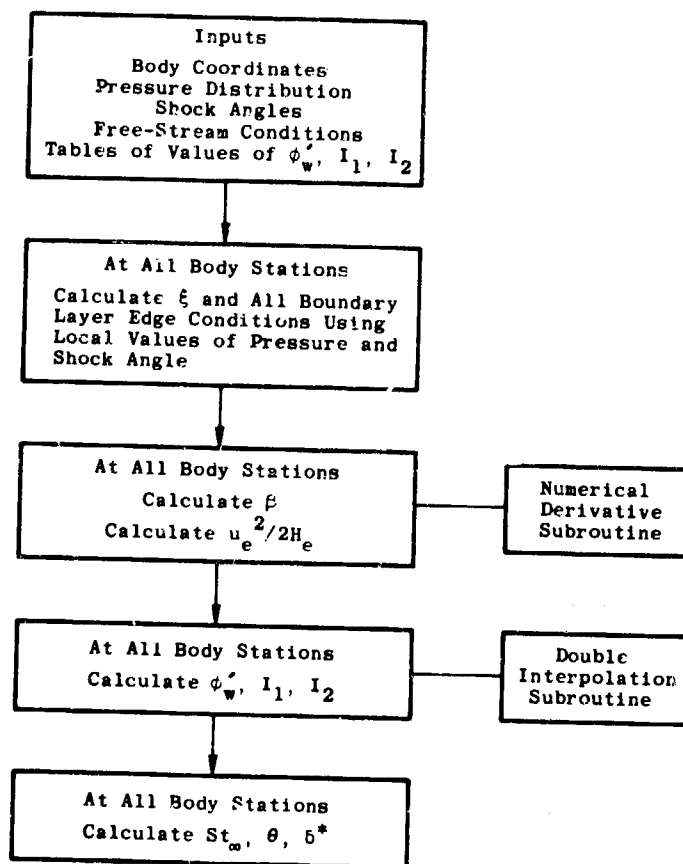
The values of the boundary-layer parameters were tabulated in Ref. 47 for a range of values of β , $u_e^2/2H_e$, Prandtl number, wall temperature ratio, and temperature-viscosity law. A Prandtl number of 0.7 was selected for the present calculations. A temperature-viscosity

⁵See Fig. VII-1 for nomenclature peculiar to this appendix.

law of $\mu \propto T^{0.7}$ was selected because Dewey and Crane showed it gave good agreement with the Sutherland law for the temperature range of the present calculations. The wall temperature ratio was fixed by the particular case.

Values of ϕ_w , I_1 , and I_2 were then obtained from the tabulated solutions for several values of $\bar{\beta}$ and $u_e^2/2H_e$. These values were then input into a computer solution. At each calculation point, a double interpolation procedure was used to obtain the value of the boundary-layer parameter for the value of $\bar{\beta}$ and $u_e^2/2H_e$ at the point.

A flow diagram of the calculation procedure is given in Fig. VII-1.



f' u/u_e

I_1 Integral parameter used in the calculation of displacement thickness, $(T_w/T_o - 1) \int_0^\infty (1-\phi) d\eta + \int_0^\infty (1 - f'^2) d\eta$

I_2 Integral parameter used in the calculation of displacement and momentum thickness, $\int_0^\infty f'(1 - f') d\eta$

i 0 for two-dimensional flow, 1 for axisymmetric flow

β Velocity gradient parameter, $(2\xi/u_e)(du_e/d\xi)$

$\bar{\beta}$ Velocity gradient parameter, $\beta(T_o/T_e)$

η Transformed y coordinate

θ Boundary-layer momentum thickness

ξ Transformed surface distance coordinate

ϕ $\frac{H-H_w}{H_e-H_w}$

Fig. VII-1 Calculation Flow Diagram and Nomenclature